

Preparation of Main-group and Transition metal Graphenic Nano-composites for Energy Application

*A thesis
submitted in partial fulfilment
of the requirements for the*

Doctor of Philosophy

By

Akula Naveenkumar

(20153363)



**Department of Chemistry,
Indian Institute of Science Education and Research (IISER),
Pune, India - 411008**

January 2021

Dedicated to

My mother

Sri. Saraswathi

(without you it would not have been possible)

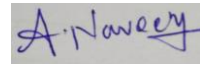
DECLARATION

I declare that this written submission represents my ideas in my own words and wherever other's ideas have been included, I have adequately cited and referenced the original sources. I also declare that I have adhered to all principles of academic honesty and integrity and have not misrepresented or fabricated or falsified any idea / data / fact / source in my submission. I understand that violation of the above will cause for disciplinary action by the Institute and can also evoke penal action from the sources which have thus not been properly cited or from whom proper permission has not been taken when needed.

Date: 24th February 2021

Mr. Akula Naveenkumar

(Reg. No: 20153363)



CERTIFICATE

This is to certify that this dissertation entitled “**Preparation of Main-group and Transition metal Graphenic Nano-composites for Energy Application**” towards the partial fulfilment of the PhD degree programme at the Indian Institute of Science Education and Research, Pune represents original research carried out by Akula Naveenkumar at IISER Pune under my supervision. The work presented here or any part of it has not been included in any other thesis submitted previously for the award of any degree or diploma from any other university or institution.

Date: 24th February 2021



Dr. Moumita Majumdar

(Thesis Supervisor)

Acknowledgments

On successful completion of this thesis, it is my pleasure to acknowledge all those who have contributed towards it, be it through encouragement, guidance and/or support.

I would first like to express my sincere gratitude towards my research supervisor Dr. Moumita Majumdar for her excellent guidance throughout the course of my doctoral studies. Her understanding of behavior, emphasis on the rigorousness of concepts and constant encouragement at every step of the research has allowed me to mold into an independent researcher. I also thank her for permitting me to work on this research problem and encouraging me to cultivate my own understanding of the literature.

I want to thank my RAC Members, Dr. Nirmalaya Ballav and Prof. Satish Ogale for their valuable comments during our annual RAC meetings. Their criticality and attention to detail encouraged me to investigate my claims and understanding of concepts more thoroughly before presenting, whether in written or oral form.

I want to thank all my lab mates in Dr. Moumita's group for reviewing my work critically, suggesting to me with experiments and comforting me during several roadblocks during this long tenure of 5.5 years.

I can't imagine my Ph.D. with the constant love and support of my family and friends. They have played a very significant role in ensuring that I am always in the best mental health to conduct my research and cope with the failures therein.

I would like to also thank CSIR-NCL-Pune and the Savitribai Phule Pune University where a few of the experiments were carried out and all the agencies that have funded me during the tenure of my doctoral studies particularly, IISER for Research fellowship.

Synopsis

Materials in nano-dimensions show intriguing properties that have led to a wide range of applications from medicine to device fabrications. In my thesis work, I have focussed in developing synthetic methodology for main-group nano-materials under relatively benign reaction conditions. The synthesized nano-materials have been tested for anode performance in lithium ion battery. More details of different chapters of this thesis are discussed below.

Chapter 1. Introduction: This chapter gives a brief introduction of the work carried out in this thesis. To begin with, the recent progress of N-doped carbon nanosheets synthesis is discussed briefly. Subsequently, the fundamentals of widely used protocols of colloidal synthesis and solid state reactions are described. Nano Crystals provide more surface to volume ratio yielding more active sites for catalytic reactions. But this large contribution of surface sites hinders charge transport in NC solids, which often reduces electrocatalytic processes in Li-ion batteries and HER water splitting. Therefore, approaches to improve the charge transport properties of nanocrystalline solids are discussed. In the end the basic principles of the experimental methods such as batteries and HER water splitting are discussed.

Chapter 2. Coherent Solution-phase Synthesis of a Germanium-Graphitic Nanocomposite and Its Evaluation for Lithium-Ion Battery Anodes: Non-innocent Role of the Mashima Reagent: In this chapter, Ge-graphitic nano-composites have been coherently prepared under hot-injection conditions. This is the first report of simultaneously synthesizing Ge(0) nanocrystals and graphitic carbon in the solution-phase. The concurrent growth has led to the strong anchoring of Ge nanocrystals onto the graphitic carbon sheets. Ge has a very high theoretical capacity of 1600 mAhg⁻¹ and hence is much coveted for constructing high energy density lithium ion battery. However, Ge is not commercially popular as it suffers from huge volume expansion during lithiation/delithiation process. In our nano-composite, the graphitic carbon helps to buffer the volume expansion to some extent. The detailed study of lithium ion battery anode performance of the Ge-graphitic nanocomposite has been done.

Chapter 3. Synthesis and Characterisation of N-rich Carbon Nanosheets and their Application as Anode Material in Li-ion Battery: In this chapter, Carbon nano-sheets have been prepared from organosilicon reagents using a very facile approach. The synthesized carbon nano-sheets have been characterized using powdered X-ray diffraction

techniques, Raman spectroscopy, X-ray photoelectron spectroscopy, FT-IR and elemental analysis. The microstructures have been studied using FE-SEM, HRTEM and AFM techniques. These graphenic carbons with very high nitrogen content show very good lithium ion battery anode performance.

Chapter 4. Simultaneous Synthesis and Characterisation of Antimony-Graphitic Nanocomposite and its anode performance in Li ion Battery: In this chapter, Sb-graphitic nano-composite has been synthesized. The anode performance of this nano-composite has been studied for both lithium ion and sodium ion batteries. Although literature report suggests that the Sb is reputed for sodium ion battery anode application, in our case, we did not obtain reasonably good battery data. The lithium ion battery data is rather very promising.

Appendix

Cobalt-Graphitic Nano-Composite, Characterization and HER Performance

Co-graphitic nano-composite has been prepared. The utility of combining Co nano-crystals along with graphitic carbon has been studied for application in hydrogen evolution reaction.

List of Abbreviations

AFM: Atomic Force Microscopy

BET: Brunauer-Emmett-Teller

CE: Counter Electrode

CV: Cyclic Voltammetry

EDAX: Energy Dispersive X-ray Analysis

EDS: Energy Dispersive X-ray Spectroscopy

EIS: Electrochemical Impedance Spectroscopy

FESEM: Field Emission Scanning Electron Microscopy

FFT: Fast Fourier Transform

FTIR: Fourier Transformed Infrared

GC: Glassy Carbon or Gas Chromatography

GO: Graphene Oxide

HER: Hydrogen Evolution Reaction

LSV: Linear Sweep Voltammetry

NCs: Nanocrystals

OER: Oxygen Evolution Reaction

PET: Polyethylene Terephthalate

PXRD: Powder X-ray Diffraction

PEM: Proton Exchange Membrane

RHE: Reversible Hydrogen Electrode

RPM: Revolution Per Minute

SC: Semiconductor

STP: Standard Temperature and Pressure

TEM: Transmission Electron Microscopy

TGA: Thermo Gravimetric Analysis

HRTEM: High Resolution Electron Microscopy

XPS: X-ray Photoelectron Spectroscopy

BJH: Barrett-Joyner-Halenda

BET: Brunauer-Emmett-Teller

CB: Carbon black

CV: Cyclic voltammogram

DC: Direct current

DMC: Dimethyl carbonate

EC: Ethylene carbonate

EV/HEV: Electric and hybrid electric vehicles

ICP-OES: Inductively coupled plasma optical emission spectrometry

JCPDS: Joint Committee on Powder Diffraction Standards

NMP: N-methylpyrrolidinone

PVDF: Polyvinylidene fluoride binder

SAED: Selected area electron diffraction

SEM: Scanning electron microscopy

wt.%: Weight percentage

Table of Contents

1. Introduction

1.1 N-doped Carbon nanomaterials.....	
1.1.1 Preparation of N-doped Carbon nanomaterials.....	
1.1.2. Synthesis of Metal and N doped graphenic carbon nanocomposites	
1.2 Synthesis of Metal Nanocrystals (NCs)	
1.2.1 Colloidal Synthesis	
1.2.2 Solid State Synthesis	
1.3 Synthesis of Metal and N doped graphenic carbon nanocomposites.....	
1.4 Batteries	
1.4.1 Basic Principle of Lithium – ion Batteries	
1.4.2 Voltage	
1.4.3 Capacity.....	
1.4.4 Energy density	
1.4.5 Power	
1.5 Basic Principle of Electrochemical Hydrogen Evolution Reaction (HER)	
1.5.1 Mechanism of Electrochemical Hydrogen Evolution Reaction (HER)	
1.5.2 Tafel Slope	
1.5.3 Stability of Catalyst	
1.5.4 Faraday Efficiency	

References

2. Germanium-Graphitic Nano-composite, Li-ion Battery Application

2.1 Introduction	
2.2 Experimental Section	

2.2.1 General Remarks	
2.2.2 Synthesis of Ge/NG	
2.2.3 Synthesis of Ge/NG/C	
2.2.4 Characterization	
2.2.5 Electrochemical Measurements	
2.3 Results and Discussion	
2.3.1 Preparation of Ge/NG Nanocomposite	
2.3.2 Structural and Microscopic Analysis	
2.3.3 Electro chemical properties	
2.4 Summary	

References

3. Synthesis and Characterisation of N-rich Carbon Nanosheets and their Application as Anode Material in Li-ion Battery

3.1 Introduction

3.2 Experimental Section

- 3.2.1 General Remarks
- 3.2.2 Synthesis of CRT
- 3.2.3 Synthesis of C500
- 3.2.4 Synthesis of C700
- 3.2.5 Characterization
- 3.2.6 Electrochemical Measurements

3.3 Results and Discussion

- 3.3.1 Preparation of CRT
- 3.3.2 Structural and Microscopic Analysis

- 3.3.3 Mechanism for the formation of the CRT
- 3.3.4 C700, C500 Characterisation and properties
- 3.3.5 C700, C500 Characterisation and properties

3.4 Electro chemical properties

- 3.4.1 C500 electrochemical performance
- 3.4.2 C700 electrochemical performance

3.5 Summary

References

4. Simultaneous Synthesis and Characterisation of Antimony-Graphitic Nanocomposite and its anode performance in Li ion Battery

4.1 Introduction	
4.2 Experimental Section	
4.2.1 General Remarks	
4.2.2 Synthesis of Sb/NG	<u> </u>
4.2.3 Synthesis of Sb/NG/C	
4.2.4 Instrumentation detail for characterization and electrochemical measurements	
4.3 Results and Discussion	
4.3.1 Preparation of Sb/NG Nanocomposite	
4.3.2 Structural and Characterizations Analysis	
4.3.3 Electrochemical Measurements	
4.4 Summary	

References

Appdindix

Cobalt-Graphitic Nano-Composite, Characterization and HER Performance

5.1 Introduction	
5.2 Experimental Section	
5.2.1 General Remarks	
5.2.2 Synthesis of Co/NG	
5.2.3 Synthesis of Co/NG/C	
5.2.4 Characterization	
5.2.5 Electrochemical Measurements	
5.3 Results and Discussion	
5.3.1 Preparation of Co/NG Nanocomposite	
5.3.2 Structural and Microscopic Analysis	
5.3.3 Electro chemical properties	
5.4 Summary	
References	

Copy right declarations

Chapter 1

Introduction

1.1 N-doped Carbon nanomaterials

The excellent optical, mechanical, and electrical properties of nanomaterials have attracted considerable attention for application in improving the next-generation energy storage and conversion devices. The size, shape, dimensions, surface area, and porosity of materials play important roles in energy storage and conversion, catalysis, and sensing applications.¹⁻³ The need for novel materials with outstanding electrochemical properties has increased due to the rapid growth of energy storage and conversion devices, such as portable electronics devices, hybrid renewable devices, smart grid devices, and transport sector devices.² The physical and chemical behaviours of two-dimensional (2D), one-dimensional (1D), zero-dimensional (0D) carbon materials depend on their inherent properties, size, and structure. These nanostructures consist of sp^2 -bonded hydrocarbons, whose properties are different.⁴ Many nanomaterials and noble metals show superior electrocatalytic properties in hydrogen evolution reaction.^{2-3, 6} Main-group and transition metal nanoparticles exhibit efficient electrochemical properties required for energy storage, conversion, gas storage, and electrocatalysis; for example, graphene-based carbon nanocomposites are good electrode materials.^{4, 7-10} The electrochemical energy storage properties of a material are important for developing high-performance energy storage devices. Nanocomposite materials with high conductivity and catalytic activity have received much attention from researchers due to their decreased electron traveling length, surface area, and precise structure. Meanwhile, noble-metal nanoparticles have been few and have suffered from poisoning.^{6,8} Transition and main-group metals have shown superior electrochemical properties; however, they have poor stability for potential application in energy storage and conversion.⁸ Therefore, the abundance, stability, and environment-friendliness of carbon materials have made them promising materials in this regard. The stability of carbon materials in acidic or basic media over a wide range of temperatures makes them good electrode materials in device applications.^{4, 8, 10} Consequently, carbon nanomaterials have been used in a wide range of applications, such as solar cells,¹¹ electrochemical double-layer capacitors,^{2,4} fuel cells, and lithium-ion batteries. Among all carbon allotropes, two-dimensional carbon nanostructures have been prominent in electrochemical energy storage applications.¹⁶ These are composed of a single monolayer of sp^2 -hybridized carbons made into a two-dimensional (2D) planar lattice with high mobility of charge carriers (200,000 cm^2/Vs , quantum Hall effect, and huge theoretical surface area (2630 m^2/g)).¹⁶ However, the electrical properties of carbon materials can be altered by elemental doping.¹⁷ Doping can be achieved by either substituting the carbon lattice or

adsorbing molecules onto the carbon surface. This can generate band gaps in the carbon materials, resulting in high-performance energy storage and conversion devices.^{18, 19} Various heteroatoms, like N, B, and S, have been used to impart excellent electrochemical properties to graphene by doping. Among these, N-doped graphene has shown good electrocatalytic activity during oxygen reduction in fuel cells,^{30, 31} excellent cycling stability, rate capability in lithium-ion battery,^{32, 33} and suitable capacitance for high performance supercapacitors applications.²⁵⁻²⁹ The nitrogen atoms in this doped graphene exist as graphitic, pyrrolic, pyridinic, and oxidised (Figure 1.1),³⁴ and are responsible for the properties of the N-doped graphene. The role of the N atoms in increasing capacitance or producing catalytically active sites in N-doped graphene remains controversial,³⁵⁻³⁶ and have been studied based on quantum mechanical calculations³⁷⁻³⁹ and experimental investigations,^{27, 40} The capacitance is increased by doping pyridinic, pyrrolic, and graphitic nitrogen atoms, whereas catalysis of oxygen reduction reaction is enhanced by doping pyridinic and graphitic nitrogen atoms, which improve the adsorption of O₂ onto the neighbouring carbon atoms, thereby promoting the four electron pathway.⁴¹⁻⁴⁴ Lithium-ion batteries have been extensively explored for use in energy storage devices. Fast development of electric vehicles and smart grids have encouraged further progress in improving the cycling stability, rate capability, and energy density of lithium-ion batteries. The nitrogen-doping approach is helpful in adjusting the properties to obtain high-energy-density rechargeable lithium-ion batteries. First, the nitrogen atom is more electronegative than the carbon element since it has a lone pair. Therefore, it has higher electrochemical activity. Thus, the negative charge density, which leads to stronger interaction with positive particles, increases less with increase in the adjacent carbon atom electron density. This improves the interaction with negative charge. Second, nitrogen-doping improves the electrical conductivity of carbon nanomaterials, particularly N-doped graphene and carbon nanotubes (CNTs).⁴⁵⁻⁴⁶

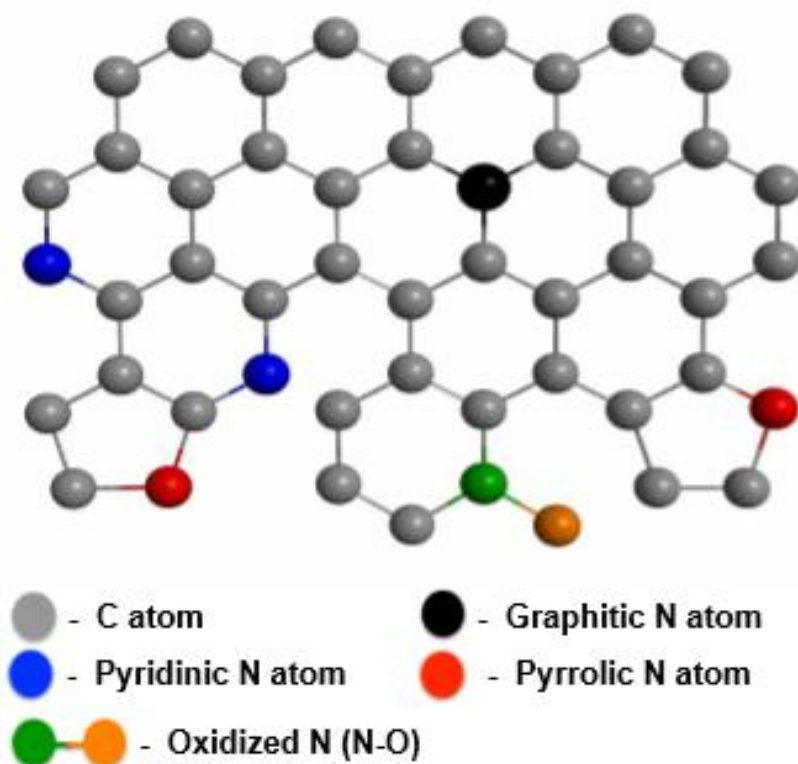


Figure 1.1 Schematic structure of Nitrogen-doped graphene.

1.1.1 Preparation of N-doped Carbon nanomaterials

Large-scale synthesis of nitrogen doped carbon nanomaterials with a higher atomic percentage of N is important for achieving a high ratio of pyridinic N and graphitic N. These sites are responsible for the excellent performance of the N-doped carbon nanomaterials. The synthesis method and nitrogen source are important in obtaining different types of nitrogen bonding configurations and required percentage of nitrogen in N-doped carbon nanomaterials. The nitrogen sources are mostly acetonitrile,⁴⁷ pyridine,⁴⁸ and ammonia,⁴⁶⁻⁴⁸ with the nitrogen doping achieved through chemical vapour deposition (CVD) or high-temperature annealing. The resulting nitrogen doped carbon nanomaterials are useful in lithium batteries, oxygen reduction⁴⁹ and hydrogen evolution reactions, and in field effect transistors.⁴⁸ However, a high percentage of atomic nitrogen in the doped carbon nanomaterials is difficult to obtain via CVD. Obtaining large quantities of material using this method is also difficult because it uses gaseous or liquid sources of nitrogen. In addition, the method also suffers from contamination of the metal catalyst and utilises poisonous starting materials. Meanwhile, a higher percentage of nitrogen (~9 at%) is obtained from the co-

pyrolysis of graphene or graphene starting materials with a solid nitrogen source. The solid nitrogen sources are melamine⁵⁵ and cyanamide.⁵¹ Catalysts are not required in this method; therefore, it is more attractive for producing large quantities of material.⁵⁷ However, cyanamide requires a surfactant to bind it to the carbon during the synthesis of N-doped carbon materials, while melamine has low surface area.⁵¹ Meanwhile, the pyrrolic nitrogen⁵¹ plays a vital role in increasing the capacitance,³⁷ which does not occur in N-doped carbon synthesized from cyanamide. In addition to cyanamide and melamine, urea is widely used as a solid nitrogen source; however, the properties of materials prepared using urea have not been investigated.⁵²⁻⁵⁴ Enough amounts of pyridinic, pyrrolic, and graphitic nitrogen atoms, high surface area, and large pore volume are required to enhance the electrochemical activity and capacitance. The restacking of N-doped carbon sheets by van der Waals interactions between adjacent carbon sheets results in the loss of surface area, while loading a large mass on the current collector. Nanoparticles can be used between the N-doped carbon nanosheets to overcome this challenge.⁵⁵⁻⁵⁶ The reassembling of N-doped carbon sheets is the main drawback, which prevents the penetration of electrolyte between the sheets and reduces the surface area, thereby causing reduction in capacitance and electrochemical properties.⁵⁷ Efforts to increase the capacitance of N-doped carbon sheets by structural modifications are on-going.⁵⁸⁻⁶¹ Therefore, the large surface area of N-doped carbon materials with metallic nanoparticles can improve the electrical conductivity by various structural effects, with the support of conjugated nanocomposites to stop the reassembling of the carbon sheets.⁶²⁻⁶⁴ Apart from the noble-metal nanocrystals, main-group and transition metal nanocrystals have shown better electrocatalytic activity and their low price is appropriate for device production for profit applications.⁶² Placing main-group and transition metal nanocrystals between the doped carbon nanosheets improves the electrochemical surface area, which in turn increases the catalytic activity of the material through synergistic effects of the composite. This also aids in building a three-dimensional (3D) structural material; however, it is difficult to maintain a regular shape with strong bonding between the nanocrystals and the N-doped carbon sheets surface. The 2D N-doped carbon nanosheets conjugated with one dimensional (1D) carbon nanotubes (CNTs) utilise C-C bonds, which provide the 3D structure with improved electrolyte permeation and catalytic properties for good stability in energy storage and conversion.⁶⁵⁻⁶⁸ The penetration of ions, which increases with the formation of 3D N-doped building block carbon structure, enables the increase in capacitance and metal ion storage of batteries. This also improves the catalytic activity during hydrogen evolution, oxygen reduction, and oxygen evolution reactions.^{33, 69}

1.2 Synthesis of Metal Nanocrystals (NCs)

There are different methods for the synthesis of semiconductor or metal nanocrystals (NCs), reported in literature, such as electron beam lithography, molecular beam epitaxy, colloidal synthesis,⁷⁰ and solid-state synthesis.⁷¹ The first two methods involve highly complex instrumentation and need highly controlled atmosphere, high vacuum, and high voltage. Meanwhile, colloidal synthesis is cost-effective because it takes place in solution phase.⁷² Solid-state synthesis is also a convenient method because it enables the synthesis of samples on a large scale. However, a furnace is needed because the reactions take place at high temperatures.

1.2.1 Colloidal Synthesis

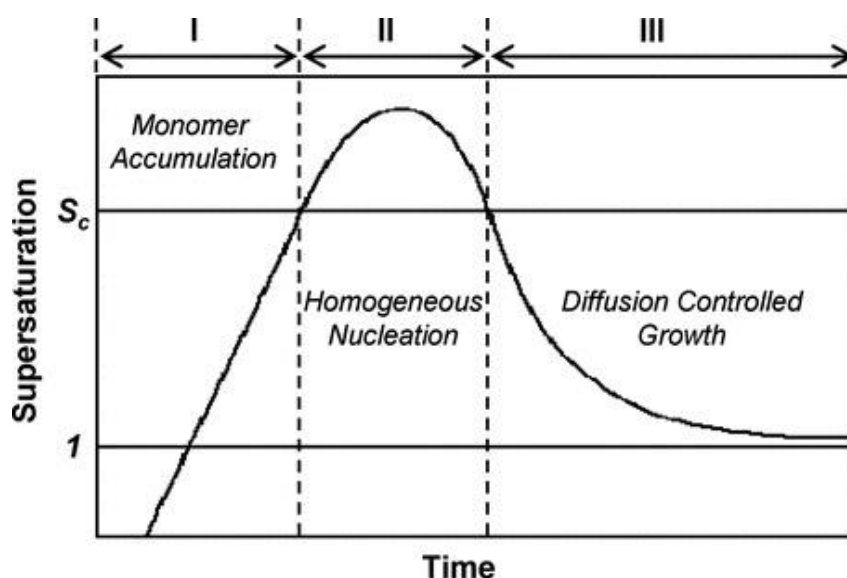


Figure 1.2: LaMer diagram. S_c is the critical supersaturation, the minimum supersaturation level for the homogeneous nucleation to occur. Reprinted with permission from ref.⁷³ Copyright 2011 Wiley-VCH Verlag GmbH & Co.

Colloidal synthesis is well known for producing good-quality semiconductors and metal NCs. Murray et al. introduced for the first time the synthesis of cadmium chalcogenide NCs through a colloidal synthesis method called hot injection.⁷⁴ Generally, the synthesis of semiconductor NCs involves multiple steps. First, the metal ion precursors, in the form of metal complexes and metal salts, are dissolved in high-boiling-point solvents, such as 1-octadecene or trioctyl phosphine oxide. Then, the dissolved metal precursors are heated to a ~ 300 °C. Afterward, anion precursors, such as sulfur or selenium, are dissolved in trioctyl

phosphine and maintained at room temperature. Then, they are quickly injected into the reaction mixture of metal precursors maintained at high temperatures (Figure 1.2). After the injection of the anion precursor into the hot metal precursor solution, the concentration of free monomers in the solution increases rapidly and reaches or exceeds the critical value, according to the LaMer mechanism. Afterward, the monomers undergo instant nucleation, thereby reducing the free monomer concentration in the solution. This results in almost no nucleation occurring due to the low concentration of monomers. However, the nucleated small clusters begin to grow into bigger sized NCs. Figure 1.2 shows all these stages. Further, the high surface-to-volume ratio of small NCs re-dissolved into solution leads to continuous growth of larger NCs at the expense of smaller ones. As a result, the size distribution of NCs becomes narrower, thereby decreasing the free energy of the overall system. This phenomenon is known as the Ostwald refining.⁷⁵

Meanwhile, a different kind of colloidal synthesis method has been used to synthesize the organic-ligand-free inorganic nanocrystals, such as CdS and AgInS₂.⁷⁶ The films of these organic-ligand-free NC systems exhibit better charge transport properties than films of the capped inorganic NCs. However, other materials, such as metal nitrides and metal carbides are difficult to synthesize using the colloidal synthesis method. These metal nitrides and metal carbides have received great attention in the research areas of electrocatalysis and photoelectrocatalysis due to their metallic electronic band structure⁷⁷⁻⁷⁸ and high durability in electrolyte solution. The solid-state method is the most widely used experimental technique for the synthesis of metal nitrides, metal carbides, and other different materials, which requires high temperatures.

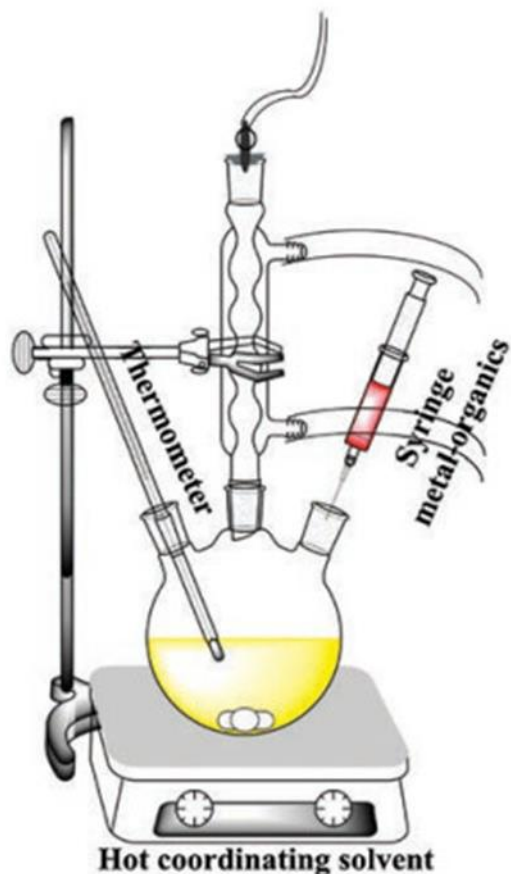


Figure 1.3 Schematic of the apparatus for the hot injection synthesis mode.

1.2.2 Synthesis of metal graphenic nanocomposites

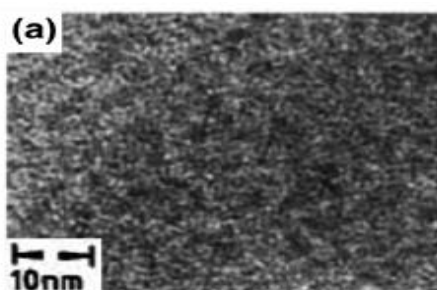
Recently, the colloidal synthesis of anisotropic structures,^{79–85} core-shell nanocrystals, and compositional materials^{82, 84, 86–88} has attracted attention. These inorganic nanocrystals have extraordinary characteristics, which can be obtained by precise size tuning of the material. They have been used in various device applications, such as solar cells,⁹⁰ electrochemical energy storage,^{100–103} electrocatalysis,⁸⁵ electronic circuits,^{98,99} photo detectors,^{91–93} and transistors.^{96, 97, 94, 95} When synthesising a new targeted material, choosing the molecular starting materials is difficult.^{79–85, 104} During the initial trials, researchers spend much time choosing the best combination of starting materials, solvents, and capping agents. In addition, the starting materials must yield pure target materials without any unwanted side reactions and impurities. These materials must also be able to independently tune the reaction rate and growth of the nanocrystal producing a final material that is stable at room temperature. The final material must also dissolve in various solvents and be nonreactive with them. The M-O bonded starting materials are the most used precursors, e.g. acetylacetonates,^{104–107} carboxylates, and organometallic starting materials like carbonyl, alkyl,^{108–111} and M-Si

bonded precursors.¹¹² A clear awareness of the starting material to nanocrystal synthesis pathway, simplistic experimental understanding, and high atom economy, while providing high-purity final materials are important qualities. Recently, a one-pot synthesis of nanocrystals with metal-nitrogen-bonded starting materials has been carried out in situ. Many reports have suggested that the monodisperse nanocrystals^{113–115} are produced from $\text{LiN}(\text{SiMe}_3)_2$ and the respective metal chloride.^{102, 103} Various methods have been investigated for germanium nanocrystal synthesis, including the reduction of solution phase starting material, Ge Zintl phase reaction, organogermanium, and GeI_2 and GeI_4 precursors co-reduction.^{116–119}

Issues during Ge nanocrystals synthesis:

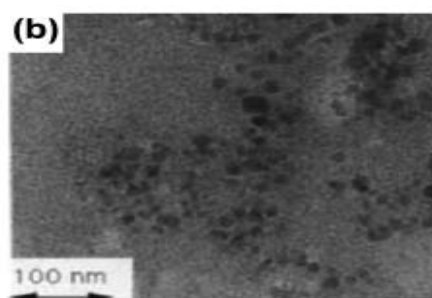
**GeCl_4 , Li naphthalide,
THF, $(\text{CH}_3)_3\text{SiCl}$**

**Room
temperature**



Amorphous GeNP

**Laser
illumination**



Partially Crystalline GeNP

Figure 1.4 Schematic representation of the synthesis of germanium nanoparticles at room temperature by reducing the germanium tetrachloride with alkali metal. TEM images of the (a) amorphous Ge nanoparticles, (b) five-flashed ruby laser-induced partially crystallized germanium nanoparticles. ref.¹⁶⁷ (Copyright 2005, American Chemical Society).

GeCl_4 dissolved in THF has been reacted with lithium naphthalide at room temperature to produce a wide range of distributed amorphous germanium nanoparticles.¹⁶⁶ Then, the dangling bonds on the amorphous Ge nanoparticles are terminated by adding TMSCl ($(\text{CH}_3)_3\text{SiCl}$). The large particles were eliminated by re-dispersion of the dried material in hexane after filtration and amorphous germanium particles of size ~ 2 nm were produced (Figure 1.4a), while also yielding larger particles (Figure 1.4b). The reducing agent used in this method is highly reactive and flammable, and the method produces amorphous nanoparticles.

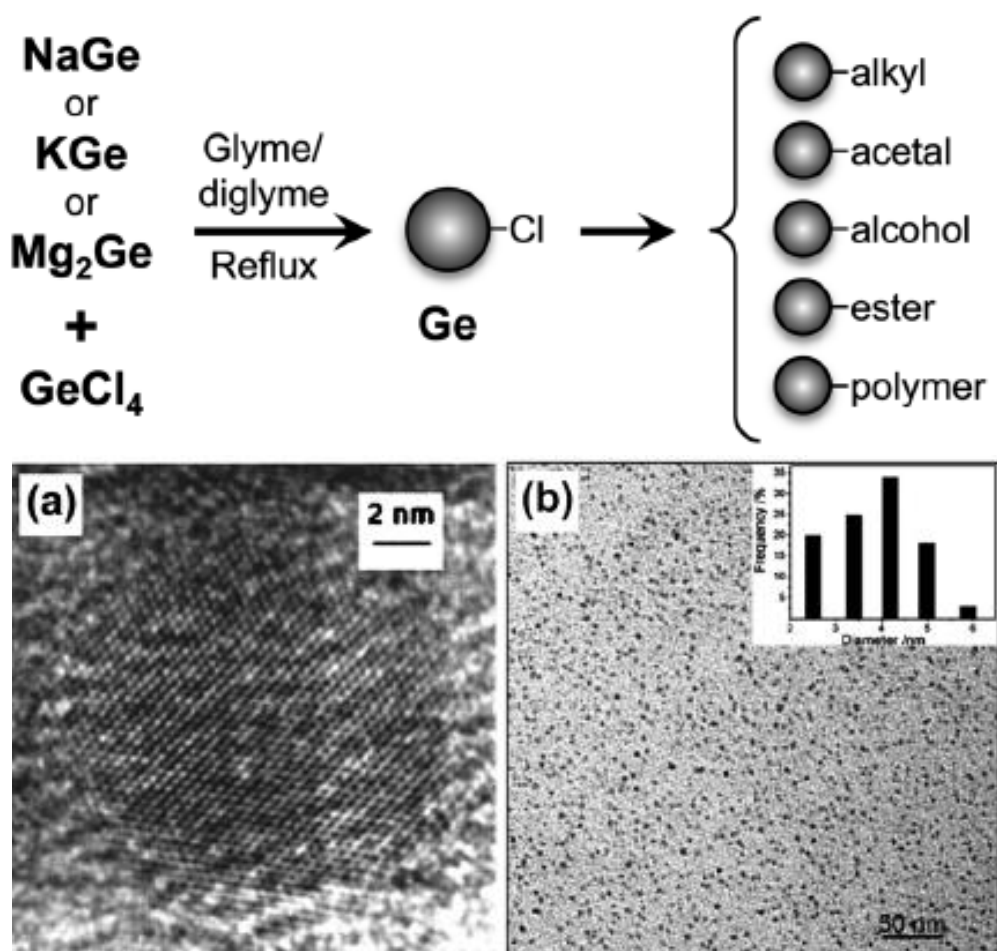


Figure 1.5 Metathesis reaction to produce germanium nanoparticles using germanium Zintl salts and GeCl_4 as precursors. (a) HRTEM of Ge nanoparticles with a size of 15 nm, (b) histogram of Ge nanoparticles synthesised from NaGe Zintl salt, TEM image. ref.¹⁷⁴ (Copyright 2008, Elsevier Inc.).

The NaK alloys have been reacted with GeCl_4 and phenyl- GeCl_3 in heptane using ultrasonication under air and moisture-free conditions to produce germanium amorphous nanoparticles.¹⁷⁰ The amorphous nanoparticles are placed in a sealed vessel and heated to 270 °C for 24–48 h. (Figure 1.5a, b) The materials in this method are not easy to handle and are flammable.

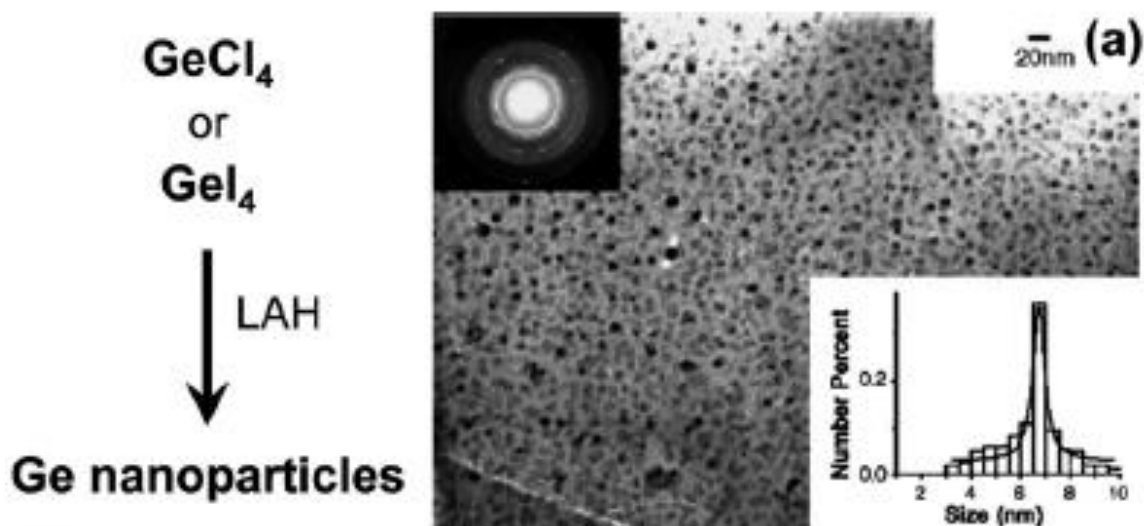


Figure 1.6 GeCl_4 reacted with lithium aluminium hydride (LAH) to produce amorphous colloidal Ge nanoparticles. (a) TEM image, small angle electron diffraction (SAED) pattern, and histogram of the amorphous Ge nanoparticles. ref. ¹⁸⁵ (Copyright 2005, Elsevier B.V.)

GeI_4 reacted with LAH in the presence of cetyl trimethyl ammonium bromide (CTAB) surfactant in toluene solution produces crystalline hydride-terminated germanium nanoparticles. Unlike GeCl_4 which is volatile liquid, GeI_4 is solid and its colour allows the in-situ observation of the process. (Figure 1.6a, b) However, LAH reacts with GeI_4 to produce the highly toxic germane.

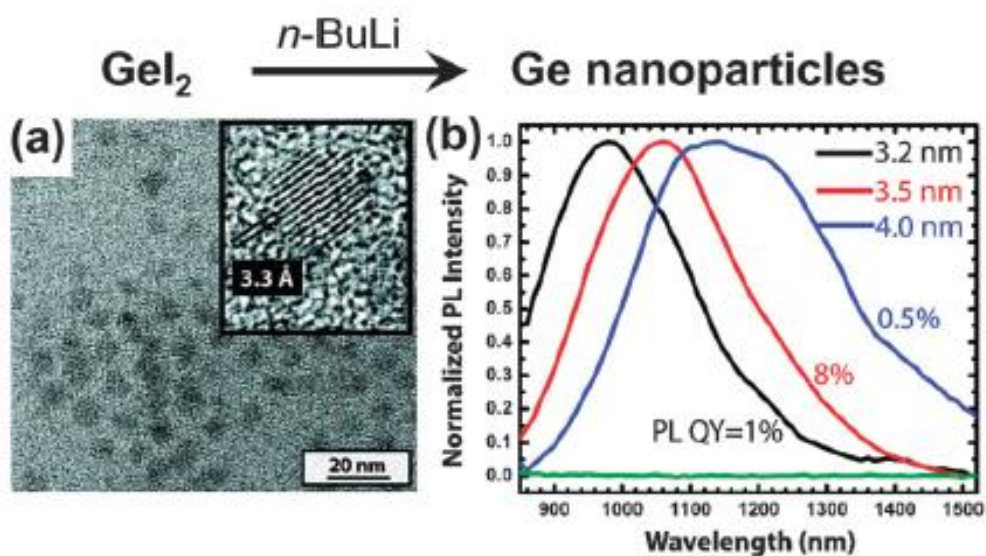


Figure 1.7 GeI_2 reduced by n-butyl lithium to produce colloidal germanium nanoparticles (a) TEM of the germanium nanoparticles (b) Photoluminescence spectra of the octadecene capped germanium nanoparticles with three different sizes. ref. ¹⁹³ (Copyright 2009, American Chemical Society).

The crystalline Ge nanoparticles are synthesised by injecting an n-butyl lithium in octadecene solution into germanium iodide in hexadecylamine at 200 °C. After injection, the temperature is increased to 300 °C for 1 h. (Figure 1.7a) ¹⁹³ n-BuLi is highly flammable; however, this method produces amorphous nanoparticles.

All the methods mentioned above use harsh conditions, flammable materials, and produces low-quality and amorphous nanoparticles. High-quality nanocrystals are important for good-quality devices. Here, we discuss a new method to produce metal nanocrystals.

The large surface area, chemical stability, flexibility, and conductivity of the carbon nanosheets make them suitable for hosting active nanocrystals for better electrochemical applications. Recent reports suggest that a variety of hybrid nanostructures has been designed for use as electrode materials. ^{120–128} N-doped carbon nanosheets are good candidates compared with carbon nanotubes, carbon black, and graphite due to their good nanocrystal dispersion. This improves the electrical conductivity of the overall electrode to achieve high capacitance. ^{120–128} However, during the electrochemical reactions the nanocrystals still undergo agglomeration, which leads to capacity fading when active nanocrystals are directly exposed to the electrolyte. ^{120, 125, 129–131} The best strategy to tackle this agglomeration problem

is to confine the nanocrystal in individual carbon shells and then distribute them on the surface of the carbon nanosheets.²⁵ These mixed conducting 3D nanocomposite networks are important for obtaining high-performance electrochemical applications.^{129, 131, 133}

1.3 Solid-State Synthesis

Solid-state synthesis is a widely used experimental technique for synthesising various polycrystalline materials, such as semiconductors, metals, and dielectrics. In this method, the precursor materials are solids, which do not react together at room temperature. Therefore, to drive the reaction between them, it is necessary to apply higher temperatures often in the range 500–1500 °C.^{67,71} The factors which mainly affect solid state reactions are the: (1) increase in the contact area between the reactant solids, (2) slow rate of nucleation of product, and (3) diffusion of the ions through various phases, particularly, through the product phase. The contact area between the solids is increased by fine grinding of the reactant material or pellets of reactant materials, while the rate of nucleation can be increased by choosing the reactants and products with similar structural properties. The diffusion rate of ions can be increased using two processes i.e., increasing the temperature and introducing defects before or during the reaction.

It is also necessary to choose a suitable sample holder, which does not react with both the reactants and products under the high-temperature conditions used during the synthesis. Typically, alumina and quartz-based crucibles or boats, and noble-metal-based sample holders, such as platinum and gold holders are used. Then, the reactants are heat-treated using a furnace in the last step. The heating programme used depends on the reactivity of the reactant solids in the required atmosphere. Finally, the obtained product are characterized using various experimental techniques. Carbon nanosheets, Ge, Sb, and Co nanocomposites were synthesised using the solid-state method. The detailed of the synthesis are discussed in the following chapters.

1.4 Batteries

A battery is a device that stores chemical energy, which is converted into electrical energy during the discharge process.^{85–90} The major components of a battery are illustrated in Figure 1.4. Unlike supercapacitors, batteries are totally Faradaic devices. The charge storage takes place via oxidation and reduction processes throughout the electrodes. This implies that batteries have bulk storage despite having surface storage. The batteries have a specific

electrochemical potential at which the Faradaic reaction occurs due to the transfer of electrons. The charging and discharging time for batteries is usually longer than those of the electrochemical double layer capacitors (EDLCs) and pseudocapacitors. The capacitive behaviour of the EDLCs is due to the adsorption of ions on the electrode surface; hence, the time scales are in seconds. Meanwhile, the Faradaic reaction occurs in the pseudocapacitors along with intercalation, which is reflected in their charge and discharge nature. The charging and discharging time scales for batteries range from minutes to hours. Batteries have high energy density and a well-defined potential window, which can be tuned based on the chosen electrolyte. The power density of batteries can be enhanced using materials with high rate capabilities. Meanwhile, batteries have wide operating potential range as well. The aqueous electrolytes-based batteries operate at up to 1.23 V because beyond this, water splitting becomes thermodynamically feasible. The potential window can be increased up to 4 V using non-aqueous batteries.

The basic difference between a battery and capacitor is that a capacitor always stores charge on the electrode surfaces irrespective of the chemical processes involved. In contrast, a battery always store charge in the electrode bulk making bulk diffusion an important phenomenon. This results in higher energy density than in supercapacitors. There are various kinds of batteries, such as primary batteries which are basically galvanic cells in which the chemical reaction is irreversible, making the batteries non-rechargeable. There are also rechargeable secondary batteries, such as Ni-Cd, Pb-acid, and Li-ion batteries. Ni-Cd batteries use nickel oxide/hydroxide and metallic Cd as electrodes, which deliver a gravimetric specific energy of 40–60 Wh kg⁻¹ and works at a nominal voltage of 1.2 V. Meanwhile, Pb acid batteries use PbO₂ and Pb as the two working electrodes with an aqueous H₂SO₄ electrolyte delivering a specific energy of 87–90 Whkg⁻¹ at a nominal voltage of 2.1 V. The popularity of the Li-ion batteries over other secondary batteries is due to their nominal voltage (3.6 V using LiCoO₂ and graphite as the cathode and anode, respectively) and specific energy (~230–240 Wh kg⁻¹), which results in higher overall energy density. This energy density can be increased by using Li metal instead of LiCoO₂. However, this comes with different scale-up challenges, such as dendrite formation that causes major safety issues. There are also reports of aqueous and non-aqueous metal air batteries, such as Z-air, Mg-air, Al-air, Li-air, Na-air etc. which use oxygen gas and the corresponding metals as the cathode and anodes, respectively. These batteries have high energy densities, but face major scalability challenges because they use gaseous cathodes.

1.5 Types of Batteries

Batteries are broadly classified based on their function and life cycle. They are divided into two categories i.e., 1) primary batteries and 2) secondary batteries.

Primary Batteries: These batteries have fixed life spans and cannot be recharged once their cycle life is finished. They stop functioning once the chemicals have been used up. Therefore, the components need to be replaced to further generation of energy.¹⁵

Secondary Batteries: These are also popularly known as rechargeable batteries. They have longer life span and can be recharged over multiple cycles. The chemical processes taking place in such batteries are reversible

1.4.1 Basic Principle of Lithium-ion Batteries (LIB)

The Li ion battery era started in 1980 with the contribution of American scientist John B. Goodenough, who proposed the use of a Li-containing oxide LiCoO_2 (LCO) as a cathode material. During the same year, Rachid Yazami from Morocco discovered a graphite anode with a solid electrolyte.⁹⁰⁻⁹⁵ The first Li ion battery prototype was built in Japan in 1985; however, the Li ion battery were commercialised by Sony in 1991. These batteries have an electromotive force up to 3.6 V and are now commercially used for large-scale as well as small-scale applications. Li polymer batteries were also developed using a polymer or gel-based electrolyte to mitigate the issues associated with the use of liquid electrolytes. These liquid electrolytes are generally carbonate-based and flammable, thereby posing a safety threat.

Working principle:

During the discharge process, Li ions present in the LiCoO_2 interlayers between the two CoO_6 octahedra are pulled when a certain amount of current density is applied. The Li ions travel through the electrolyte medium across the separator and are intercalated in the graphite layers forming an intercalation van-der-Waals compound LiC_6 . Since the separator is electrically insulating, it keeps the positive and negative electrodes separate and allows the passage of the Li ions. Meanwhile, the electrons flow through an external circuit. The anode and cathode materials are coated onto the current collectors (e.g. Cu, Al foils etc.). This helps

in collecting the electrons that pass through the external circuit. During the charging process, the reverse mechanism takes place. The Li ions move from the graphite layers and intercalate again in the LiCoO₂ layers.²

1.4.1 Basic Principles of the LIB

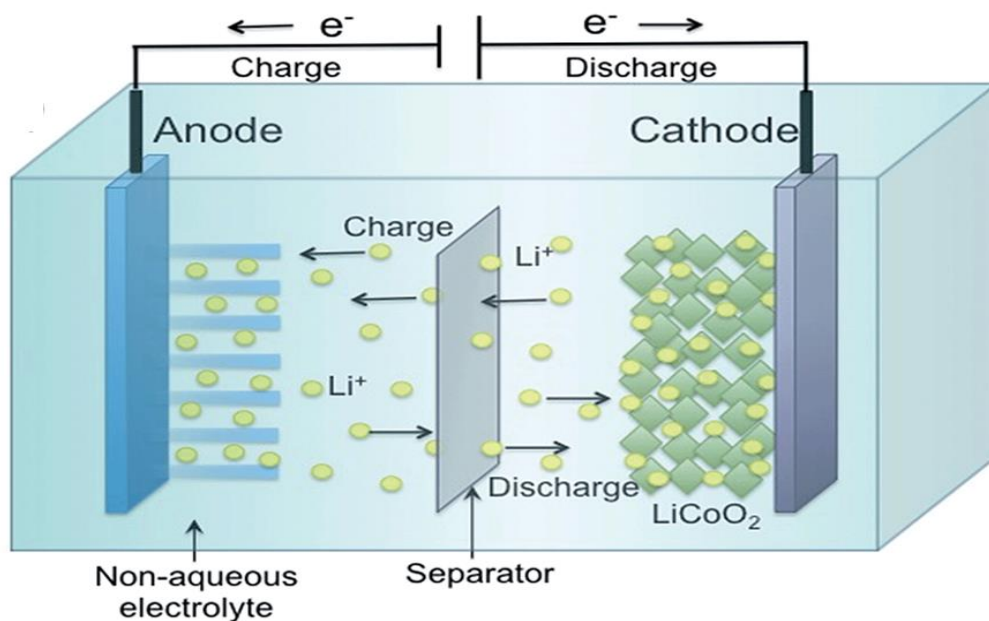


Figure 1.4 Schematic of the electrons and Li⁺ ions transfers during the charge and discharge steps. Reproduced with permission from ref. ⁹⁸ Copyright 2015, *J. Mater. Chem. A*.

1.4.3 Voltage

The chemical potential difference at each electrode is equivalent to the voltage of the battery. The voltage across the electrodes is given by equation (1), when the cell is in the discharge and open circuit states.

$$V_{oc} = \frac{-[\mu_{Li}^{(+)} - \mu_{Li}^{(-)}]}{nF} \quad (1)$$

where n is number of electrons participating in the reaction, F is the Faraday's constant, and $(\mu_{Li}^{(+)})$ and $(\mu_{Li}^{(-)})$ are the chemical potentials.

1.4.2 Capacity

Capacity is the charge that can be stored by the active material. It is generally reported either as gravimetric or volumetric, with volumetric capacity representing the size of the battery instead of its weight. The units of capacity are ampere-hour per gram (Ah/g).

$$C_G = \frac{1000 \times F}{3600 M_w} \text{ mAh/g} \quad (2)$$

$$C_v = \rho C_G \text{ Ah/L or mAh/cm}^3 \quad (3)$$

where F is the Faraday's constant ($9.64853 \times 10^4 \text{ C}$), and M_w and ρ are the molecular weight and density, respectively.

1.4.3 Energy density

The potential when the reaction with lithium occurs and the specific capacity of the material, called energy density (E) are related by equation (4).

$$E = VC_G \quad (4)$$

The unit of energy density is Wh/kg. The equation shows that the energy density increases with increasing voltage or capacity.

1.5 Basic Principles of the Electrochemical Hydrogen Evolution Reaction (HER)

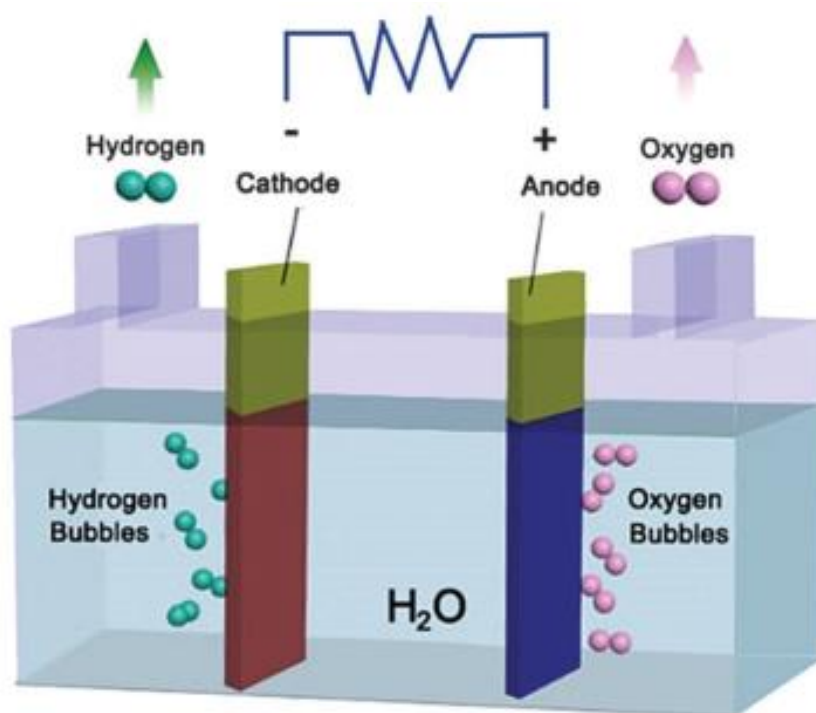
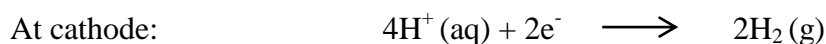


Figure 1.5: Schematic of the electrolyser. Reprinted with permission from ref.¹⁰² Copyright 2015, Royal Society of Chemistry.

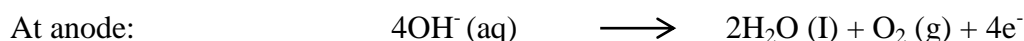
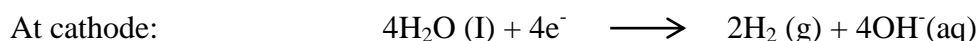
Figure 1.5 shows a typical electrolyser, which consists of three components, viz. a cathode, an anode, and electrolyte (H_2O). When an external voltage is applied across the electrodes,

the water molecules are decomposed into hydrogen gas and oxygen gas at the cathode and anode, respectively. The oxygen gas is released into the environment, while the hydrogen gas is stored for use as fuel. Therefore, the water splitting reaction is divided into two half reactions i.e., the OER and HER, occurring at the anode and cathode, respectively. These reactions can be expressed by the following reactions in acidic, neutral, and basic media.

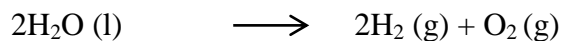
In acidic solution:



In neutral and alkaline medium:



Overall reaction:



Under standard temperature and pressure (STP) conditions, the thermodynamic potential required to convert one molecule of water into hydrogen and oxygen is 1.23 V, irrespective of the media condition i.e., acidic, alkaline, or neutral. This value corresponds to the reversible electrolysis cell voltage and is sufficient to initiate the water splitting process. However, to increase the amount of produced gases, a voltage higher than 1.23 V at 25 °C must be applied from an external source. The excess potential is known as the overpotential (η), which is mainly useful for overcoming the energy barriers at the cathode (η_c), anode (η_a), and other energy barriers (η_{others}), like solution resistance and contact resistance. Thus, practically, the operational voltage of the electrolyser can be described as¹⁰³

$$E_{\text{op}} = 1.23 \text{ V} + \eta_a + \eta_c + \eta_{\text{other}}$$

The function of the electrocatalysts is to reduce the η . The external potential helps form reaction intermediates on the catalyst surface, which increases the electron transfer rate to overcome the high activation energy barriers. Efficient electrocatalyst materials form reaction intermediates at lower overpotential values.

Therefore, the water splitting reaction efficiency can be improved by reducing the overpotentials. The η_a and η_c can be reduced by introducing highly active oxygen evolution and hydrogen evolution catalysts, respectively. Meanwhile, the η_{other} can be reduced by optimising the electrolytic cell design. Increasing the active surface area of the electrode by introducing the nanostructure-based catalysts is a useful strategy to reduce the overpotential. Likewise, the bubbling effect cannot be ignored. During the electrolysis of water, many bubbles are generated on the active surface area of the electrode. Some of these bubbles do not leave the electrode surface, which reduces the active surface area of the electrode and increases the overpotential.

1.5.1 Mechanism of the HER

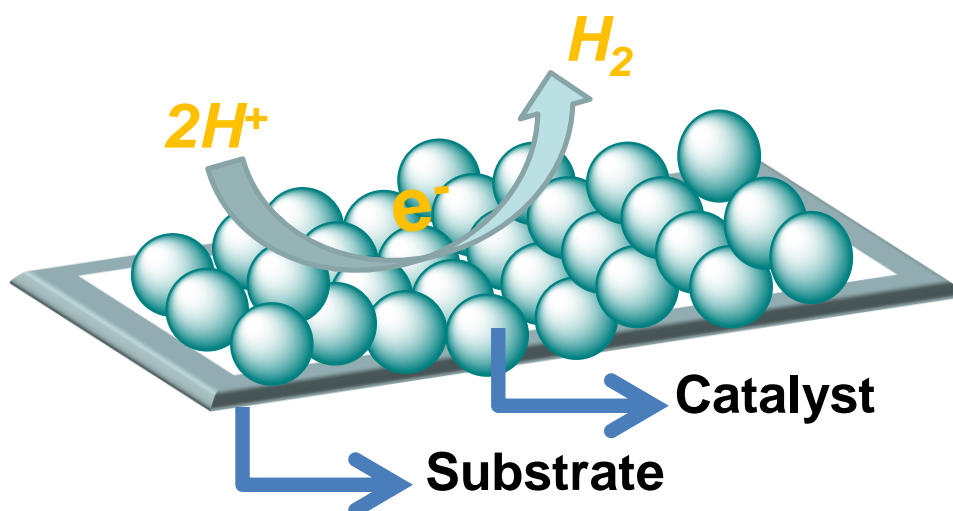
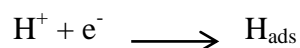


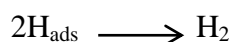
Figure 1.5.1: HER on the catalyst surface in acidic media.

Figure 1.5.1 shows the HER on the catalyst surface in acidic media. Typically, in acidic media, the HER involves two major reaction steps, which take place on the surface of electrode via multiple reaction intermediate pathways, during the production of hydrogen fuel through water splitting. Step 1 involves the adsorption of hydrogen onto the electrode surface through the reaction between an electron and proton. This reaction is termed the Volmer reaction.¹⁰⁴



In step 2, the electrochemical HER occurs. The hydrogen evolution possibly takes place through two different kinds of reaction intermediate pathways. As shown in Figure 1.6, the reaction intermediate path 1 involves the adsorption of hydrogen atoms (H_{ads}) onto the electrode surface coupled with each other, leading to the formation of hydrogen molecule.

This reaction is termed the Tafel reaction, and the overall mechanism is termed the Tafel-Volmer mechanism.¹⁰⁴



Meanwhile, in the reaction intermediate path 2, an adsorbed hydrogen atom and a proton in solution react with an electron or both reaction intermediate 1 and 2 occur, leading to the formation of a hydrogen molecule. This reaction is known as the Heyrovsky reaction, and the mechanism is termed the Volmer-Heyrovsky mechanism.¹⁰⁴ H_{ads} is always present during the HER process regardless of the mechanism by which the HER occurs.

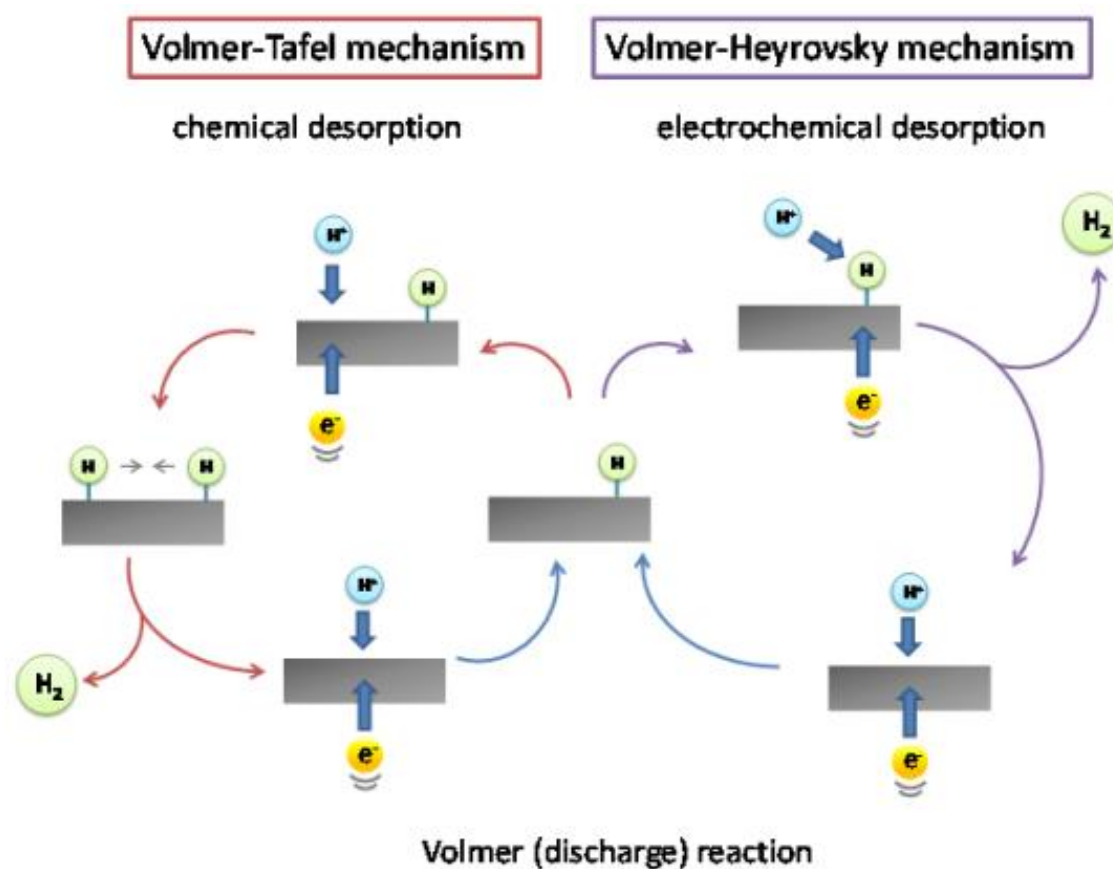
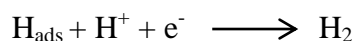


Figure 1.5.2: Electrochemical HER mechanism in acidic medium. Reprinted with permission from ref.¹⁰⁴ Copyright 2014, Royal Society of Chemistry.



ΔG_{H} is the free energy change for the adsorption of hydrogen on hydrogen evolution catalyst. For instance, ΔG_{H} for Pt is approximately zero; hence, Pt is an ideal electrocatalyst for HER. If ΔG_{H} has a large negative value, the H_{ads} was strongly bound to the catalyst surface, resulting in an easier Volmer step but difficult Tafel or Heyrovsky steps. Meanwhile, when the ΔG_{H} is more positive, the H_{ads} interacts weakly with the catalyst surface, resulting in slower Volmer step, which limits the overall HER activity.

To design a new efficient noble-metal-free electrocatalyst for HER, both reaction intermediate steps should be considered. Therefore, the electrocatalyst is expected to have $\Delta G_H \approx 0$.

1.5.2 Tafel Slope

To determine the predominant HER mechanism on the electrocatalyst surface, Tafel slopes are estimated. Typically, the Tafel slope defined as the overpotential (η) is logarithmically related to the current density (J). The linear portion of the Tafel plot can be fitted with the Tafel equation.¹⁰⁴

$$\eta = a + b \log (J/J_0)$$

where, b and J_0 denote the Tafel slope and exchange current density, respectively.

The above Tafel equation gives information on the (1) Tafel slope (b) which is typically related to the catalytic mechanism on the electrode surface, and (2) exchange current density (J_0), which denotes the current density at zero overpotential. The exchange current density describes the intrinsic catalytic activity of the catalyst under equilibrium conditions. Typically, an efficient electrocatalyst has a high exchange current density (J_0) and small Tafel slope (b).

1.5.3 Stability of Catalyst

Good HER activity and stability are crucial parameters of the electrocatalyst in practical applications. Most of the research on catalysts, especially HER catalysts, is often conducted in either extremely acidic solution or extremely basic solution (i.e., pH = 0 or 14). Two methods are used to characterize the stability of HER catalyst.¹⁰¹ The first method is to measure the current density against time (I-T curve). The set current density should be greater than 10 mA/cm² over a long time (> 10 h). The second method is related to cycling stability. In this method, the cycles of cyclic voltammetry or linear sweep voltammetry are repeated by performing cyclic voltammetry. The number of cycles should be maintained above 5000 to evaluate the stability of the electrocatalyst.

1.5.4 Faraday Efficiency

In an electrochemical system, the Faraday efficiency shows the efficiency of the electrons participating in the desired reaction. In a HER experiment, the Faraday efficiency is defined

as the ratio between the experimentally observed H₂ amount and theoretical estimated H₂ amount.¹⁰¹

$$\text{Faraday efficiency (\%)} = \frac{\text{Experimental gas evolution}}{\text{Theoretical gas evolution}} \times 100$$

References:

1. Winter, M., Brodd, R. J. *Chem. Rev.***2004**, *104*, 4245–4269.
2. Liu, C., Li, F., Ma, L. –P. Cheng, H. –M. *Adv. Mater.***2010**, *22*, E28–E62.
3. Arico, A. S., Bruce, P., Scrosati, B., Tarascon, J. M., Schalkwijk, W. V. *Nat. Mater.***2005**, *4*, 366–377.
4. Wang, Y.; Wei, H.; Lu, Y.; Wei, S.; Wujcik, E. K.; Guo, Z. *Nanomaterials***2015**, *5*, 755777.
5. Chen, Z.; Higgins, D.; Yu, A.; Zhang, J. *Environ. Sci.***2011**, *4*, 3167–3192.
6. Manthiram, A.; Murugan, A. V.; Sarkar, A.; Muraliganth, T. *Energy Environ. Sci.***2008**, *1*, 621–638.
7. Jaouen, F., Proietti, E., Lefèvre, M., Chenitz, R., Dodelet, J. –P., Wu, G., Chung, H. T., Johnston, C. M., Zelenay, P. *Energy Environ. Sci.***2011**, *4*, 114–130.
8. Choi, H. –J., Jung, S. –M. Seo, J. M., Chang, D. W., Dai, L., Baek, J. –B. *Nano Energy***2012**, *1*, 534–551.
9. Zhang, X., Wang, B., Sunarso, J., Liu, S., Zhi, L. *WIREs Energy Environ.***2012**, *1*, 317–336.
10. Sun, Y., Wu, Q., Shi, G. *Energy Environ. Sci.* **2011**, *4*, 1113–1132.
11. Ramuz, M. P., Vosgueritchian, M., Wei, P., Wang, C., Gao, Y., Wu, Y. Chen, Y., Bao, Z. *ACS Nano***2012**, *6*, 10384–10395.
12. Simon, P., Gogotsi, Y. *Nat. Mater.***2008**, *7*, 845–854.
13. Zhu, Y., Murali, S., Stoller, M. D., Ganesh, K. J., Cai, W., Ferreira, P. J., Pirkle, A., Wallace, R. M., Cychosz, K. A., Thommes, M., Su, D., Stach, E. A., Ruoff, R. S. *Science***2011**, *332*, 1537–1541.
14. Shao, Y., Liu, J., Wang, Y. Lin, Y. *J. Mater. Chem.* **2009**, *19*, 46–59.
15. Zheng, Y. Jiao, Y., Jaroniec, M., Jin, Y., Qiao, S. Z. *Small* **2012**, *8*, 3550–3566.
16. Geim, A. K., K. S. K. S. *Nat. Mater.***2007**, *6*, 183–191.
17. Liu, H., Liu, Y., Zhu, D. *J. Mater. Chem.***2011**, *21*, 3335–3345.

18. Guo, B., Fang, L., Zhang, B., Gong, J. R. *Insci. J.***2011**, *1*, 80–89.
19. Lv, R., Terrones, M. *Mater. Lett.***2012**, *78*, 209–218.
20. Han, J., Zhang, L. L., Lee, S., Oh, J., Lee, K. –S., Potts, J. R., Ji, J., Zhao, X., Ruoff, R. S., Park, S. *ACS Nano***2013**, *7*, 19–26.
21. Wu, Z. –S., Winter, A., Chen, L., Sun, Y., Turchanin, A., Feng, X., Müllen, K. *Adv. Mater.***2012**, *24*, 5130–5135.
22. Yang, Z., Yao, Z., Li, G., Fang, G., Nie, H., Liu, Z., Zhou, X., Chen, X., Huang, S. *ACS Nano***2012**, *6*, 205–211.
23. Sheng, Z. –H., Gao, H. –L., Bao, W. –J., Wang, F. –B., Xia, X. –H. *J. Mater. Chem.***2012**, *22*, 390–395.
24. Yang, S., Zhi, L., Tang, K., Fang, X., Maier, J., Müllen, K. *Adv. Funct. Mater.***2012**, *22*, 3634–3640.
25. Guo, H. –L., Su, P., Kang, X., Ning, S. –K., *J. Mater. Chem. A* **2013**, *1*, 2248–2255.
26. Qiu, Y., Zhang, X., Yang, S. *Phys. Chem. Chem. Phys.***2011**, *13*, 12552–12558.
27. Sun, L. Wang, L., Tian, C., Tan, T., Xie, Y., Shi, K., Li, M., Fu, H. *RSC Adv.***2012**, *2*, 4498–4506.
28. Wen, Z., Wang, X., Mao, S., Bo, Z., Kim, H., Cui, S., Lu, G., Feng, X., Chen, J. *Adv. Mater.***2012**, *24*, 5610–5616.
29. Haque, E.; Islam, M. M.; Pourazadi, E.; Hasan, M.; Faisal, S. N.; Roy, A. K.; Konstantinov, K.; Harris, A. T.; Minett, A. I.; Gomes, V. G. *RSC Adv.***2015**, *5*, 30679–30686.
30. Lai, L., Potts, J. R., Zhan, D., Wang, L., Poh, C. K., Tang, C., Gong, H., Shen, Z., Lin, J., Ruoff, R. S. *Energy Environ. Sci.***2012**, *5*, 7936–7942.
31. Qu, L., Liu, Y., Baek, J. –B., Dai, L. *ACS Nano***2010**, *4*, 1321–1326.
32. Lin, Z.; Waller, G. H.; Liu, Y.; Liu, M.; Wong, C. –P. *Carbon***2013**, *53*, 130–136.
33. Tian, G. –L.; Zhao, M. –Q.; Yu, D.; Kong, X. –Y.; Huang, J. –Q.; Zhang, Q. Wei, F. *Small***2014**, *10*, 2251–2259.
34. Wang, H., Maiyalagan, T., Wang, X. *ACS Catal.* **2012**, *2*, 781–794.
35. Shao, Y., Sui, J., Yin, G., Gao, Y. *Appl. Catal. B***2008**, *79*, 89–99.
36. Thorum, M. S. Hankett, J. M., Gewirth, A. A. *J. Phys. Chem. Lett.***2011**, *2*, 295–298.
37. Jeong, H. M., Lee, J. W., Shin, W. H., Choi, Y. J., Shi, J. H., Kang, J. K., J. W. Choi, J. W. *Nano Lett.***2011**, *11*, 2472–2477.
38. Zhang, L. L., Zhao, X., Ji, H., Stoller, M. D., Lai, L., Murali, S., Mcdonnell, S., Cleveger, B., Wallace, R. M., Ruoff, R. S. *Energy Environ. Sci.***2012**, *5*, 9618–9625.

39. Ikeda, T., Boero, M., Huang, S. –F., Terakura, K., Oshima, M., Ozaki, J. *J. Phys. Chem. C* **2008**, *112*, 14706–14709.
40. Yang, S., Feng, X. Wang, X., Müllen, K. *Angew. Chem. Int. Ed.* **2011**, *50*, 5339-5343.
41. Reddy, A. L. M., Srivastava, A., Gowda, S. R., Gullapalli, H., Dubey, M., Ajayan, P. M. *ACS Nano* **2010**, *4*, 6337-6342.
42. Biddinger, E. J.; Ozkan, U. S. *J Phys. Chem. C* **2010**, *114*, 15306–15314.
43. Xing, T.; Zheng, Y.; Li, L. H.; Cowie, B. C. C.; Gunzelmann, D.; Qiao, S. Z.; Huang, S.; Chen, Y. *ACS Nano* **2014**, *8*, 6856–6862.
44. Wu, J.; Ma, L.; Yadav, R. M.; Yang, Y.; Zhang, X.; Vajtai, R.; Lou, J.; Ajayan, P. M. *ACS Appl. Mater. Interfaces* **2015**, *7*, 14763–14769.
45. Z. Pan, J. Ren, G. Guan, X. Fang, B. Wang, S. G. Doo, I. H. Son, X. Huang and H. Peng, *Adv. Energy Mater.*, **2016**, *6*, 1600271.
46. Z. S. Wu, W. Ren, L. Xu, F. Li and H. M. Cheng, *ACS Nano*, **2011**, *5*, 5463–5471.
47. Jin, Z., Yao, J., Kittrell, C., Tour, J. M., *ACS Nano* **2011**, *5*, 4112–4117.
48. Geng, D., Chen, Y., Chen, Y., Li, Y., Li, R., Sun, X., Ye, S. Knights, S. *Energy Environ. Sci.* **2011**, *4*, 760-764.
49. Sheng, Z. –H., Shao, L., Chen, J. –J., Bao, W. –J., Wang, F. –B., Xia, X. –H. *ACS Nano* **2011**, *5*, 4350–4358.
50. Wang, H., Zhang, C., Liu, Z., Wang, L., Han, P., Xu, H., Dong, S., Yao, J., Cui, G. J. *Mater. Chem.* **2011**, *21*, 5430–5434.
51. Parvez, K., Yang, S., Hernandez, Y., Winter, A. Turchanin, A., Feng, X., Müllen, K. *ACS Nano* **2012**, *6*, 9541–9550.
52. Lin, Z., Waller, G., Liu, Y., Liu, M., Wong, C. –P. *Adv. Energy Mater.* **2012**, *2*, 884–888.
53. Lei, Z., Lu, L., Zhao, X. S. *Energy Environ. Sci.* **2012**, *5*, 6391–6399.
54. Mou, Z., Chen, X., Du, Y., Wang, X., Yang, P., Wang, S. *Appl. Surf. Sci.* **2011**, *258*, 1704–1710.
55. Zhou, R.; Jaroniec, M.; Qiao, S. –Z. *ChemCatChem*, **2015**, *7*, 3808-3817.
56. Du, J.; Cheng, F.; Wang, S.; Zhang, T.; Chen, J. *Sci. Reports* **2014**, *4*, 4386-4393.
57. Li, D.; Muller, M. B.; Gilje, S.; Kaner, R. B.; Wallace, G. G. *Nat. Nanotechnol.* **2008**, *3*, 101-105.
58. Zhao, Y.; Liu, J.; Hu, Y.; Cheng, H.; Hu, C.; Jiang, C.; Jiang, L.; Cao, A.; Qu, L. *Adv. Mater.* **2013**, *25*, 591-595.
59. Xu, Y.; Sheng, K.; Li, C.; Shi, G. *ACS Nano* **2010**, *4*, 4324-4330.

60. Luo, J.; Hang, H. D.; Huang, J. *ACS Nano* **2013**, *7*, 1464-1471.
61. Zhu, Y.; Murali, S.; Stoller, M. D.; Ganesh, K. J.; Cai, W.; Ferreira, P. J.; Pirkle, A.; Wallace, R. M.; Cychosz, K. A.; Thommes, M.; Su, D.; Stach, E. A.; Ruoff, R. S. *Science* **2011**, *332*, 1537-1541.
62. Choi, H. J.; Jung, S. M.; Seo, J. M.; Chang, D. W.; Dai, L.; Baek, J. B. *Nano Energy* **2012**, *1*, 534-551.
63. Sun, Y.; Wu, Q.; Shi, G. *Energy Environ. Sci.* **2011**, *4*, 1113-1132.
64. Huang, X.; Qi, X.; Boey, F.; Zhang, H. *Chem. Soc. Rev.* **2012**, *41*, 666-686.
65. Wang, Y.; Wu, Y.; Huang, Y.; Zhang, F.; Yang, F.; Ma, Y.; Chen, Y. *J. Phys. Chem. C* **2011**, *115*, 23192-23197.
66. Du, F.; Yu, D.; Dai, L.; Ganguli, S.; Varshney, V.; Roy, A. K. *Chem. Mater.* **2011**, *23*, 4810-4816.
67. Zhao, M. Q.; Zhang, Q.; Huang, J. Q.; Tian, G. L.; Chen, T. C.; Qian, W. Z.; Wei, F. *Carbon* **2013**, *54*, 403-411.
68. Xue, Y.; Ding, Y.; Niu, J.; Xia, Z.; Roy, A.; Chen, H.; Qu, J.; Wang, Z. L.; Dai, L. *Sci. Adv.* **2015**, *1*, 1400198-1400207.
69. Chabi, S.; Peng, C.; Hu, D. Zhu, Y. *Adv. Mater.* **2014**, *26*, 2440-2445.
70. Murray, C. B.; Kagan, C. R.; Bawendi, M. G. *Ann. Rev. Mater. Sci.* **2000**, *30*, 545-610.
71. Allnatt, A. R.; Jacobs, P. W. M. *Can. J. Chem.* **1968**, *46*, 111-116.
72. Park, J.; An, K.; Hwang, Y.; Park, J. G.; Noh, H. J.; Kim, J. Y.; Park, J. H.; Hwang, N.-M.; Hyeon, T. *Nat. Mater.* **2004**, *3*, 891.
73. Kwon, S. G.; Hyeon, T. *Small* **2011**, *7*, 2685-2702.
74. Murray, C. B.; Norris, D. J.; Bawendi, M. G. *J. Am. Chem. Soc.* **1993**, *115*, 8706-8715.
75. Kershaw, S. V.; Susha, A. S.; Rogach, A. L. *Chem. Soc. Rev.* **2013**, *42*, 3033-3087.
76. Kadlag, K. P.; Rao, M. J.; Nag, A. *J. Phys. Chem. Lett.* **2013**, *4*, 1676-1681.
77. Chen, J. G. *Chem. Rev.* **1996**, *96*, 1477-1498.
78. Chen, W. F.; Muckerman, J. T.; Fujita, E. *Chem. Commun.* **2013**, *49*, 8896-8909.
79. Talapin, D. V.; Lee, J.-S.; Kovalenko, M. V.; Shevchenko, E. V. *Chem. Rev.* **2009**, *110*, 389-458.
80. Yin, Y.; Alivisatos, A. P. *Nature* **2005**, *437*, 664-670.
81. Cho, K. S.; Talapin, D. V.; Gaschler, W.; Murray, C. B. *J. Am. Chem. Soc.* **2005**, *127*, 7140-7147.

82. Talapin, D. V.; Nelson, J. H.; Shevchenko, E. V.; Aloni, S.; Sadtler, B.; Alivisatos, A. P. *Nano Lett.* **2007**, *7*, 2951–2959.
83. Milliron, D. J.; Hughes, S. M.; Cui, Y.; Manna, L.; Li, J.; Wang, L.-W.; Alivisatos, A. P. *Nature* **2004**, *430*, 190–195.
84. Zeng, H.; Sun, S. *Adv. Funct. Mater.* **2008**, *18*, 391–400.
85. Murray, C. B.; Norris, D. J.; Bawendi, M. G. *J. Am. Chem. Soc.* **1993**, *115*, 8706–8715.
86. Shevchenko, E. V.; Bodnarchuk, M. I.; Kovalenko, M. V.; Talapin, D. V.; Smith, R. K.; Aloni, S.; Heiss, W.; Alivisatos, A. P. *Adv. Mater.* **2008**, *20*, 4323–4329.
87. Carbone, L.; Nobile, C.; De Giorgi, M.; Sala, F. D.; Morello, G.; Pompa, P.; Hytch, M.; Snoeck, E.; Fiore, A.; Franchini, I. R.; Nadasan, M.; Silvestre, A. F.; Chiodo, L.; Kudera, S.; Cingolani, R.; Krahn, R.; Manna, L. *Nano Lett.* **2007**, *7*, 2942–2950.
88. Cozzoli, P. D.; Pellegrino, T.; Manna, L. *Chem. Soc. Rev.* **2006**, *35*, 1195–1208.
89. Hines, M. A.; Guyot-Sionnest, P. *J. Phys. Chem.* **1996**, *100*, 468–471.
90. Kramer, I. J.; Sargent, E. H. *Chem. Rev.* **2013**, *114*, 863–882.
91. Anikeeva, P. O.; Halpert, J. E.; Bawendi, M. G.; Bulović, V. *Nano Lett.* **2007**, *7*, 2196–2200.
92. Keuleyan, S.; Lhuillier, E.; Brajuskovic, V.; Guyot-Sionnest, P. *Nat. Photonics* **2011**, *5*, 489–493.
93. Clifford, J. P.; Konstantatos, G.; Johnston, K. W.; Hoogland, S.; Levina, L.; Sargent, E. H. *Nat. Nanotechnol.* **2009**, *4*, 40–44.
94. Jong-Soo, L.; Kovalenko, M. V.; Jing, H.; Dae Sung, C.; Talapin, D. V. *Nat. Nanotechnol.* **2011**, *6*, 348–352.
95. Ibanez, M.; Cadavid, D.; Zamani, R.; Garcia-Castello, N.; Izquierdo-Roca, V.; Li, W. H.; Fairbrother, A.; Prades, J. D.; Shavel, A.; Arbiol, J.; Perez-Rodriguez, A.; Morante, J. R.; Cabot, A. *Chem. Mater.* **2012**, *24*, 562–570.
96. Kovalenko, M. V.; Spokoyny, B.; Lee, J. S.; Scheele, M.; Weber, A.; Perera, S.; Landry, D.; Talapin, D. V. *J. Am. Chem. Soc.* **2010**, *132*, 6686–6695.
97. Choi, J. H.; Fafarman, A. T.; Oh, S. J.; Ko, D. K.; Kim, D. K.; Diroll, B. T.; Muramoto, S.; Gillen, J. G.; Murray, C. B.; Kagan, C. R. *Nano Lett.* **2012**, *12*, 2631–2638.
98. Kim, D. K.; Lai, Y. M.; Diroll, B. T.; Murray, C. B.; Kagan, C. R. *Nat. Commun.* **2012**, *3*, 1216.

99. Koh, W. K.; Saudari, S. R.; Fafarman, A. T.; Kagan, C. R.; Murray, C. B. *Nano Lett.***2011**, *11*, 4764–4767.
100. Oh, M. H.; Yu, T.; Yu, S.-H.; Lim, B.; Ko, K.-T.; Willinger, M.-G.; Seo, D.-H.; Kim, B. H.; Cho, M. G.; Park, J.-H.; Kang, K.; Sung, Y.-E.; Pinna, N.; Hyeon, T. *Science***2013**, *340*, 964–968.
101. Bodnarchuk, M. I.; Kravchyk, K. V.; Krumeich, F.; Wang, S.; Kovalenko, M. V. *ACS Nano***2014**, *8*, 2360–2368.
102. He, M.; Kravchyk, K. V.; Walter, M.; Kovalenko, M. V. *Nano Lett.***2014**, *14*, 1255–1262.
103. Kravchyk, K.; Protesescu, L.; Bodnarchuk, M. I.; Krumeich, F.; Yarema, M.; Walter, M.; Guntlin, C.; Kovalenko, M. V. *J. Am. Chem. Soc.***2013**, *135*, 4199–4202.
104. Yarema, M.; Caputo, R.; Kovalenko, M. V. *Nanoscale***2013**, *5*, 8398–8410.
105. Mahler, B.; Spinicelli, P.; Buil, S.; Quelin, X.; Hermier, J.-P.; Dubertret, B. *Nat. Mater.***2008**, *7*, 659–664.
106. Hines, M. A.; Scholes, G. D. *Adv. Mater.***2003**, *15*, 1844–1849.
107. Bodnarchuk, M. I.; Kovalenko, M. V.; Groiss, H.; Resel, R.; Reissner, M.; Hesser, G.; Lechner, R. T.; Steiner, W.; Schäffler, F.; Heiss, W. *Small***2009**, *5*, 2247–2252.
108. Puntès, V. F.; Krishnan, K. M.; Alivisatos, A. P. *Science***2001**, *291*, 2115–2117.
109. Sun, S.; Murray, C. B.; Weller, D.; Folks, L.; Moser, A. *Science***2000**, *287*, 1989–1992.
110. Talapin, D. V.; Rogach, A. L.; Kornowski, A.; Haase, M.; Weller, H. *Nano Lett.***2001**, *1*, 207–211.
111. Peng, X.; Manna, L.; Yang, W.; Wickham, J.; Scher, E.; Kadavanich, A.; Alivisatos, A. P. *Nature***2000**, *404*, 59–61.
112. Battaglia, D.; Peng, X. *Nano Lett.***2002**, *2*, 1027–1030.
113. Wang, F.; Buhro, W. E. *Small***2010**, *6*, 573–581.
114. Zolotavin, P.; Guyot-Sionnest, P. *ACS Nano***2010**, *4*, 5599–5608.
115. Li, W.; Zamani, R.; Rivera Gil, P.; Pelaz, B.; Ibáñez, M.; Cadavid, D.; Shavel, A.; Alvarez-Puebla, R. A.; Parak, W. J.; Arbiol, J.; Cabot, A. *J. Am. Chem. Soc.* **2013**, *135*, 7098–7101.
116. R. Gresback, Z. Holman, and U. Kortshagen, U. *Appl. Phys. Lett.* 2007, **91**, 093119.
117. J. P. Wilcoxon, P. P. Provencio, and G. A. Samara, *Phys. Rev. B* 2001, **64**, 035417/1.
118. B. R. Taylor, S. M. Kauzlarich, H. W. H. Lee and G. R. Delgado, *Chem. Mater.***1998**, *10*, 22

119. E. Muthuswamy, J. Zhao, K. Tabatabaei, M. M. Amador, M. A. Holmes, F. E. Osterloh and S. M. Kauzlarich, *Chem. Mater.***2014**, *26*, 2138.
120. Zhang, L.-S.; Jiang, L.-Y.; Yan, H.-J.; Wang, W. D.; Wang, W.; Song, W.-G.; Guo, Y.-G.; Wan, L.-J. *J. Mater. Chem.***2010**, *20*, 5462.
121. Wang, H.; Cui, L.-F.; Yang, Y.; Sanchez Casalongue, H.; Robinson, J. T.; Liang, Y.; Cui, Y.; Dai, H. *J. Am. Chem. Soc.***2010**, *132*, 13978.
122. Sun, Y.; Hu, X.; Luo, W.; Huang, Y. *ACS Nano***2011**, *5*, 7100.
123. Paek, S.-M.; Yoo, E.; Honma, I. *Nano Lett.***2009**, *9*, 72.
124. Guo, W.; Yin, Y.-X.; Xin, S.; Guo, Y.-G.; Wan, L.-J. *Energy Environ. Sci.***2012**, *5*, 5221.
125. Yang, S.; Feng, X.; Ivanovici, S.; Müllen, K. *Angew. Chem., Int. Ed.* 2010, *49*, 8408.
126. Li, B.; Cao, H.; Shao, J.; Qu, M. *Chem. Commun.***2011**, *47*, 10374.
127. Wang, B.; Wu, X.-L.; Shu, C.-Y.; Guo, Y.-G.; Wang, C.-R. *J. Mater. Chem.***2010**, *20*, 10661.
128. Ding, S.; Chen, J. S.; Luan, D.; Boey, F. Y. C.; Madhavi, S.; Lou, X. W. *Chem. Commun.* **2011**, *47*, 5780.
129. Cao, F.-F.; Guo, Y.-G.; Zheng, S.-F.; Wu, X.-L.; Jiang, L.-Y.; Bi, R.-R.; Wan, L.-J.; Maier, J. *Chem. Mater.***2010**, *22*, 1908.
130. Cao, F.-F.; Deng, J.-W.; Xin, S.; Ji, H.-X.; Schmidt, O. G.; Wan, L.-J.; Guo, Y.-G. *Adv. Mater.***2011**, *23*, 4415.
131. Wu, X.-L.; Jiang, L.-Y.; Cao, F.-F.; Guo, Y.-G.; Wan, L.-J. *Adv. Mater.* **2009**, *21*, 2710.
132. Zhang, W.-M.; Hu, J.-S.; Guo, Y.-G.; Zheng, S.-F.; Zhong, L.-S.; Song, W.-G.; Wan, L.-J. *Adv. Mater.* **2008**, *20*, 1160.
133. Wang, X.-L.; Han, W.-Q.; Chen, H.; Bai, J.; Tyson, T. A.; Yu, X.-Q.; Wang, X.-J.; Yang, X.-Q. *J. Am. Chem. Soc.***2011**, *133*, 20692.
134. J. Wei, Y. Liang, Y. Hu, B. Kong, J. Zhang, Q. Gu, Y. Tong, X. Wang, P. Jiang San, H. Wang, *Angew. Chem. Int. Ed.***2016**,*55*, 12470.
135. X. Liu, I.S. Amiin, S. Liu, K. Cheng, S. Mu, *Nanoscale*, **2016**,*8*, 13311.
136. W. Yang, L. Chen, X. Liu, J. Jia, S. Guo, *Nanoscale*,**2017**, *9*, 1738.
137. W. Zhou, J. Zhou, Y. Zhou, J. Lu, K. Zhou, L. Yang, Z. Tang, L. Li, S. Chen, *Chem. Mater.***2015**, *27*, 2026.
138. B. He, X. Chen, J. Lu, S. Yao, J. Wei, Q. Zhao, D. Jing, X. Huang, T. Wang, *Electroanalysis***2016**, *28*, 2435.

139. L. Chen, L. Zhang, Z. Chen, H. Liu, R. Luque, Y. Li, *Chem. Sci.***2016**, 7, 6015.
140. West, A. R. *Solid State Chemistry and its Applications*, John Wiley and Sons, Student edn, **1998**, ch. 5.
141. J. M. Tarascon, *Philosophical Transactions of the Royal Society a-Mathematical Physical and Engineering Sciences*, **2010**, 368, 3227.
142. M. Armand, J. M. Tarascon, *Nature*, **2008**, 451, 652.
143. M. M. Thackeray, C. Wolverton, E. D. Isaacs, *Energy & Environmental Science*, **2012**, 5, 7854.
144. V. Etacheri, R. Marom, R. Elazari, G. Salitra, D. Aurbach, *Energy & Environmental Science*, **2011**, 4, 3243.
145. J. B. Goodenough, *Accounts of Chemical Research*, **2013**, 46, 1053.
146. N.-S. Choi, Z. Chen, S. A. Freunberger, X. Ji, Y.-K. Sun, K. Amine, G. Yushin, L. F. Nazar, J. Cho, P. G. Bruce, *Angewandte Chemie International Edition*, **2012**, 51, 9994.
147. A. Patil, V. Patil, D. W. Shin, J.-W. Choi, D.-S. Paik, S.-J. Yoon, *Materials Research Bulletin*, **2008**, 43, 1913.
148. J. M. Tarascon, M. Armand, *Nature*, **2001**, 414, 359.
149. M.R. Zamfir, H.T. Nguyen, E. Moyon, Y.H. Lee, D. Pribat, *Journal of Materials Chemistry A*, **2013**, 1, 9566.
150. B. Xu, D. Qian, Z. Wang, Y. S. Meng, *Materials Science and Engineering: R: Reports*, **2012**, 73, 51.
151. M. I. Hoffert, K. Caldeira, G. Benford, D. R. Criswell, C. Green, H. Herzog, A. K. Jain, H. S. Khesghi, K. S. Lackner, J. S. Lewis, H. D. Lightfoot, W. Manheimer, J. C. Mankins, M. E. Mauel, L. J. Perkins, M. E. Schlesinger, T. Volk, T. M. L. Wigley, *Science*, **2002**, 298, 981. 12 J. R. Szczech, S. Jin, *Energy & Environmental Science*, **2011**, 4, 56-72.
152. J.-M. Tarascon, M. Armand, *Nature*, **2001**, 414, 359-367.
153. M. Wakihara, O. Yamamoto, Wiley-VCH, Japan, 1998.
154. H. Takeshita, *Proceedings of the American Power Conference*, 2000, San Diego.
155. K. Caldeira, A. K. Jain, M. I. Hoffert, *Science*, **2003**, 299, 2052.
156. C. K. Chan, X. F. Zhang and Y. Cui, *Nano Letters*, **2008**, 8, 307.
157. B. Laforge, L. Levan-Jodin, R. Salot and A. Billard, *Journal of the Electrochemical Society*, **2008**, 155, A181.

158. T. Song, J. L. Xia, J. H. Lee, D. H. Lee, M. S. Kwon, J. M. Choi, J. Wu, S. K. Doo, H. Chang, W. Il Park, D. S. Zang, H. Kim, Y. G. Huang, K. C. Hwang, J. A. Rogers and U. Paik, *Nano Letters*, **2010**, *10*, 1710–1716.
159. W.J. Zhang, *Journal of Power Sources*, **2011**, *196*, 877-885.
160. D. Linden, T.B. Reddy, Handbook of Batteries; 3 ed.; McGraw-Hill: New York, 2001.
161. D. Linden, T.B. Reddy, Handbook of Batteries; 3 ed.; McGraw-Hill: New York, 2001.
162. Zhao, G.; Rui, K.; Dou, S. X.; Sun, W. *Adv. Funct. Mater.* **2018**, *28*, 1803291.
163. Zou, X.; Zhang, Y. *Chem. Soc. Rev.* **2015**, *44*, 5148-5180.
164. Cook, T. R.; Dogutan, D. K.; Reece, S. Y.; Surendranath, Y.; Teets, T. S.; Nocera, D. G. *Chem. Rev.* **2010**, *110*, 6474-6502.
165. Morales-Guio, C. G.; Stern, L. A.; Hu, X. *Chem. Soc. Rev.* **2014**, *43*, 6555-6569.
166. A. Kornowski, M. Giersig, R. Vogel, A. Chemseddine and H. Weller, *Adv. Mater.*, **1993**, *5*, 634–636.
167. H. W. Chiu, C. N. Chervin and S. M. Kauzlarich, *Chem. Mater.*, **2005**, *17*, 4858–4864.
168. H. W. Chiu and S. M. Kauzlarich, *Chem. Mater.*, **2006**, *18*, 1023–1028.
169. H. Lee, M. G. Kim, C. H. Choi, Y. K. Sun, C. S. Yoon and J. Cho, *J. Phys. Chem. B*, **2005**, *109*, 20719–20723.
170. J. R. Heath, J. J. Shiang and A. P. Alivisatos, *J. Chem. Phys.*, **1994**, *101*, 1607–1615.
171. B. R. Taylor, S. M. Kauzlarich, H. W. H. Lee and G. R. Delgado, *Chem. Mater.*, **1998**, *10*, 22–24.
172. B. R. Taylor, S. M. Kauzlarich, G. R. Delgado and H. W. H. Lee, *Chem. Mater.*, **1999**, *11*, 2493–2500.
173. R. S. Tanke, S. M. Kauzlarich, T. E. Patten, K. A. Pettigrew, D. L. Murphy, M. E. Thompson and H. W. H. Lee, *Chem. Mater.*, **2003**, *15*, 1682–1689.
174. X. C. Ma, F. Y. Wu and S. M. Kauzlarich, *J. Solid State Chem.*, **2008**, *181*, 1628–1633.
175. D. Gerion, N. Zaitseva, C. Saw, M. F. Casula, S. Fakra, T. Van Buuren and G. Galli, *Nano Lett.*, **2004**, *4*, 597–602.
176. N. Zaitseva, Z. R. Dai, C. D. Grant, J. Harper and C. Saw, *Chem. Mater.*, **2007**, *19*, 5174–5178.

177. H. P. Wu, M. Y. Ge, C. W. Yao, Y. W. Wang, Y. W. Zeng, L. N. Wang, G. Q. Zhang and J. Z. Jiang, *Nanotechnology*, **2006**, *17*, 5339–5343.
178. E. J. Henderson, C. M. Hessel and J. G. C. Veinot, *J. Am. Chem. Soc.*, **2008**, *130*, 3624–3632.
179. M. Hoffman and J. G. C. Veinot, *Chem. Mater.*, **2012**, *24*, 1283–1291.
180. E. J. Henderson, M. Seino, D. P. Puzzo and G. A. Ozin, *ACS Nano*, **2010**, *4*, 7683–7691.
181. O. Dag, E. J. Henderson and G. A. Ozin, *Small*, **2012**, *8*, 921–929.
182. H. Gerung, S. D. Bunge, T. J. Boyle, C. J. Brinker and S. M. Han, *Chem. Commun.*, **2005**, 1914–1916.
183. T. J. Boyle, L. J. Tribby, L. A. M. Ottley and S. M. Han, *Eur. J. Inorg. Chem.*, *2009*, 5550–5560.
184. J. P. Wilcoxon, P. P. Provencio and G. A. Samara, *Phys. Rev. B: Condens. Matter Mater. Phys.*, **2001**, *64*, 035417; P. Wilcoxon, P. P. Provencio and G. A. Samara, *Phys. Rev. B: Condens. Matter Mater. Phys.*, **2007**, *76*, 199904(E).
185. H. P. Wu, J. F. Liu, Y. W. Wang, Y. W. Zeng and J. Z. Jiang, *Mater. Lett.*, **2006**, *60*, 986–989.
186. E. Fok, M. L. Shih, A. Meldrum and J. G. C. Veinot, *Chem. Commun.*, **2004**, 386–387.
187. X. M. Lu, B. A. Korgel and K. P. Johnston, *Chem. Mater.*, **2005**, *17*, 6479–6485.
188. J. H. Warner and R. D. Tilley, *Nanotechnology*, **2006**, *17*, 3745–3749.
189. N. H. Chou, K. D. Oyler, N. E. Motl and R. E. Schaak, *Chem. Mater.*, **2009**, *21*, 4105–4107.
190. S. Prabakar, A. Shiohara, S. Hanada, K. Fujioka, K. Yamamoto and R. D. Tilley, *Chem. Mater.*, **2010**, *22*, 482–486.
191. C. B. Jing, X. D. Zang, W. Bai, J. H. Chu and A. Y. Liu, *Nanotechnology*, **2009**, *20*, 505607.
192. J. H. Wu, Y. G. Sun, R. J. Zou, G. S. Song, Z. G. Chen, C. R. Wang and J. Q. Hu, *CrystEngComm*, **2011**, *13*, 3674–3677.
193. D. C. Lee, J. M. Pietryga, I. Robel, D. J. Werder, R. D. Schaller and V. I. Klimov, *J. Am. Chem. Soc.*, **2009**, *131*, 3436–3437.
194. D. A. Ruddy, J. C. Johnson, E. R. Smith and N. R. Neale, *ACS Nano*, **2010**, *4*, 7459–7466.

195. S. C. Codoluto, W. J. Baumgardner and T. Hanrath, *CrystEngComm*, **2010**, *12*, 2903–2909.
196. D. D. Vaughn II, J. F. Bondi and R. E. Schaak, *Chem. Mater.*, **2010**, *22*, 6103–6108.
197. D. J. Xue, J. J. Wang, Y. Q. Wang, S. Xin, Y. G. Guo and L. J. Wan, *Adv. Mater.*, **2011**, *23*, 3704–3707.
198. J. H. Warner, *Nanotechnology*, **2006**, *17*, 5613–5619.
199. Z. C. Holman and U. R. Kortshagen, *Langmuir*, **2009**, *25*, 11883–11889.
200. Z. C. Holman, C. Y. Liu and U. R. Kortshagen, *Nano Lett.*, **2010**, *10*, 2661–2666.

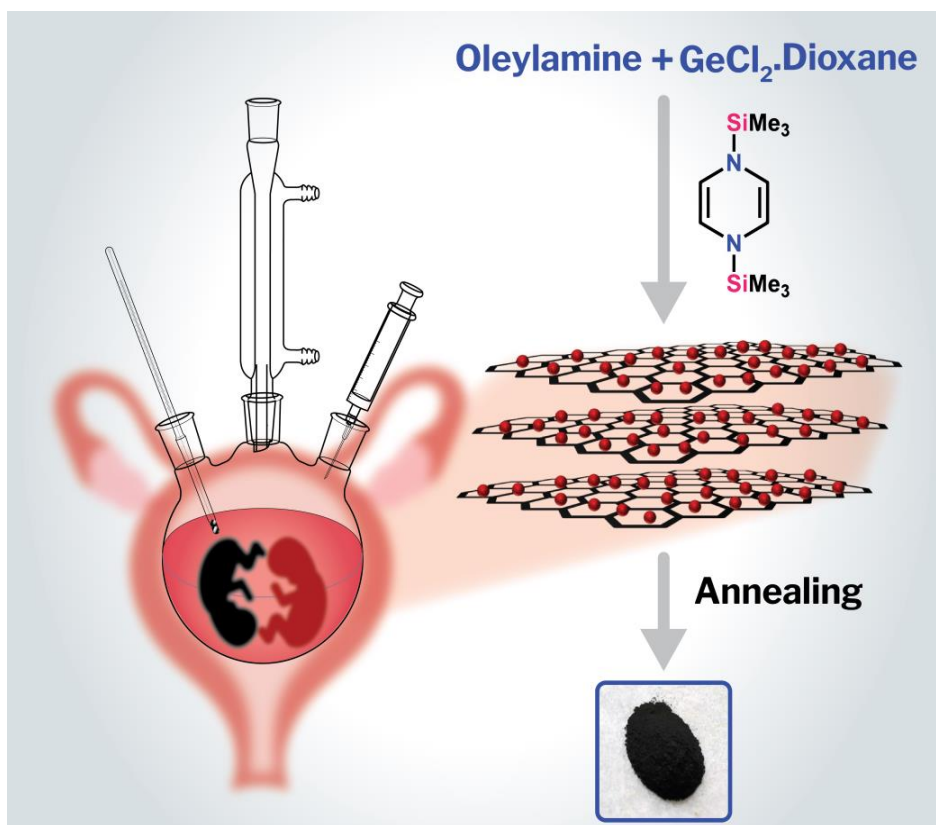
Chapter 2

Coherent Solution-phase Synthesis of a Germanium-Graphitic Nanocomposite and Its Evaluation for Lithium-Ion Battery Anodes: Non-innocent Role of the Mashima Reagent

The following paper has been published based on the work documented in this chapter.

N. Akula, N. Sharma, A. Lohegaonkar, S. B. Ogale and M. Majumdar, Coherent Solution-phase Synthesis of a Germanium-Graphitic Nanocomposite and Its Evaluation for Lithium-Ion Battery Anodes: Non-innocent Role of the Mashima Reagent. *Chem. Asian J.* **2020**, *15*, 585.

Copyright permission has been obtained for complete article from Wiley.



2.1 Introduction

In contemporary research, zerovalent Group 14 element compounds E⁰ (E=Si, Ge) have been successfully isolated vesting upon the donor-acceptor concept.¹ The reduction step in their synthetic methods usually include the use of alkali or alkaline-earth metals and thus involve inevitable metal salt removal during workup. A smart alternate to ease such isolation and purification difficulties is the use of the Mashima reagent.² In 1981 Kaim et. al first reported the bis-silylated nonaromatic reagents.³ Mashima et. al have very ingeniously utilized this organosilicon reagent to reduce early transition metal halides in a salt-free manner and without the formation of over-reduced impurities.⁴ The reaction proceeds due to the thermodynamically favorable formation of Si-Cl bond and aromatic stabilization of the ring. Recently, this reduction method has been applied to main group compounds such as dibismuthene and distibene.⁵ Our group has reported the onepot syntheses of N-heterocyclic germylene and stannylene using 1,4-bis-(trimethylsilyl)-1,4-diaza-2,5-cyclohexadiene as the reductant.⁶ The reaction occurs in a single step and the volatile byproducts trimethylsilylchloride and pyrazine could be easily removed under vacuum yielding

Chapter 2. Coherent Solution-phase Synthesis of a Germanium-Graphitic Nanocomposite and Its Evaluation for Lithium-Ion Battery Anodes: Non-innocent Role of the Mashima Reagent

the heavier carbenes.⁶ This organosilicon reagent proved to be crucial for an elusive reductive cyclization step from bis(α -iminopyridine) stabilized bis(chlorogermylumylidene).⁷ In the nano regime, metal (0) particles have been achieved using this salt-free reduction method for both transition metal chlorides and also main-group chlorides (Ga, In, Sb and Bi).⁸ Among the Group 14 elements, the nanoparticles of Ge are well-reputed to show a wide range of applications in the fields of optoelectronics, bio-imaging and energy conversion and storage.⁹ However, the colloidal syntheses of Ge nano crystals (NC) from Ge(IV) precursors suffer from the requirements of high temperature conditions and strong reducing agents.¹⁰ On the other hand GeI₂ undergoes disproportionation reaction in the presence of capping ligands to generate Ge(0) nanoparticles.¹¹ As a matter of fact, the use of the cheaper GeCl₂.dioxane as the Ge(II) precursor to synthesize Ge nanoparticles has not been sufficiently explored.

In this work, we have considered the reduction of GeCl₂.dioxane 1 to Ge(0) particles using 1,4-bis-(trimethylsilyl)-1,4-diaza-2,5-cyclohexadiene⁴ 2 as the reductant and oleylamine as the capping agent. Under hot-injection conditions, we have obtained a synchronous growth of Ge nanocrystals and Ndoped graphitic nanosheets Ge/NG. Till date, there are no reports on the coherent synthesis of Ge NCs and graphitic nanosheets in the solution phase starting from small molecules. Further, carbon coated Ge NCs immobilized on the N-doped graphitic nanosheets Ge/NG/C were obtained by carbonization in the second step. As an exploratory application, the Ge/NG/C with 57 wt.% of Ge exhibited reasonable anode performance in LIB half-cell.

2.2 Experimental Sections

2.2.1 General Remarks.

Syntheses: All chemicals were purchased from Sigma-Aldrich and used as it is. Tetra hydro furan and pentane were refluxed over sodium/benzophenone and distilled prior to use. Acetone and toluene were distilled prior to use. Oleylamine was stirred overnight at 100°C under vacuum prior to use. 1,4-Bis-(trimethylsilyl)-1,4-diaza-2,5-cyclohexadiene was prepared according to literature procedure. Annealation was done in Nabertherm RHTC 80-710/15.

2.2.2 Synthesis of Ge/NG: GeCl₂.dioxane (0.5 g, 2.16 mmol) dissolved in oleylamine (8 mL, 24.3 mmol) was heated to 200 ° C under argon atmosphere taken in a three-necked flask fitted with a reflux condenser. When the reaction mixture attains the temperature, an oleylamine (4

mL, 12.16 mmol) solution of 1,4-Bis- (trimethylsilyl)-1,4-diaza-2,5-cyclohexadiene (0.75 g, 3.31 mmol) was rapidly injected. The solution colour instantaneously turned intense brown-red. The reaction temperature was increased to 300 °C (ramp rate = 10 °C/min) and kept for one hour at this temperature. Subsequently, the reaction mixture was cooled to room temperature. The solution was then transferred to a centrifuge tube with 2-3 mL of toluene. The Ge/NG was precipitated by adding 20 mL of acetone and separated by centrifugation (9000 rpm for 10 minutes). After decanting the supernatant, the precipitate was resuspended in 5 mL of toluene and 25 mL of acetone was added as the non-solvent. The Ge/NG was separated by centrifugation. This process of dissolution/precipitation/centrifugation was repeated several times until all impurities were removed. This yielded 350 mg of the red-brown solid which was stored in the glove box.

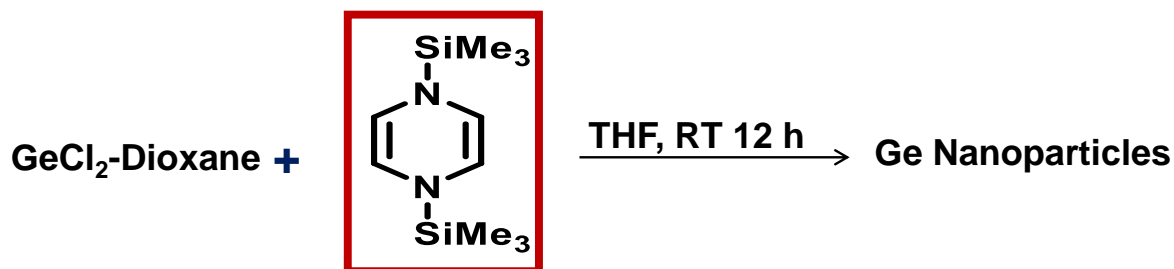
2.2.3 Synthesis of Ge/NG/C: Ge/NG (200 mg) was annealed at 700 °C for two hours under argon containing 5% of hydrogen in a furnace to yield a black powder Ge/NG/C (110 mg). The rate of heating was 2 degree/min.

2.2.4 Characterization: Powder X-ray Diffraction (XRD) of Ge-Graphenic nanocomposites were recorded using a Bruker D8 Advance X-ray diffractometer equipped with Cu K α radiation (1.54 Å). Raman spectra of the nanocomposites were analysed by using LabRAM HR800 from Yvon Horiba. X-ray photoelectron spectroscopy (XPS) data were collected by using PHI 5000 Versa Probe II, FEI Inc. Scanning Electron Microscopy (SEM) was done using FEI Nova Nano 450 SEM. The Brunauer-Emmett- Teller (BET) adsorption measurements for surface area calculation were carried out using Quadrasorb automatic volumetric instrument. Atomic Force Microscopy (AFM) data were collected using Keysight atomic force microscope (model: AFM 5500) by using tapping mode technique. Fourier Transformed Infrared spectroscopy (FTIR) measurements were collected on the pellet of nanocomposites and KBr using Thermo scientific NICOLET 6700 FTIR spectrophotometer. Transmission Electron Microscopy (TEM) images were taken using a JEOL JEM 2100 FS field emission transmission electron microscope at 200 kV. CHN analyses were performed on Elementar vario EL analyzer. Thermogravimetric analysis was performed in air using TGA Perkin-Elmer STA6000.

2.2.5 Electrochemical Measurements: The electrodes were prepared by making a slurry of Ge/NG/C, conducting carbon, and polyvinylidene fluoride (PVDF) binder in the weight ratio

Chapter 2. Coherent Solution-phase Synthesis of a Germanium-Graphitic Nanocomposite and Its Evaluation for Lithium-Ion Battery Anodes: Non-innocent Role of the Mashima Reagent 80:10:10 using N-Methyl-2-Pyrrolidone (NMP) solvent. The slurry was coated onto a Cu foil and kept for drying overnight at 80 °C. The foil was then punched into 1 cm² circular discs. The CR-2032 coin half-cell was assembled using this composite as the working electrode and metallic lithium foil as the counter and reference electrode. The mass of active material loaded on the electrode was 1.0 mg. Whatmann was used as the separator and a commercial electrolyte 1M LiPF₆ in ethylene carbonate: dimethyl carbonate EC: DMC (1:1 volume). All the cells were assembled inside an Argon-filled glove box. Galvanostatic charge-discharge measurements were performed with BTS-Neware (China) 5V-10mA battery tester. The impedance and cyclic voltammetry were performed with VMP3 Biologic system equipped with potentiostat and galvanostat channels.

2.3 Results and Discussion



Scheme: Ge nanoparticles formation.

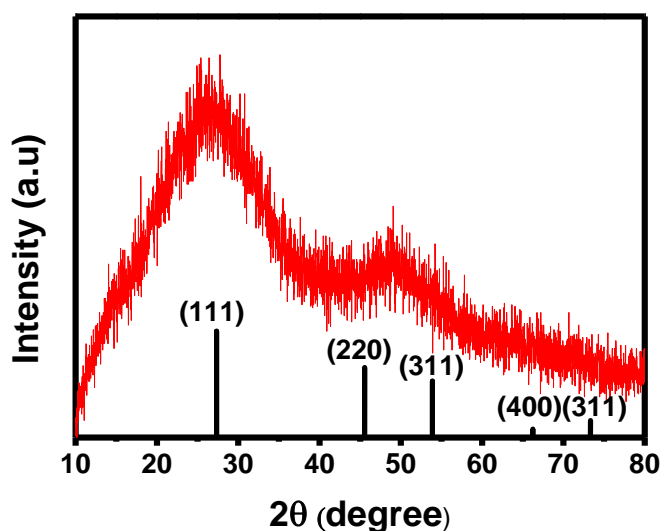


Figure 2.1 PXRD pattern Ge nanoparticles

Under inert atmosphere, the 2.16 mmol of GeCl_2 .dioxane dissolved in THF in a shlenk flask at room temperature. A solution of 3.3 mmol of 1,4-bis-(trimethylsilyl)-1,4-diaza-2,5-cyclohexadiene⁴ in THF was rapidly injected leading to an immediate colour the solution turns dark brownish-red instantaneously, stirred for 24h at room temperature. The dark brown solid was isolated using the solvent/non-solvent technique.¹² The washing and centrifugation were repeated until all impurities were removed and dried. The dark brown powder further chareatarised for XRD, Raman, TEM, TGA.

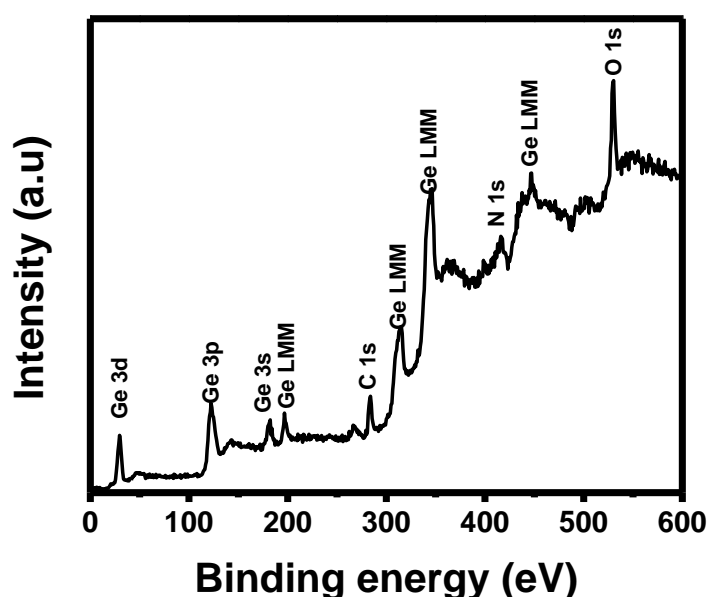


Figure 2.2 survey spectrum of the Ge nano particles

The powder X-ray diffraction (PXRD) pattern (Figure 2.1) of the Ge nanoparticles two broad peaks displays at $2\theta=27.5^\circ$, 47.7° which can clearly tell the formation of amorphous Ge nanoparticles. The survey X-ray photoelectron spectroscopy (XPS) scan shows four obvious signals which can be assigned to Ge, C, N and O elements (Figure 2.2). Raman spectroscopy (Figure 2.3) shows presence of amorphous graphitic nanosheets in the Ge/NG microstructure and there is no clear Germanium crystalline peak at 290 from this which supports the PXRD, confirms the amorphous Ge nanoparticles. The two characteristic peaks at 1355 and 1570 cm^{-1} are in good agreement with the typical optical modes of D band (disorder induced phonon mode) and G band (graphitic band) of C respectively from this the along with there is amorphous carbon also present.

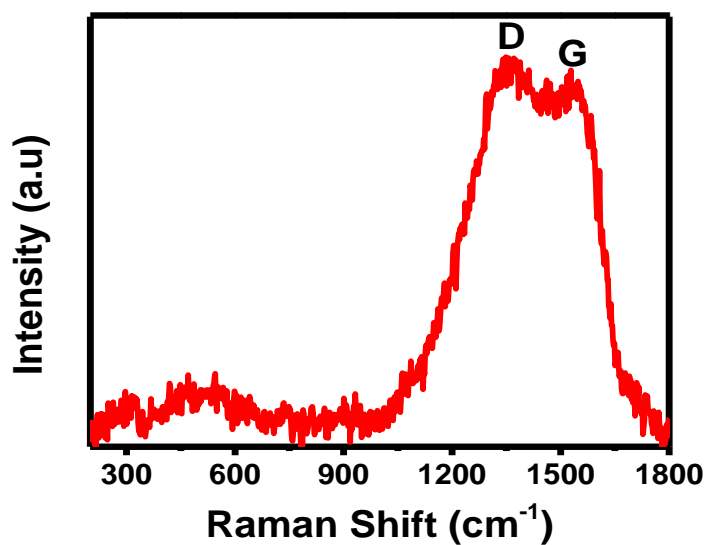


Figure 2.3 Raman spectra of Ge nanoparticles

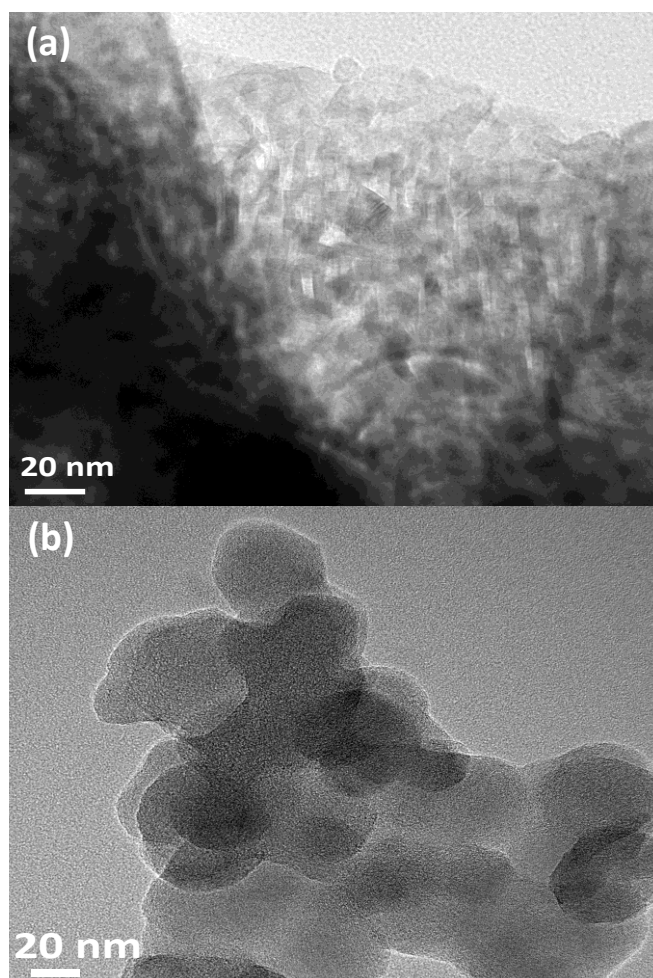


Figure 2.4 (a) TEM image of the amorphous Ge nanoparticles (b) TEM image of the amorphous carbon nanosheets.

Chapter 2. Coherent Solution-phase Synthesis of a Germanium-Graphitic Nanocomposite and Its Evaluation for Lithium-Ion Battery Anodes: Non-innocent Role of the Mashima Reagent

Transmission electron microscopy of Ge nanoparticles (Figure 2.4a, 2.6 a,b) shows the nanoparticles are agglomerated because there is no any capping agent along with Ge nanoparticles there are carbon nanosheets also present which well agreement with Raman spectroscopy. The carbon nanosheets are also agglomerated and the sheets are separated with Ge nanoparticles (Figure 2.4b) FESEM of the Ge nanoparticles also shows the nanoparticles are agglomerated. (Figure 2.5)

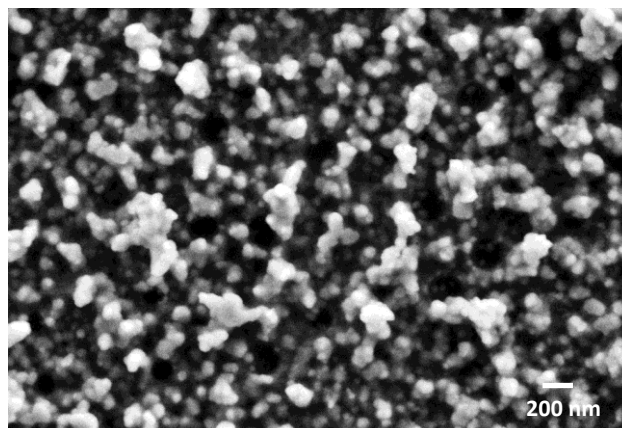


Figure 2.5 FESEM image of Ge nanoparticles.

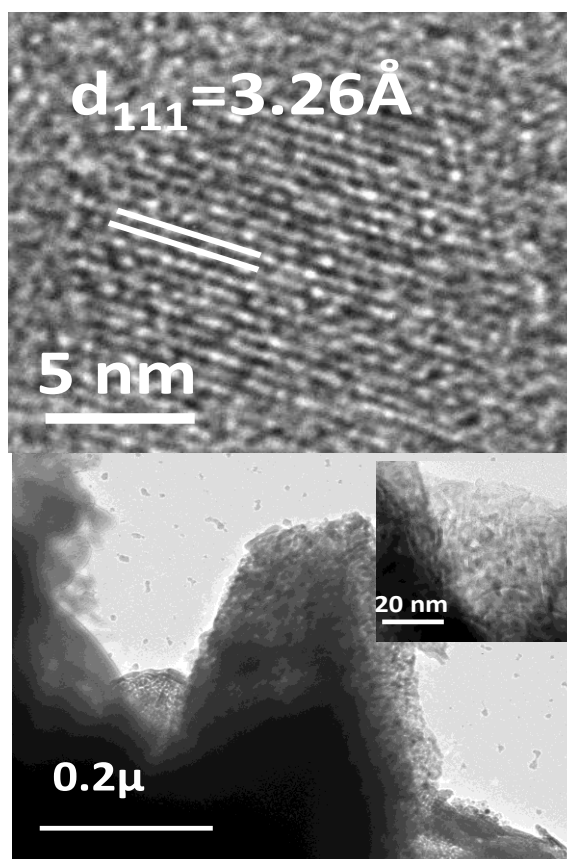


Figure 2.6(a) HRTEM image of the amorphous Ge nanoparticles (b) TEM image of the agglomerated Ge amorphous nanoparticles.

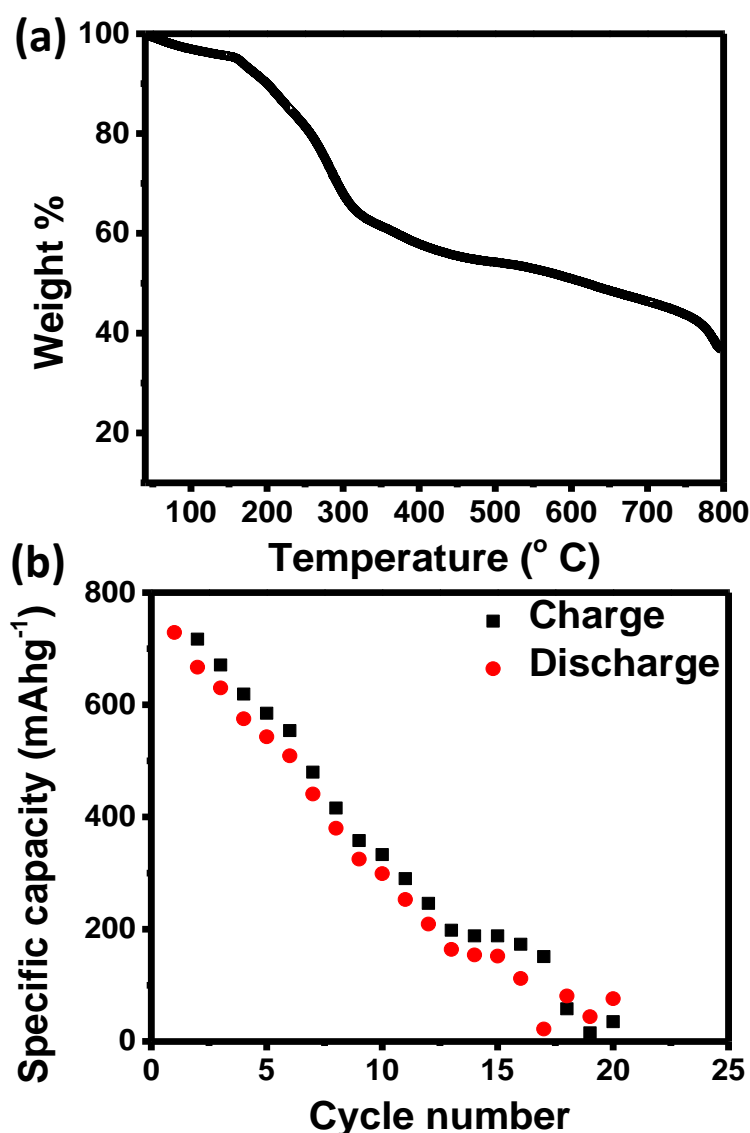


Figure 2.7 (a) TGA of Ge nanoparticles (b) Cycling performance of the Ge nanoparticles in Li ion battery as anode material.

Ge nanoparticles further characterised for thermogravimetric analysis, from this experiment the amount of Germanium 38% (Figure 2.7a). Ge amorphous nanoparticles use as electrode in Li ion battery as anode material. The cycling stability of the material in Li ion battery capacity showed 730 m Ahg⁻¹ and it decreased continuously, at 20th cycle the capacity decreased to 5 m Ah⁻¹.(Figure 2.7b)

The Ge amorphous nanoparticles are not a good candidate for Li ion battery as anode material, due to its amorphous in nature and agglomeration of the nanoparticles which leads to poor conductivity and cycling performance, to get for better formance, need crystalline

Chapter 2. Coherent Solution-phase Synthesis of a Germanium-Graphitic Nanocomposite and Its Evaluation for Lithium-Ion Battery Anodes: Non-innocent Role of the Mashima Reagent nanoparticles with carbon nanosheets. Carbon nanosheets are not only improves the conductivity with increses the cycling performance and rate capability.

2.3.1 Preparation of Ge/NG Nanocomposite

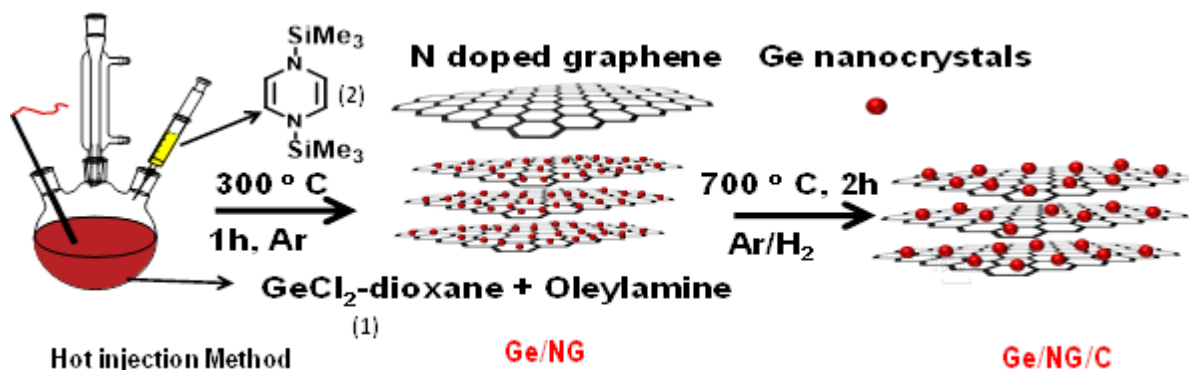


Figure 2.8: Schematic representation of synthesis of Ge/NG and Ge/NG/C nanocomposites.

In a typical reaction under inert atmosphere, the 2.16 mmol of $\text{GeCl}_2\text{-dioxane}$ 1 dissolved in 24.3 mmol of oleylamine taken in a three-necked round bottomed flask was heated to 200°C . When the reaction temperature reached 200°C , a solution of 3.3 mmol of 1,4-bis-(trimethylsilyl)-1,4-diaza-2,5- cyclohexadiene⁴ 2 in 12.16 mmol of oleylamine was rapidly injected leading to an immediate temperature drop to ca. 170°C and the solution turns dark brownish-red instantaneously. After recovery to 200°C , the reaction temperature was raised to 300°C (ramp rate= 10°Cmin^{-1}) and held for one hour at 300°C . After subsequent cooling to room temperature, the dark brown solid was isolated using the solvent/non-solvent technique.¹² The washing and centrifugation were repeated until all impurities such as unbound oleylamine etc. were removed. This method is gram-scalable and the resulting dark brown solid Ge/NG was dried and stored in a glove box. Ge/NG forms stable colloidal suspension in toluene. The burst of homogeneous nucleation followed by steady controlled growth in the hot-injection method led to a high quality monodispersed Ge/NG nanocomposit.(Figure 2.8)

2.3.2 Structural and Microscopic Analysis

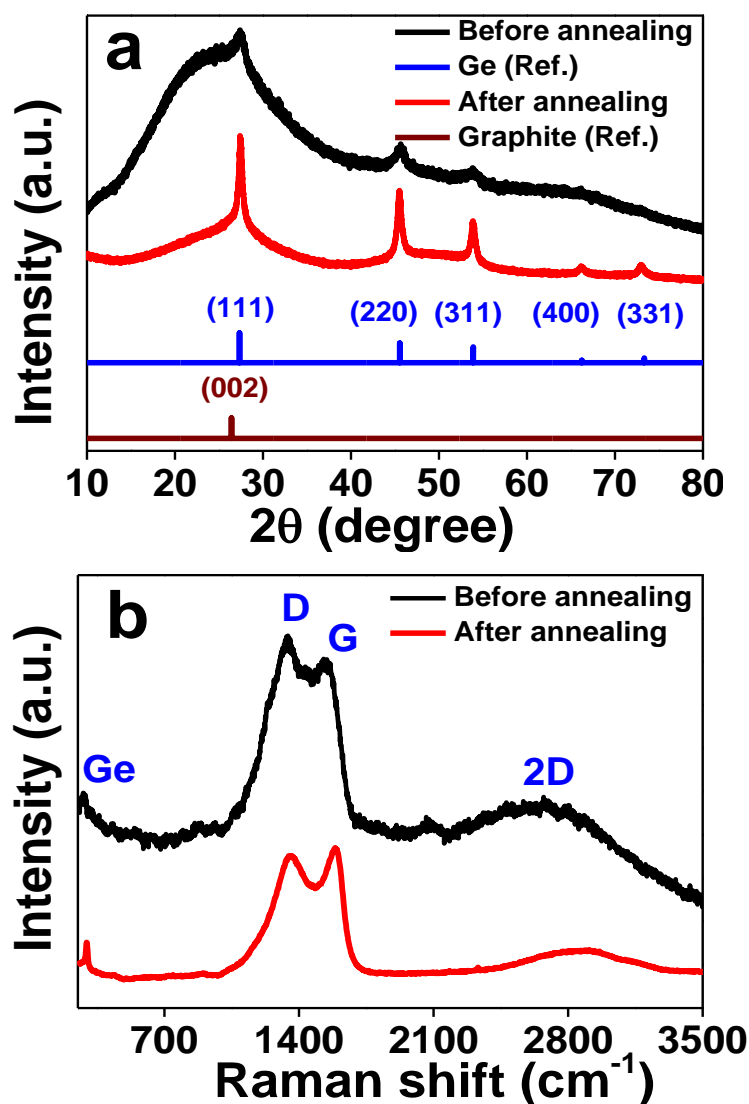


Figure 2.9 (a) PXRD pattern and (b) Raman Spectra of Ge/NG (before annealing) and Ge/NG/C (after annealing)

The powder X-ray diffraction (PXRD) pattern (Figure 2.9a) of the as-synthesized Ge/NG displays clear peaks at $2\theta = 27.5^\circ$, 45.7° and 53.9° which can be well-indexed to the diamond cubic Ge (JCPDS card No. 04-0545).¹³ No GeO_2 phase has been detected in the diffraction pattern. The calculated d-spacing based on the (111) peak is 0.32 nm. A broad diffraction (002) peak in the range 20° – 26° was observed, indicating low degree of graphitization.¹⁴ Left-shift of this peak suggests widened plane spacing due to the defects and disorders of the graphitelike sheet structure.¹⁵ Raman spectroscopy (Figure 2.9b) further authenticated the crystalline phase of Ge and presence of graphitic nanosheets in the Ge/NG microstructure.

The three characteristic peaks at 290, 1342 and 1530 cm^{-1} are in good agreement with the typical optical modes of crystalline Ge, D band (disorder induced phonon mode) and G band (graphitic band) of C respectively.

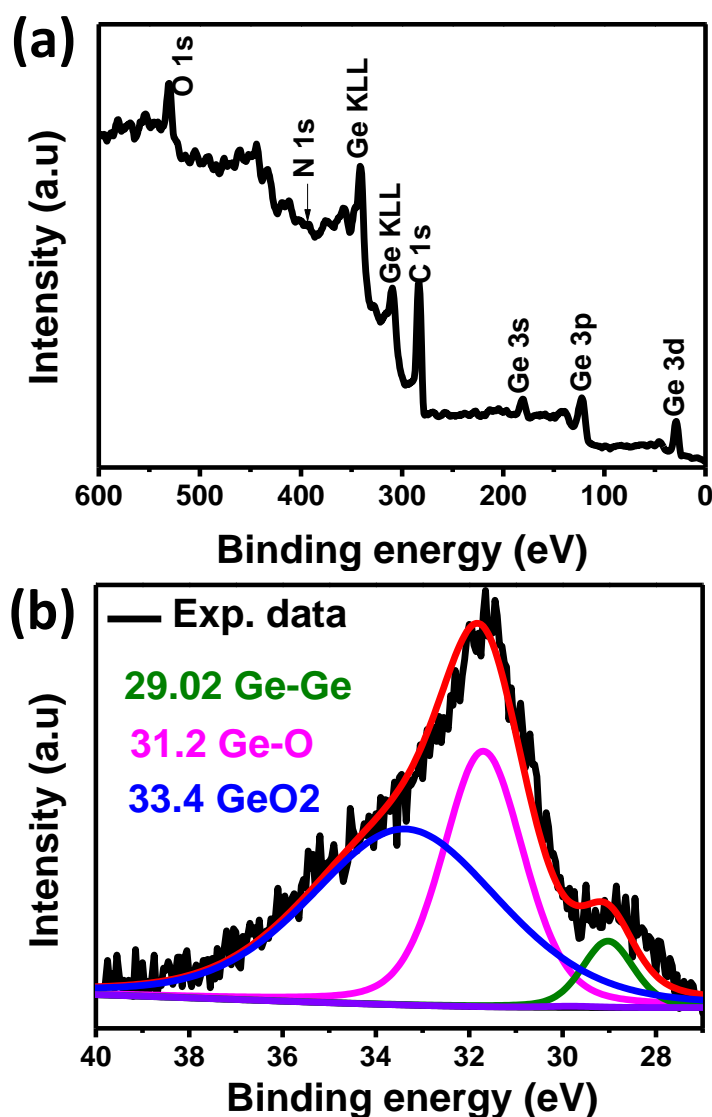


Figure 2.10 (a) survey spectrum; High resolution XPS (b) Ge 3d

The integrated area ratio of D/G 1.86 indicates that the graphitized structure has defects and disorders.¹⁵ A distinct broad 2D peak which is the second order of the D band appears at 2635 cm^{-1} in the Raman spectrum. The survey X-ray photoelectron spectroscopy (XPS) scan shows four obvious signals which can be assigned to Ge, C, N and O elements (Figure 2.10a). The high resolution XPS spectra of Ge 3d shows two broad peaks, one below 30 eV assignable to Ge(0) and the other around 32 eV due to Ge⁴⁺ 3d (Figure 2.10b) which arises due to easy surface oxidation of Ge in air.¹⁶

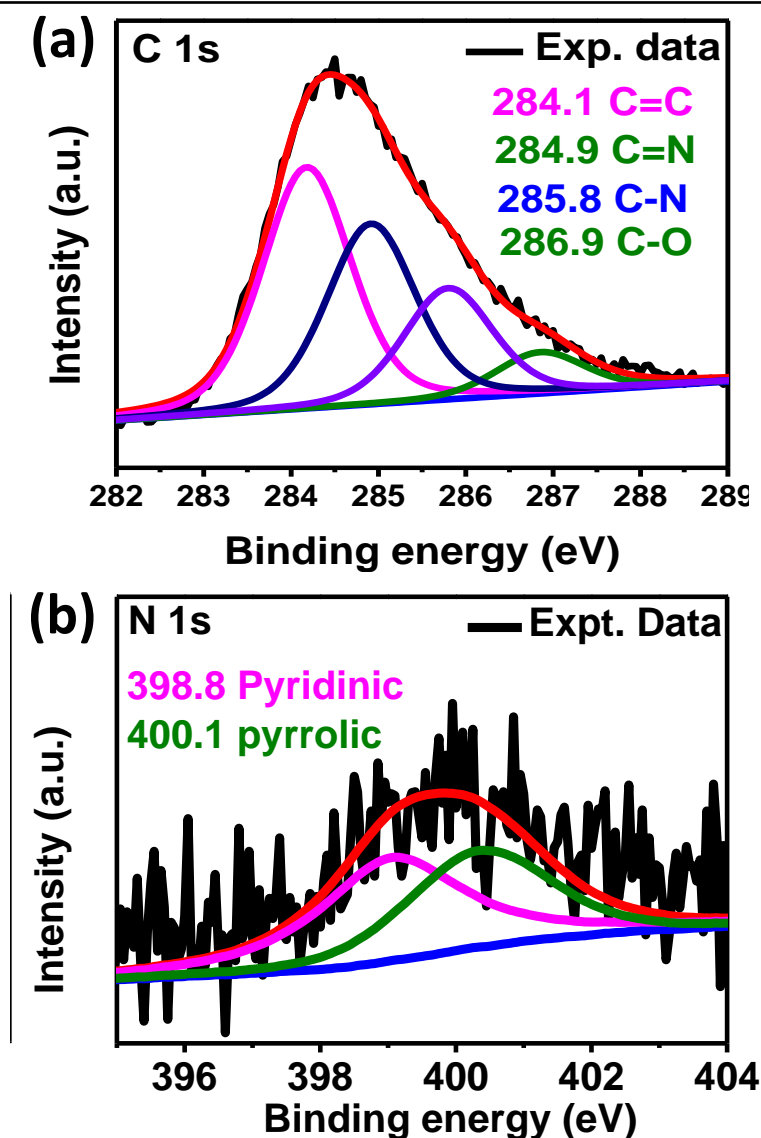


Figure 2.11 High resolution XPS (a) C1s; (b) N1s sp

The fitted XPS spectra of C1s displays four peaks (Figure 2.11a). The main peak at 284.3 eV is assigned to the graphite-like sp^2 C.¹⁷ The other three peaks centered at 284.9 and 285.9 eV correspond to the C=N, and C N groups respectively and at 286.9 corresponds to C O group.¹⁷ The N1s spectra could be de-convoluted into two sub peaks at 398.8 and 400.1 eV corresponding to the pyridinic N and pyrrolic N respectively (Figure 2.11b).¹⁸ The N contents of the graphene is about 3.4 wt.% obtained from CHNS elemental analysis and XPS. It has been well studied that doping graphene with N manipulates the electronic and physicochemical properties of pristine graphene with improved applicability.¹⁹ Thus, put together solid evidence of Ge nano-crystals immobilized on multilayer N-doped graphenic nano-sheets has been procured. It is apparent that in this method graphitization occurs at a

relatively lower temperature in solution phase without any additional requirement of catalyst or pre-polymerization, template and etching steps, tedious synthesis of precursors, vacuum systems etc. as involved in the conventional routes.²⁰ Under the hot-injection conditions, the precursors undergo a series of complex events. The precursor 2 plays the binary role of reducing Ge(II) and the generation of graphitic nanosheets through intermolecular cross-linking^{17,21} process. This gives rise to polyaromatic systems and ultimately into extended graphitic nano-sheets onto which the oleylamine capped Ge NCs are impregnated. The purification step is trivial involving no metal salt or catalyst removal. The volatile by-product Me₃SiCl escapes out from the medium, while any other plausible silylated products²² formed and excess oleylamine are removed during washing. Therefore, the Ge/NG isolated after precipitation and repeated washing is free from any impurities as characterized and confirmed from PXRD and XPS analyses. This is the first example where Ge nanocrystals and graphitic nanosheets have been grown simultaneously in the solution-phase from small molecules.

The transmission electron microscopy (TEM) image (Figure 2.12a) reveals that the Ge NCs are fairly uniformly and densely anchored²³ on the graphitic nano-sheets. The mean size of Ge NCs is around 5 nm which could be clearly observed from HRTEM (Figure 2.13b). The lattice fringes have interlayer spacing of 0.32 nm (Figure 2.9b), which agrees well with the (111) plane of diamond cubic Ge and matches with the interlayer spacing calculated from PXRD. The selected area electron diffraction (SAED) pattern also reveals that the Ge NCs have a diamond cubic structure. No diffraction patterns associated with the graphitic sheets indicates poor degree of graphitization.

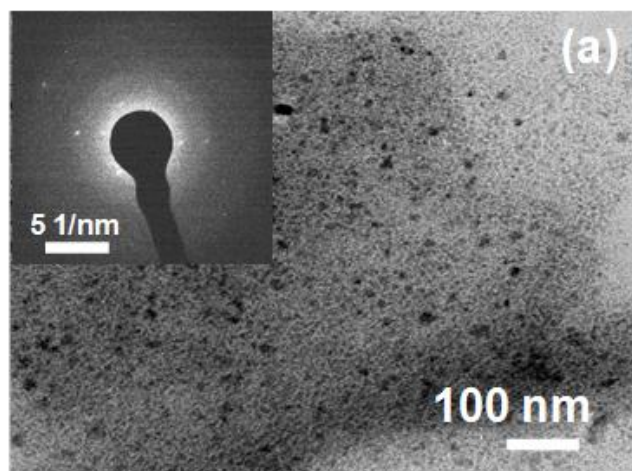


Figure 2.12 (a) TEM image of Ge/NG;

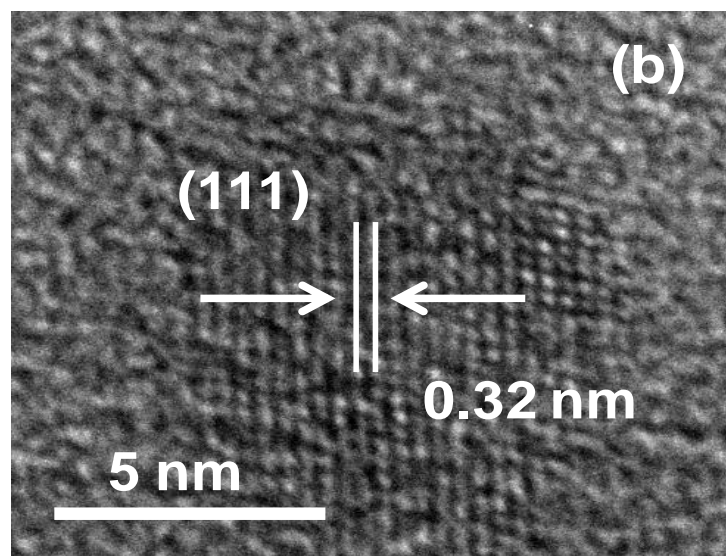


Figure 2.13 (b) HRTEM image of Ge/NG

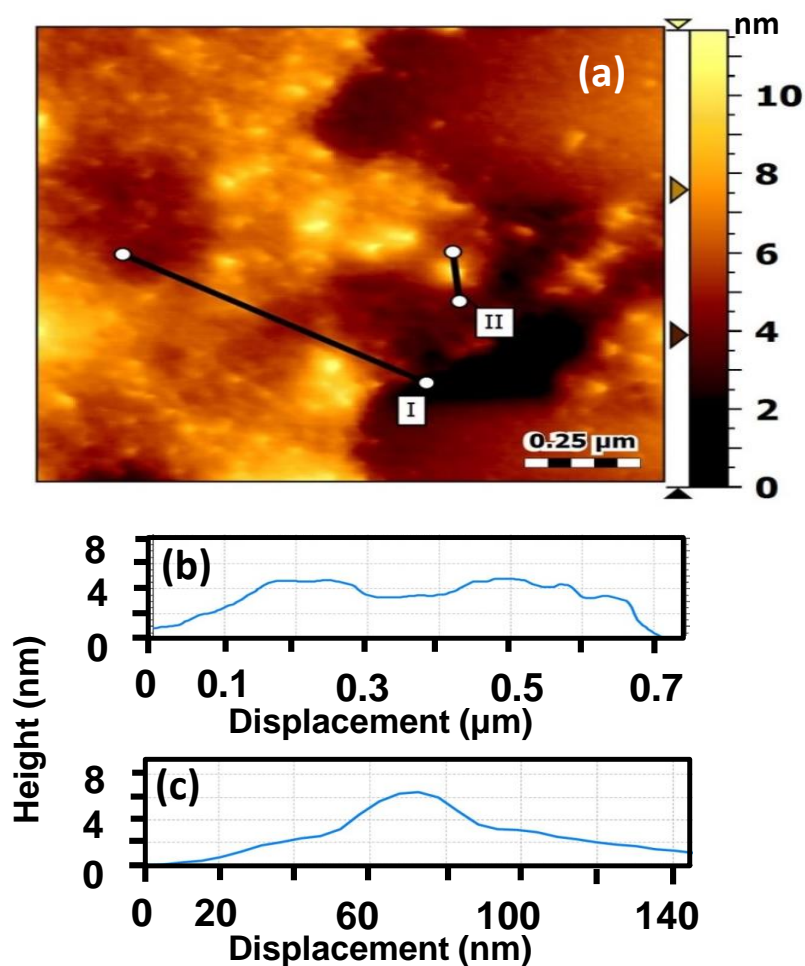


Figure 2.14 (a) AFM image; (b)–(c) height profiles for lines I and II in the AFM image of Ge nanocrystals.

The profile height in atomic force microscopy (AFM) study (Figures 2.14a-c) shows nanosheet thickness of around 4 nm, characteristic of approximately 10 stacked graphene layers. Ge/NG was subsequently annealed at 700 °C for 2 hours under Ar containing 5% H₂. The carbonization led to the formation of a carbon coated Ge/NG/C with 57 wt.% of Ge as confirmed from the thermogravimetric analysis²⁴ in air. The XRD pattern of Ge/NG/C shows intense and sharp peaks well-corresponding to the diamond cubic phase of Ge (Figure 2.9a). It is likely that the (002) diffraction peak for N doped graphitic sheets is eclipsed by the Ge(111) peak and hence not observed. The AD/AG ratio in the Raman spectra of Ge/NG/C (Figure 2.9b) decreases to 1.46 when compared with the value for Ge/NG, reflecting the structural restoration of graphitic framework in Ge/NG/C.^{23,25} The positional shift of the 2D band and a slight decrease in the A2D/AG ratio also echoes the graphitization.

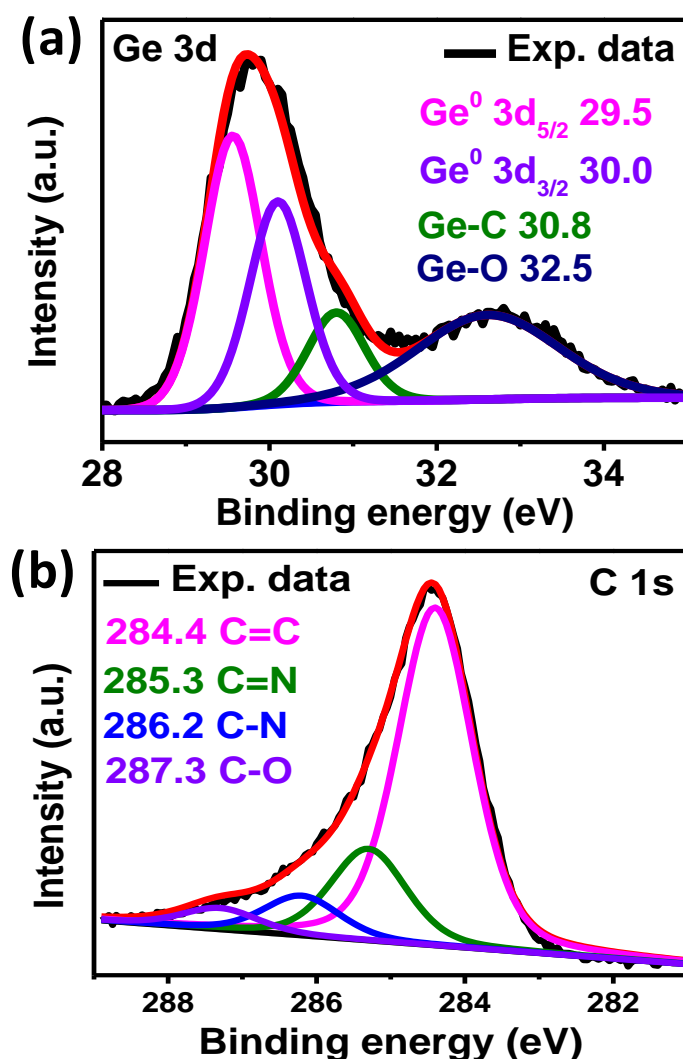


Figure 2.15 High resolution XPS analysis of (a) Ge 3d for Ge/NG/C, (b) C1s for Ge/NG/C

Chapter 2. Coherent Solution-phase Synthesis of a Germanium-Graphitic Nanocomposite and Its Evaluation for Lithium-Ion Battery Anodes: Non-innocent Role of the Mashima Reagent

The high resolution XPS spectra (Figure 2.15a) of Ge 3d^{24,26} for Ge/NG/C plainly shows the substantial decrease in Ge O groups after carbonization; other features (Figure 2.15b) of the survey spectra remaining similar as Ge/ NG. The level of surface oxidation of Ge NCs reduces substantially upon annealing. The N 1s peak was not very distinct probably due to their abundance only in the bulk.²³ The amount of N doping in Ge/NG/C is about 1.5 wt.%. The decrease in doping level arises due to high reaction temperature making most of the C N bonds vulnerable to bond cleavage.^{23, 28}

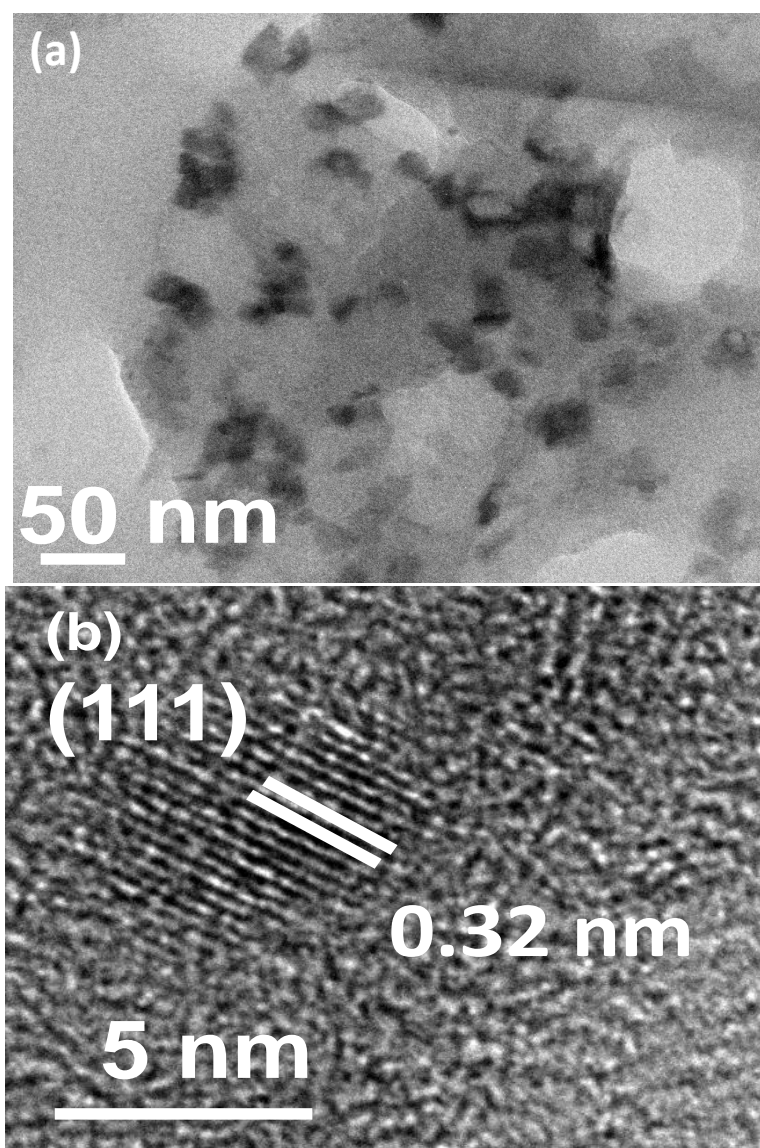


Figure 2.16 (a) TEM; (b) HRTEM;

The post-anneal TEM images are very informative. The major discernable change is the increase in NC size and their polycrystalline nature.²⁹ The Ge NCs with an increased average particle size of 26 nm could be clearly observed distributed on the transparent crack-free nanosheets (Figure 2.16a). No Ge NCs were found outside the nanosheets. No agglomeration was observed in the nanocomposite. Similar to the as-synthesized nanocomposite, Ge/NG/C shows highly crystalline Ge NCs with a (111) interplanar spacing of 0.32 nm (Figure 2.16b).

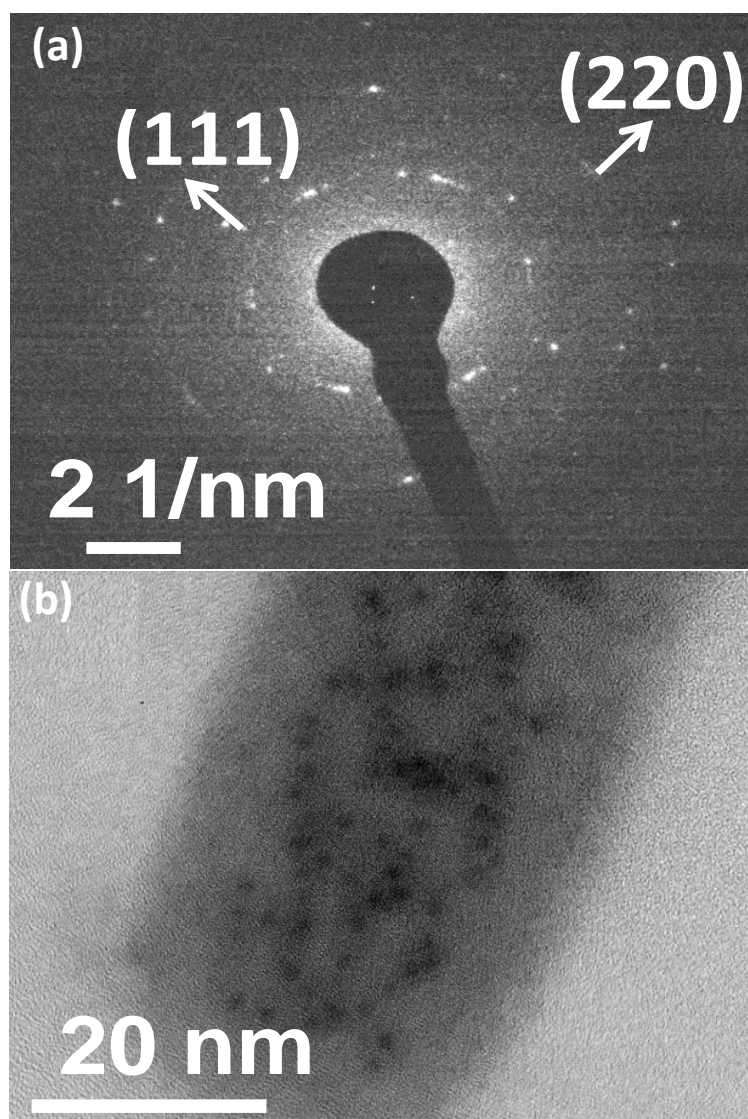


Figure 2.17 (a) SAED images of Ge/NG/C; (b) TEM image of the anode material taken after 100 cycles.

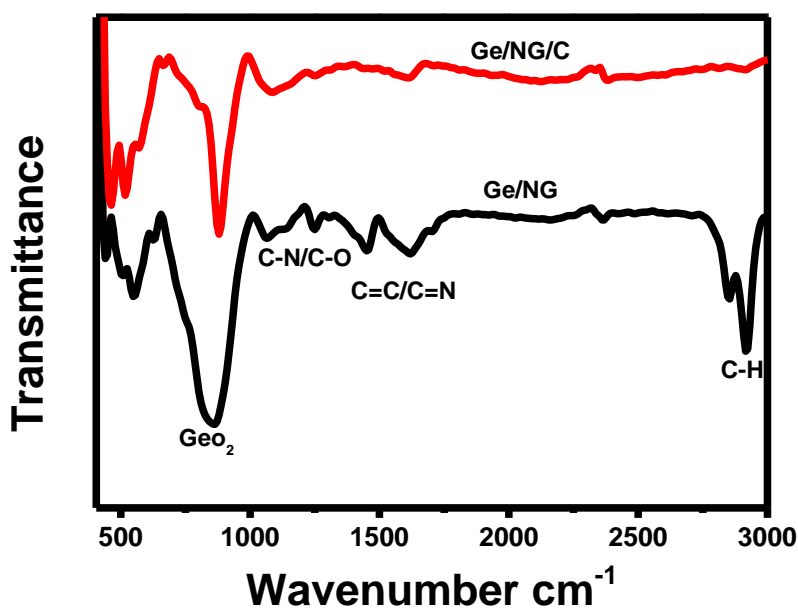


Figure 2.18 FTIR spectra of Ge/NG and Ge/NG/C

The diffraction rings in the SAED pattern (Figure 2.17a) was perfectly indexed to the crystal planes of cubic Ge phase in accordance with the PXRD data. The specific surface area of Ge/NG/C, as determined from BET analysis is $176 \text{ m}^2\text{g}^{-1}$ and the volume of mesopores is $0.241 \text{ cm}^3\text{g}^{-1}$ as calculated using BJH³⁸ method. The as synthesized Ge/NG capped with oleylamine which conforms with FTIR (Figure 2.18), after annealing the capped ligand removed in Ge/NG/C.

2.3.3 Electro chemical properties

The electrochemical performance of Ge/NG/C was thus evaluated with cyclic voltammetry (CV) (Figure 2.19a) and charge-discharge galvanostatic voltage profile (Figure 2.19b) in a CR2032 coin cell. The peak potentials in the cyclic voltammogram²³ and the observation of a distinct plateau at around 0.3 V in charge-discharge voltage profile³⁴ confirmed that the Li alloying/dealloying occurs with Ge nanocrystals. The initial discharge and charge specific capacities are 1447 and 1049 mAhg^{-1} respectively based on the total mass of the Ge/NG/C, corresponding to initial Coulombic efficiency of 72.5%. However, the capacity deteriorates in the subsequent cycles up to about 100th cycle (Figure 2.11a). This electrochemical instability arises due to the probable volume expansion of the larger sized ($>20 \text{ nm}$) Ge NC and the high surface area of graphene-like sheets where more solid electrolyte interface (SEI) are irreversibly formed.^{29,34} In addition, the SEI layer formed in this case continuously ruptures

Chapter 2. Coherent Solution-phase Synthesis of a Germanium-Graphitic Nanocomposite and Its Evaluation for Lithium-Ion Battery Anodes: Non-innocent Role of the Mashima Reagent and reforms thereby consuming Li^+ during the first 100 cycles. Worth mentioning, a SEI-free surface is advantageous in terms of obtaining high initial Coulombic efficiency and stable long-term cycling as has been reported in the case of ZnO porous nanocomposite with surface/interface organic encapsulation.³⁵ After 250 cycles, 88% of the discharge capacity at 100th cycle = 456 mAhg⁻¹ is retained (Figure 2.19a). On the basis of 57 wt.% of Ge NCs in the nano-composite, the calculated reversible capacity of Ge NCs was 705 mAhg⁻¹ at the 250th cycle.

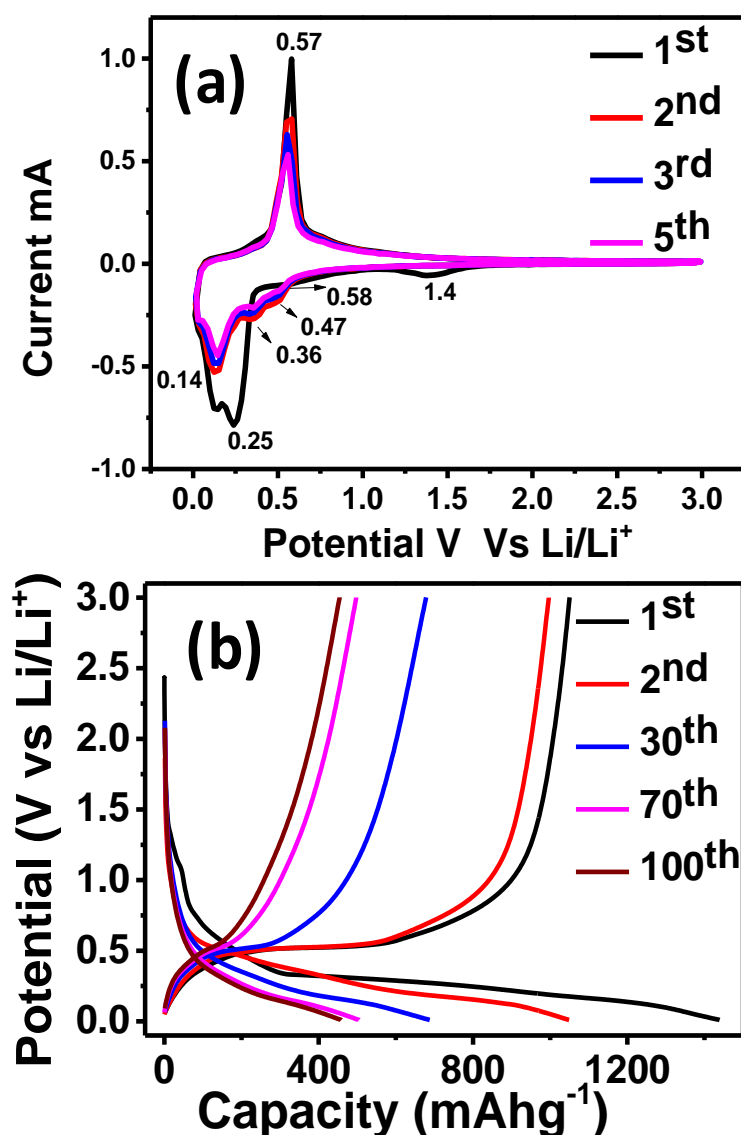


Figure 2.19 (a) Cyclic Voltammogram (scan rate = 0.1 mV/sec); (b) Discharge-charge Voltage profile of the electrode containing Ge/NG/C nanocomposite in the half-cell w.r.t. Li/Li^+

The TEM image (Figure 2.17b) of the electrode after running 100 cycles^{32d} at 500 mA_g⁻¹ show that the Ge NCs have transformed into fine NCs with an average size of 5 nm, similar to the size of the NCs before carbonization.²⁹ A stable battery data after 100th cycle has been obtained possibly due to these smaller sized Ge NCs with potentially alleviated volume change during Li insertion/de-insertion. To this point, we have investigated the anode performance of the smaller sized Ge/NG nanocomposites. It shows a declining specific capacity in the first 25 cycles collected, probably due to the oleylamine encapsulation around the Ge(0). This is on contrary to the recently reported case where the surface/interface organic encapsulation of manganese oxide has led to excellent battery performance through morphology reshaping.³⁶

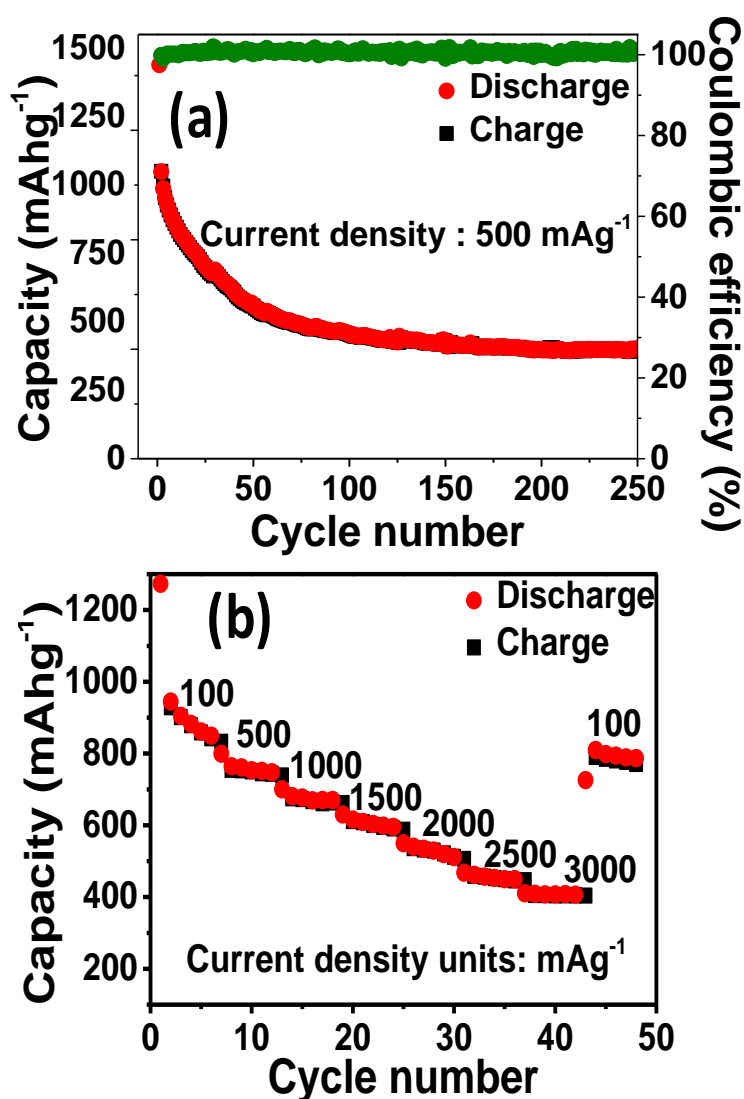


Figure 2.20 (a) Cyclic Cycling performance; (b) Rate Capability profile of the electrode containing Ge/NG/C nanocomposite in the half-cell w.r.t. Li/Li⁺.

The morphology reshaping has been realized from the N-methyl-2-pyrrolidone (NMP)-soluble organic functional groups which uniformly encapsulated the sub-3 nm nanocrystals. There are also other reported examples where the sub-3 nm monodisperse nanocrystals with organic modified surface/interfaces and abundant pores has led to ultra-steady cycling performance.³⁷ However, in our case the Ge/NG does not form any uniform colloidal dispersion in NMP.

The rate capability of Ge/NG/C was evaluated under a wide range of current densities (100 mA g⁻¹ to 3 Ag⁻¹) (Figure 2.20b). A capacity of 402 mAh g⁻¹ was obtained even at a high current density of 3 Ag⁻¹. The capacity was recovered to a value similar to the initial one when the current density was reverted back to 100 mA g⁻¹, demonstrating the stability and reversibility of the composite.¹³ The LIB application study done using Ge/NG/C is still inchoate. A smaller sized Ge NCs and crystalline graphenic sheets enriched with N-doping are necessary for a better anode performance which should be achievable targets through synthetic manipulations of our current methodology.

2.4 Summary

We have developed an easily implementable chemical strategy and large-scale coherent production of amalgamated Ge-graphitic nanocomposites. Essentially, the organosilicon compound has proven to be a promising precursor for making nanostructures with tunable composition and electronic properties. The preparation of novel nanocomposites using this modular synthetic approach suitable for applications in energy and storage devices is currently underway in our laboratory.

References:

1. a) S. Yao, Y. Xiong, M. Driess, *Acc. Chem. Res.* 2017, 50, 2026–2037; b) Y. Wang, M. Karni, S. Yao, Y. Apeloig, M. Driess, *J. Am. Chem. Soc.* **2019**, 141, 1655–1664.
2. J. Seo, A. C. Cabelof, C.-H. Chen, K. G. Caulton, *Chem. Sci.* **2019**, 10, 475–479.
3. a) W. Kaim, *Angew. Chem.* 1981, 93, 621–622; *Angew. Chem. Int. Ed.* **1981**, 20, 600–601; b) H. D. Hausen, O. Mundt, W. Kaim, *J. Organomet. Chem.* **1985**, 296, 321–337.
4. T. Saito, H. Nishiyama, H. Tanahashi, K. Kawakita, H. Tsurugi, K. Mashima, *J. Am. Chem. Soc.* **2014**, 136, 5161–5170.

5. P. K. Majhi, H. Ikeda, T. Sasamori, H. Tsurugi, K. Mashima, N. Tokitoh, *Organometallics* **2017**, *36*, 1224–1226.
6. R. K. Raut, S. F. Amin, P. Sahoo, V. Kumar, M. Majumdar, *Inorganics* **2018**, *6*, 69.
7. M. Majumdar, R. K. Raut, P. Sahoo, V. Kumar, *Chem. Commun.* **2018**, *54*, 10839–10842.
8. T. Yurino, Y. Ueda, Y. Shimizu, S. Tanaka, H. Nishiyama, H. Tsurugi, K. Sato, K. Mashima, *Angew. Chem. Int. Ed.* **2015**, *54*, 14437–14441; *Angew. Chem.* **2015**, *127*, 14645–14649.
9. a) J. Michel, J. Liu, L. C. Kimerling, *Nat. Photonics*, **2010**, *4*, 527–534; b) J. Y. Fan, P. K. Chu, *Small*, **2010**, *6*, 2080–2098; c) S. Wu, C. Han, J. Iocozzia, M. Lu, R. Ge, R. Xu, Z. Lin, *Angew. Chem. Int. Ed.* **2016**, *55*, 7898–7922; *Angew. Chem.* **2016**, *128*, 8028–8054.
10. D. D. Vaughn II, R. E. Schaak, *Chem. Soc. Rev.* **2013**, *42*, 2861–2879.
11. E. Muthuswamy, A. S. Iskandar, M. M. Amador, S. M. Kauzlarich, *Chem. Mater.* **2013**, *25*, 1416–1422.
12. a) C. de Mello Donegá, P. Liljeroth, D. Vanmaekelbergh, *Small* **2005**, *1*, 1152–1162; b) D. A. Ruddy, J. C. Johnson, E. R. Smith, N. R. Neale, *ACS Nano*, **2010**, *4*, 7459–7466.
13. D.-J. Xue, S. Xin, Y. Yan, K.-C. Jiang, Y.-X. Yin, Y.-G. Guo, L.-J. Wan, *J. Am. Chem. Soc.* **2012**, *134*, 2512–2515.
14. W. Gao, H. Huang, H. Shi, X. Feng, W. Song, *Nanotechnology* **2014**, *25*, 415402.
15. J. Chen, Z. Mao, L. Zhang, Y. Tang, D. Wang, L. Bie, B. D. Fahlman, *Carbon*, **2018**, *130*, 41–47.
16. B. Wang, J. Jin, X. Hong, S. Gu, J. Guo, Z. Wen, *J. Mater. Chem. A*, **2017**, *5*, 13430–13438.
17. S. Zhang, K. Dokko, M. Watanabe, *Chem. Mater.* **2014**, *26*, 2915–2926.
18. Y. Wang, Y. Shao, D. W. Matson, J. Li, Y. Lin, *ACS Nano*, **2010**, *4*, 179
19. H. Wang, T. Maiyalagan, X. Wang, *ACS Catal.* **2012**, *2*, 781–794.
20. a) L. Zhi, K. Müllen, *J. Mater. Chem.* **2008**, *18*, 1472–1484; b) A. Narita, X. Feng, Y. Hernandez, S. A. Jensen, M. Bonn, H. Yang, I. A. Verzhbitskiy, C. Casiraghi, M. R. Hansen, A. H. R. Koch, G. Fytas, O. Ivasenko, B. Li, K. S. Mali, T. Balandina, S. Mahesh, S. De Feyter, K. Müllen, *Nat. Chem.* **2013**, *6*, 126–132; c) L. Talirz, P.

- Ruffieux, R. Fasel, *Adv. Mater.* **2016**, 28, 6222–6231; d) Y. Segawa, H. Ito, K. Itami, *Nat. Rev. Mater.* **2016**, 1, 15002.
21. A. Turchanin, A. Beyer, C. T. Nottbohm, X. Zhang, R. Stosch, A. Sologubenko, J. Mayer, P. Hinze, T. Weimann, A. Götzhäuser, *Adv. Mater.* **2009**, 21, 1233–1237.
22. M. A. Meshgi, S. Biswas, D. McNulty, C. O'Dwyer, G. A. Alessio Verni, J. O'Connell, F. Davitt, I. Letofsky-Papst, P. Poelt, J. D. Holmes, C. Marschner, *Chem. Mater.* **2017**, 29, 4351–4360.
23. Y. Xiao, M. Cao, *ACS Appl. Mater. Interfaces*, **2014**, 6, 12922–12930.
24. Y. Xu, X. Zhu, X. Zhou, X. Liu, Y. Liu, Z. Dai, J. Bao, *J. Phys. Chem. C*, **2014**, 118, 28502–28508.
25. D. W. Chang, E. K. Lee, E. Y. Park, H. Yu, H.-J. Choi, I.-Y. Jeon, G.-J. Sohn, D. Shin, N. Park, J. H. Oh, L. Dai, J.-B. Baek, *J. Am. Chem. Soc.* **2013**, 135, 8981–8988.
26. V. C. Holmberg, B. A. Korgel, *Chem. Mater.* **2010**, 22, 3698–3703.
27. a) K. H. Seng, M.-H. Park, Z. P. Guo, H. K. Liu, J. Cho, *Angew. Chem. Int. Ed.* **2012**, 51, 5657–5661; b) J. Alvarado-Rivera, D. A. Rodriguez-Carvajal, M. C. Acosta-Enriquez, M. B. Manzanares-Martinez, E. Alvarez, R. Lozada Morales, G. C. Diaz, A. Leon, M. E. Zayas, *J. Am. Ceram. Soc.* **2014**, 97, 3494–3500.
28. Z. Xing, Z. Ju, Y. Zhao, J. Wan, Y. Zhu, Y. Qiang, Y. Qian, *Sci. Rep.* **2016**, 6, 26146.
29. F.-W. Yuan, H.-Y. Tuan, *Chem. Mater.* **2014**, 26, 2172–2179.
30. S. Pei, H.-M. Cheng, *Carbon*, 2012, 50, 3210–3228.
31. C. Wang, J. Ju, Y. Yang, Y. Tang, J. Lin, Z. Shi, R. P. S. Han, F. Huang, *J. Mater. Chem. A*, **2013**, 1, 8897–8902.
32. [33] a) R. Mo, D. Rooney, K. Sun, H. Y. Yang, *Nat. Commun.* **2017**, 8, 13949; b) H. Kim, Y. Son, C. Park, J. Cho, H. C. Choi, *Angew. Chem. Int. Ed.* **2013**, 52, 5997–6001; c) S. Fang, L. Shen, H. Zheng, X. Zhang, *J. Mater. Chem. A*, **2015**, 3, 1498–1503; d) J.-G. Ren, Q.-H. Wu, H. Tang, G. Hong, W. Zhang, S.-T. Lee, *J. Mater. Chem. A* **2013**, 1, 1821–1826; e) S. Jin, N. Li, H. Cui, C. Wang, *ACS Appl. Mater. Interfaces* **2014**, 6, 19397–19404; f) H. Song, N. Li, H. Cui, C. Wang, *Nano Energy* **2014**, 4, 81–87.
33. X. Li, J. Liang, Z. Hou, Y. Zhu, Y. Wang, Y. Qian, *Chem. Commun.* **2015**, 51, 3882–3885.
34. G. Cui, L. Gu, L. Zhi, N. Kaskhedikar, P. A. van Aken, K. Müllen, J. Maier, *Adv. Mater.* **2008**, 20, 3079–3083.

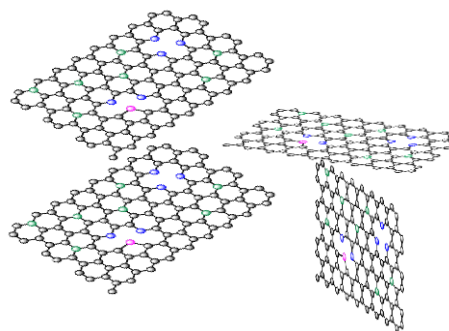
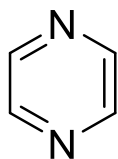
Chapter 2. Coherent Solution-phase Synthesis of a Germanium-Graphitic Nanocomposite and Its Evaluation for Lithium-Ion Battery Anodes: Non-innocent Role of the Mashima Reagent

35. H. Song, J. Su, C. Wang, *Adv. Energy Mater.* **2019**, *9*, 1900426.
36. J. Su, H. Song, C. Wang, *Adv. Funct. Mater.* **2019**, *29*, 1907154.
37. H. Song, J. Su, C. Wang, *ACS Appl. Mater. Interfaces* **2019**, *11*, 37867– 37874.
38. Thommes, M.; Kaneko, K.; Neimark, A. V.; Olivier, J. P.; Rodriguez-Reinoso, F.; Rouquerol, J.; Sing, K. S. W. *Pure Appl. Chem.* **2015**, *87*, 1051–1069.

Chapter 3

Synthesis and Characterisation of N-rich Carbon Nanosheets and their Application as Anode Material in Li-ion Battery

Pyrazine



Enthalpy of sublimation 56.2 kJ/mol

Temperature 303 °C

Boiling point 115 °C

3.1 Introduction

The doping of a heteroatom into a carbon framework to control the different properties of materials has emerged as a major research area.^{1, 2} N,⁴ S,⁶ B,³ and P⁵ are some of the atoms used for doping. Among these heteroatoms, it is easiest to dope N to adjust the relationship between the structural properties and electrical properties of the material, while maintaining the intrinsic properties of the carbon network.^{4a, 7} Nitrogen doping leads to the formation of n-type semiconducting materials, which are similar to typical semiconducting materials. This indicates that the different C-N bonding networks can be utilised in several electrical applications. Nitrogen is adjacent to carbon on the periodic table and its introduction into the graphitic network can modify the number of electrons depending on the amount of the carbon replaced with nitrogen. Consequently, there are no major lattice mismatches with carbon because the atomic radius of nitrogen is approximately similar to that carbon. Therefore, N-doped graphitic materials have received considerable attention for technical and scientific applications.^{9, 10} There are two ways to synthesise N-doped grapheme, i.e., post treatment using N₂ plasma treatment,¹² arc-discharge methods, or¹³ thermal annealing in ammonia; and direct synthesis using chemical vapour deposition,¹⁶ solvothermal, or¹⁴ segregation growth approach methods. However, post treatment methods have low efficiency, while direct methods use toxic organic starting materials.¹⁷ In addition, control over compositional homogeneity and morphology is difficult to achieve using the above methods.¹⁸

Therefore, it is important to develop an easy and environmentally friendly procedure to synthesis effective N-doped carbon nanosheets.¹⁸

The Mashima reagent has been used to synthesis low-valent transition and main-group metal complexes. Our group has reported the one-pot synthesis of N-heterocyclic germylene and

stannylene using 1,4-bis-(trimethylsilyl)-1,4-diaza-2,5-cyclohexadiene as the reductant.¹⁹ Metal(0) nanoparticles have been produced using this salt-free reduction method from both transition metal chlorides and main-group chlorides (Ga, In, Sb, Ge, and Bi).^{20, 21} Here, we report for the first time the room-temperature synthesis of N-rich carbon nanosheets using this organosilicon reducing agent. The reducing agent reacted with O₂ at room temperature to yield nitrogen-rich carbon nanosheets. These carbon nanosheets contained 22.7% nitrogen, which is the highest reported in literature to the best of our knowledge. These carbon nanosheets were annealed at 700 °C and 500 °C for 4 h in an inert environment and then both materials were characterised. Then, the materials were used as anode materials in Li ion battery.

3.2 Experimental Sections

3.2.1 General Remarks.

Synthesis: All the chemicals were purchased from Sigma-Aldrich and used as is. Tetrahydrofuran and pentane were refluxed over sodium/benzophenone and distilled prior to use, while acetone and toluene were simply distilled prior to use. 1,4-Bis-(trimethylsilyl)-1,4-diaza-2,5-cyclohexadiene was prepared according a procedure obtained from literature.[S1] The annealing was carried out in a Nabertherm RHTC 80-710/15.

3.2.2 Synthesis of the CRT (Carbon at room temperature) : 1,4-Bis(trimethylsilyl)-1,4-diaza-2,5-cyclohexadiene (2 g, 8.8 mmol) dissolved in pentane was poured in a petri dish and kept in open air at ambient temperature. The yellow solution immediately changed to brown, while the temperature of the solution increased to 80 °C. The reaction mixture was slowly concentrated and produced a brown powder after 2 h.

3.2.3 Synthesis of the C500: The CRT (400 mg) was annealed for 4 h under argon in a furnace to yield a black powder, C500 (160 mg). The heating rate was 2 °C/min.

3.2.4 Synthesis of the C700: The CRT (400 mg) was annealed for 4 h under argon in a furnace to yield a black powder, C700 (120 mg). The heating rate was 2 °C/min.

3.2.5 Characterisation: The powder X-ray Diffraction (PXRD) of the material were recorded using a Bruker D8 Advance X-ray diffractometer equipped with Cu K α radiation (1.54 Å). Meanwhile, the Raman spectra of the nanosheets were analysed using LabRAM HR800 from Yvon Horiba. The X-ray photoelectron spectroscopy (XPS) data were collected

using PHI 5000 Versa Probe II, FEI Inc, while scanning electron microscopy (SEM) was done using FEI Nova Nano 450 SEM. The Brunauer-Emmett-Teller (BET) adsorption measurements for calculating the surface area were carried out using a Quadrasorb automatic volumetric instrument. The atomic force microscopy (AFM) data were collected by a Keysight atomic force microscope (model: AFM 5500) using the tapping mode technique. The transmission electron microscopy (TEM) images were taken using a JEOL JEM 2100 FS field-emission transmission electron microscope at 200 kV. The CHN analyses were performed using an Elementar vario EL analyser.

3.2.6 Electrochemical Measurements: The electrodes were prepared from a slurry of C500, C700, conducting carbon, and polyvinylidene fluoride (PVDF) binder mixed at a weight ratio of 80:10:10 using an N-methyl-2-pyrrolidone (NMP) solvent. The slurry was coated onto a Cu foil and allowed to dry overnight at 80 °C. Then, the foil was punched into 1-cm² circular discs. The CR-2032 coin half-cell was assembled using this composite as the working electrode and metallic lithium foils as the counter and reference electrode. The mass of the active material loaded onto the electrode was 1.0 mg. A Whatmann was used as the separator, while a commercial electrolyte of 1 M LiPF₆ in a 1:1 (v/v) mixture of ethylene carbonate (EC) and dimethyl carbonate (DMC) was used. All the cells were assembled inside an argon-filled glove box. The galvanostatic charge and discharge measurements were performed using a BTS-Neware (China) 5 V, 10 mA battery tester. The impedance and cyclic voltammetry were analysed using a VMP3 Biologic system equipped with potentiostat and galvanostat channels.

3.3 Results and Discussion

3.3.1 Preparation of the CRT

An 8.8 mmol of 1,4-bis(trimethylsilyl)-1,4-diaza-2,5-cyclohexadiene dissolved in pentane in a Schlenk round-bottomed flask in inert atmosphere gave yellow colour solution, was added to petri dish under ambient conditions. The yellow solution slowly turned brown. After 2 h, a dark brown solid was collected and characterised (Figure 3.1)

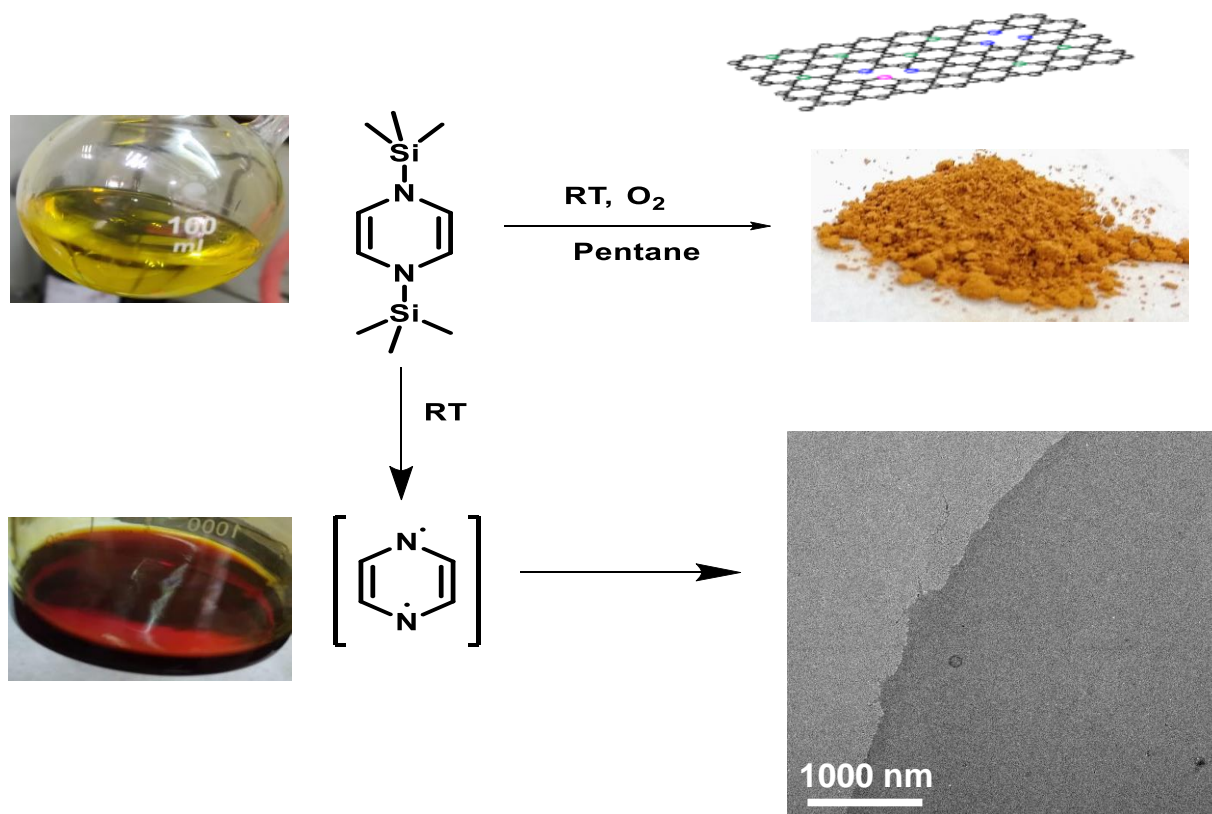


Figure 3.1: Schematic of the synthesis of the CRT.

3.3.2 Structural and Microscopic Analysis of CRT

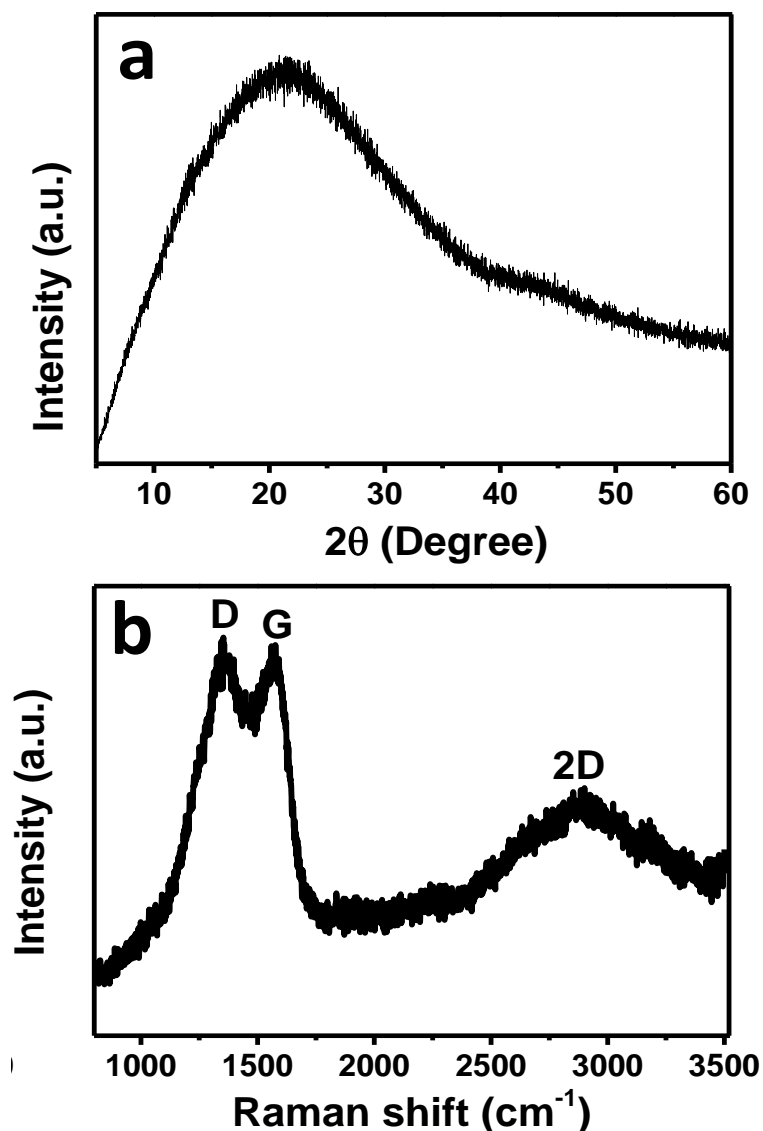


Figure 3.2 (a) PXRD pattern and (b) Raman spectra of the CRT.

The powder X-ray diffraction (PXRD) pattern (Figure 3.2a) of the CRT displays a broad peak which indicates the amorphous carbon nanosheets. The Raman spectroscopy (Figure 2.2b) shows three characteristic peaks at 1355, 1573, and 2880 cm^{-1} which are in good agreement with the typical optical modes of the D band (disorder induced phonon mode) and G band (graphitic band), respectively. The integrated area ratio of the D and G bands was 1.78, indicating that the graphitised structure had defects and disorders.²² A distinct broad 2D peak, which is the second-order D band, appeared at 2680 cm^{-1} in the Raman spectrum.

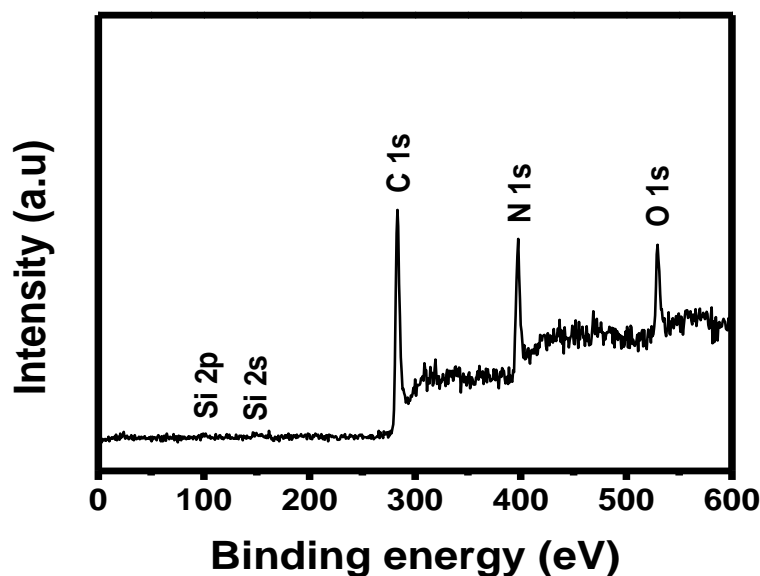


Figure 3.3 (a) Survey spectrum of the CRT; High resolution XPS of the (b) C1s; (c) N1s sp of the CRT.

The survey XPS scan shows four signals, which can be assigned to the elements C, N, Si, and O (Figure 3.3). The fitted XPS spectra of the C1s display three peaks (Figure 3.4a). The main peak at 284.3 eV was assigned to the graphite-like sp^2 C,²³ while, the other two peaks centred at 284.9 and 285.9 eV corresponded to the C=N and C N groups, respectively.²³ The N1s spectra could be de-convoluted into four sub peaks at 397.9, 400.3, 402.1, and 403.2 eV corresponding to the pyridinic N, pyrrolic N, quaternary N, and N-oxides, respectively (Figure 3.4b).²⁴ The N contents of the CRT obtained from the CHN elemental analysis and XPS was ~22 wt.%. The doping of graphene with N manipulates the electronic and physicochemical properties of pristine graphene, which improves the applicability of graphene.²⁵ Here, the carbon nanosheets were synthesised at a lower temperature in solution phase without any catalyst or pre-polymerization. To our knowledge, this is the first example in which nitrogen-rich carbon nanosheets have been synthesised in the solution phase from small molecules at room temperature.

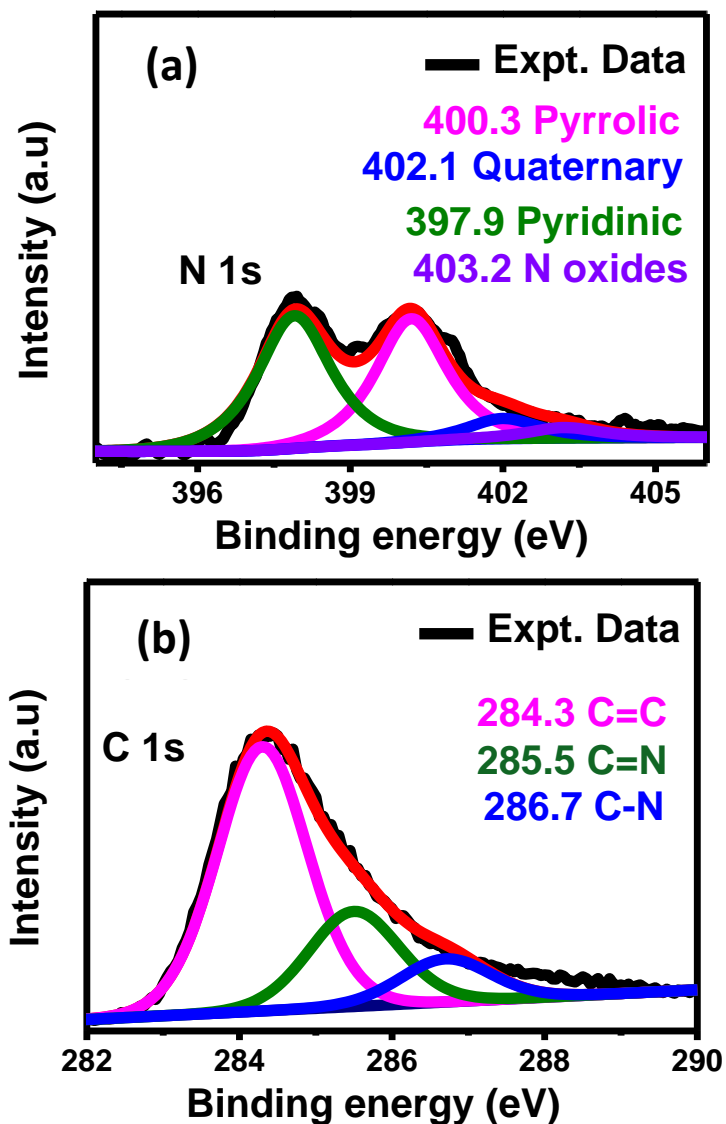


Figure 3.4 High-resolution XPS of the (a) C1s; (b) N1s sp of the CRT.

The field-emission scanning electron microscopy (FESEM) image of the CRT shows the sheet-like structure of the samples (Figure 3.5a). The energy-dispersive X-ray spectrum (EDS) mappings agreed well with the CHNS analysis on the percentages of the C and N elements. The TEM image of the CRT also shows a sheet-like shape, thereby supporting the FESEM observation (Figure 3.5b).

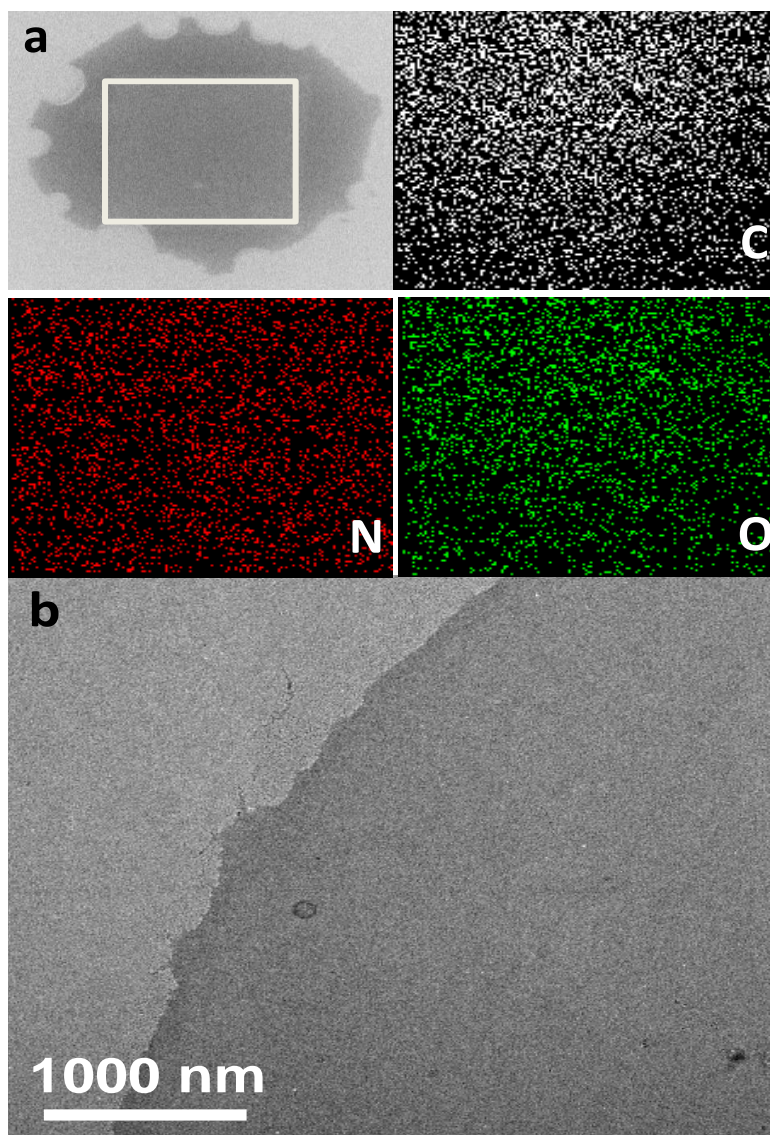


Figure 3.5 (a) FESEM elemental mapping; (b) HRTEM image.

3.3.3 CRT formation mechanism

In general, when trityl chloride reacts with silver metal it yields the trityl radical, which at room temperature is at equilibrium with its dimer. However, at low temperature, the trityl radical is the most dominant, while at high temperature its dimer becomes more dominant. Here, (Figure 3.6) 1,4-bis- (trimethylsilyl)-1,4-diaza-2,5-cyclohexadiene was used as the reducing agent to react with trityl chloride instead of the silver metal to produce trityl radical.

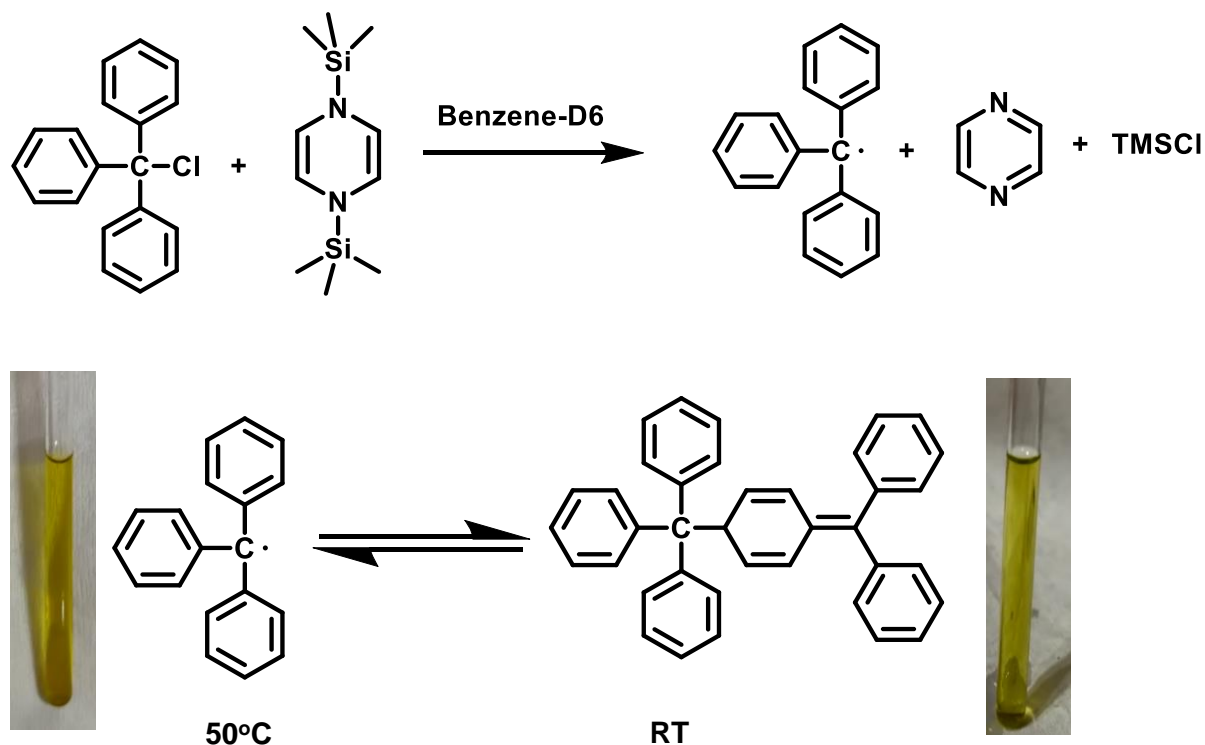


Figure 3.6 Reaction of the 1,4-bis- (trimethylsilyl)-1,4-diaza-2,5-cyclohexadiene reducing agent with trityl chloride.

The trityl radical was detected by variable-temperature ^1H NMR. At low temperatures, the ^1H NMR peak intensity decreases; however, at high temperatures, the intensity of the peak increased to 7.3δ (Figure 3.7). From these observations, it can be concluded that the formation of carbon nanosheets follows the radical-mediated path way, further explorations are required to be done for a concrete understanding.

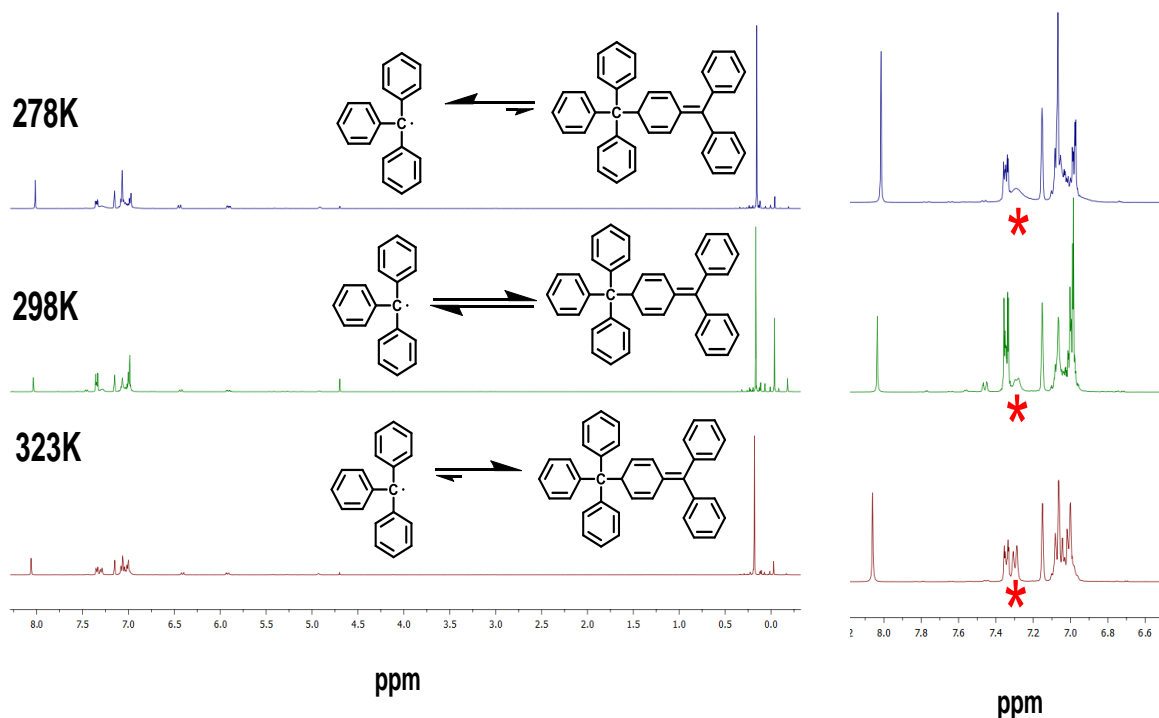


Figure 3.7 Variable-temperature ^1H NMR spectra of 1,4-bis-(trimethylsilyl)-1,4-diaza-2,5-cyclohexadiene reacted with trityl chloride.

3.3.4 Characterisation and properties of the C700 and C500

The CRT annealed at 500 and 700 °C under inert conditions for 4 h, viz. C500 and C700, respectively, were characterised using PXRD, Raman, XPS, BET, and HREM analyses. The PXRD patterns (Figure 3.8a) of C500 and C700 show a broad peak, indicating the presence of amorphous carbon nanosheets. Raman spectroscopy (Figure 3.8b) revealed that the graphitisation of C500 and C700 improved, as shown by the three characteristic peaks at 1351, 1571, and 2830 cm^{-1} , which were in good agreement with the typical optical modes of the D band (disorder-induced phonon mode) and G band (graphitic band). The integrated area ratio of the D and G bands was 1.67, indicating that the graphitised structure had defects and disorders.²² The broad 2D peak, which is the second-order D band, appeared at 2830 cm^{-1} in the Raman spectrum.

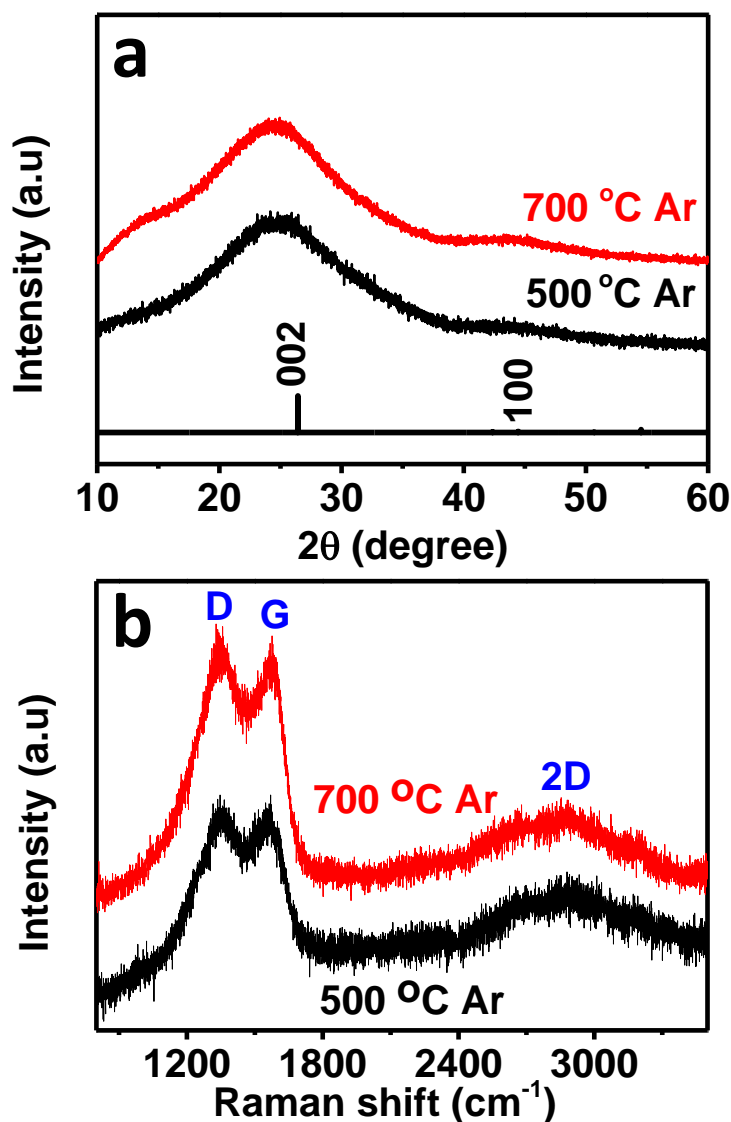


Figure 3.8 (a) PXRD pattern and (b) Raman spectra of the C500 and C700.

The survey XPS scan shows four signals which can be assigned to the elements C, N, Si, and O (Figure 3.9). The fitted XPS spectra of the C1s has three peaks (Figure 3.10a). The main peak at 284.3 eV was assigned to the graphite-like sp² C,²³ while the other two peaks centred at 285.2 and 286.3 eV corresponded to the C=N and C-N groups respectively.²³ The N1s spectra de-convoluted into three peaks at 398.5, 399.9, and 401.5 eV corresponding to the pyridinic N, pyrrolic N, and quaternary N, respectively (Figure 3.10b).²⁴ The N contents of the C500 determined by CHN elemental analysis and XPS was approximately 20.1 wt.%.

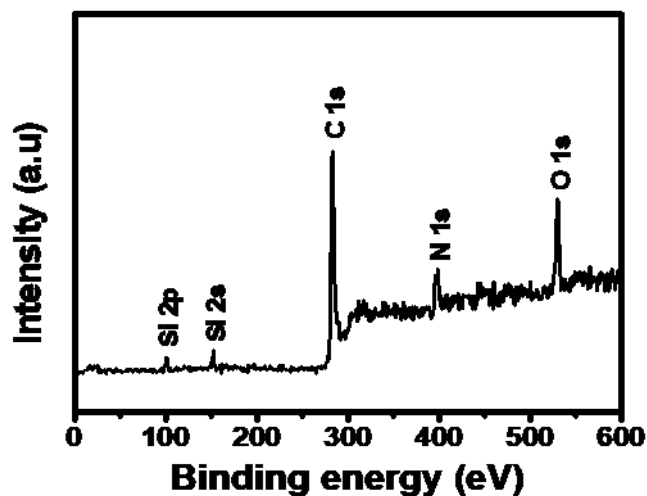


Figure 3.9 (a) Survey spectrum; High resolution XPS of the (b) C1s; (c) N1s sp of the C500

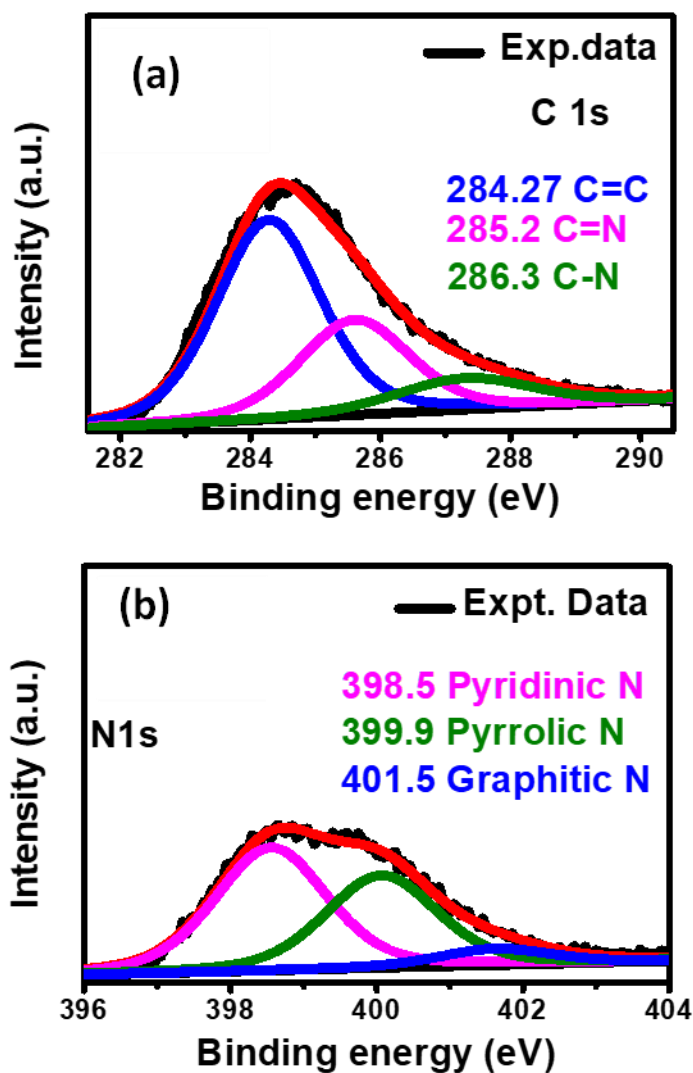


Figure 3.10 High resolution XPS of the (a) C1s; (b) N1s sp of the C500

The specific surface area of C500, determined by BET analysis using the BJH method, was $23 \text{ m}^2\text{g}^{-1}$ (Figure 3.9a). The HRTEM image shows that C500 had a sheet-like structure (Figure 3.11).

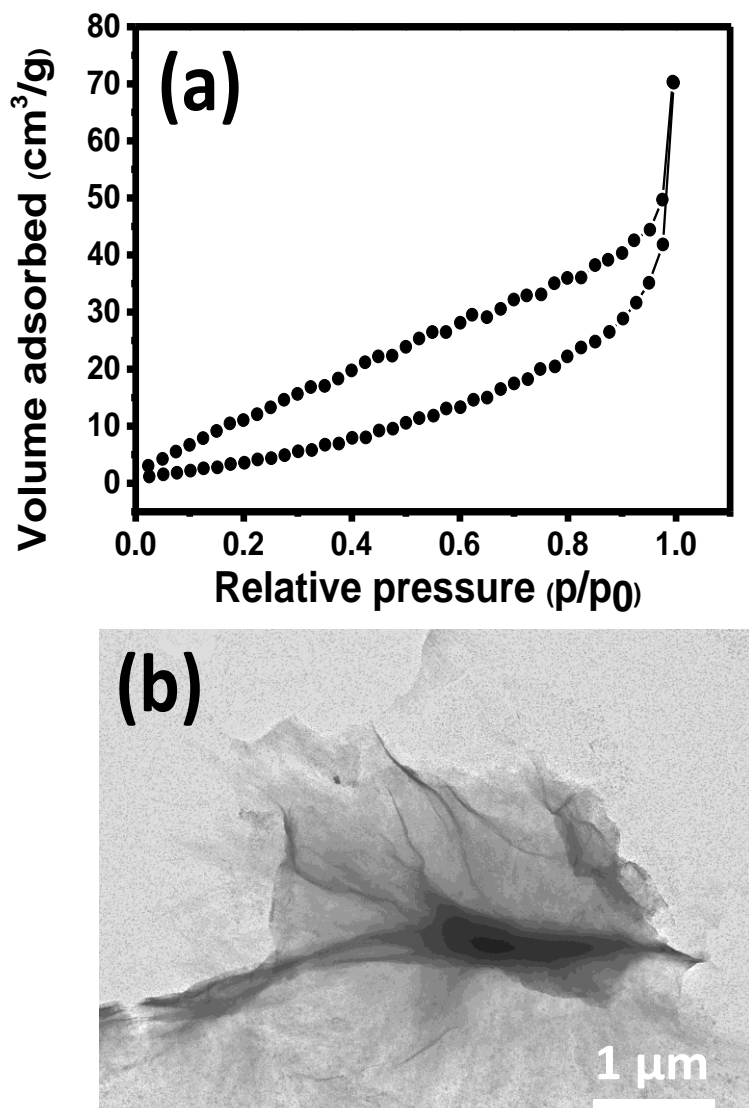


Figure 3.11 (a) BET isotherm; (b) HRTEM image of C500.

The survey XPS scan shows four signals, which can be assigned to the elements C, N, Si, and O (Figure 3.12). Meanwhile, the fitted XPS spectra of the C1s shows three peaks (Figure 3.13a) The main peak at 284.1 eV was assigned to the graphite-like sp² C,²³ while the other

two peaks, centred at 285.4 and 286.8 eV, corresponded to the C=N and C-N groups, respectively.²³

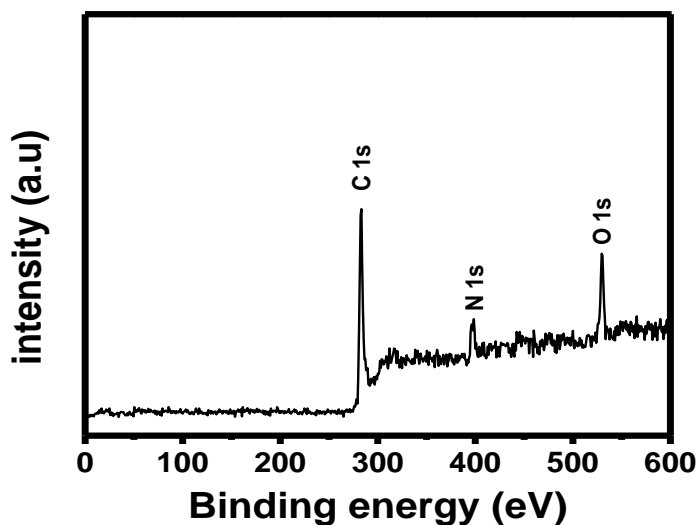


Figure 3.12 Survey spectrum;

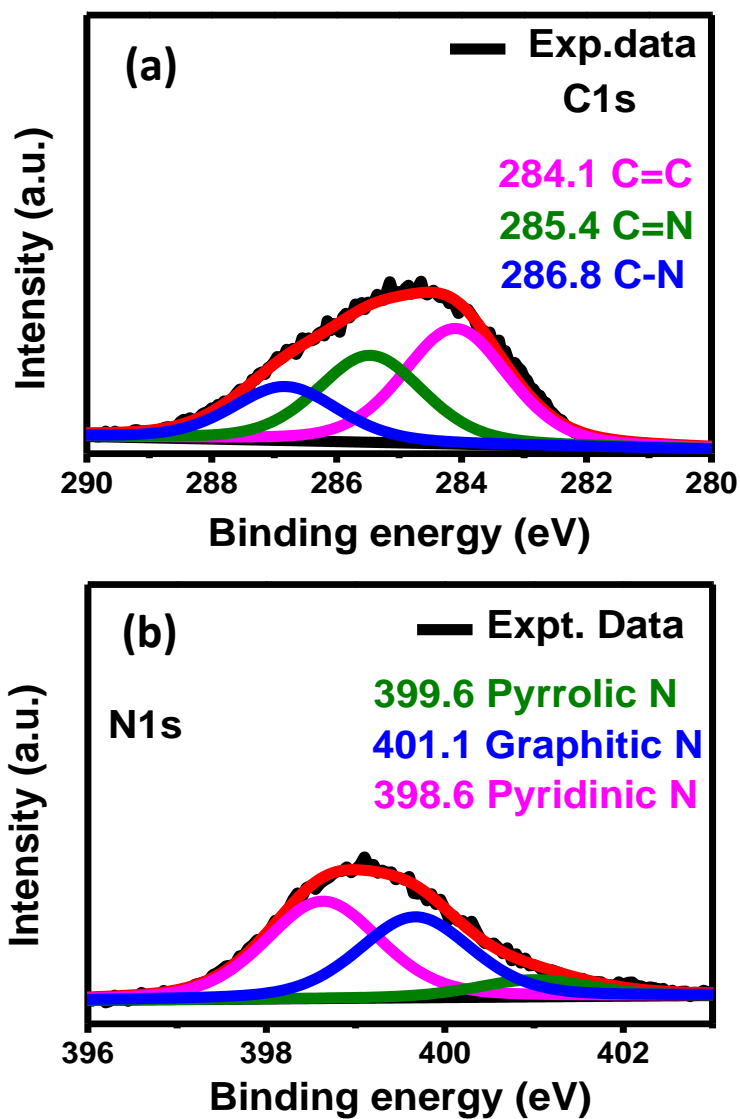


Figure 3.13 High-resolution XPS of the (a) C1s; (b) N1s sp of the C700

The N1s spectra was de-convoluted into three peaks at 398.6, 399.6, and 401.1 eV, corresponding to the pyridinic N, pyrrolic N, and graphitic N, respectively (Figure 3.13b).²⁴ The N contents of C700, determined by the CHN elemental analysis and XPS, was ~14.1 wt.%.

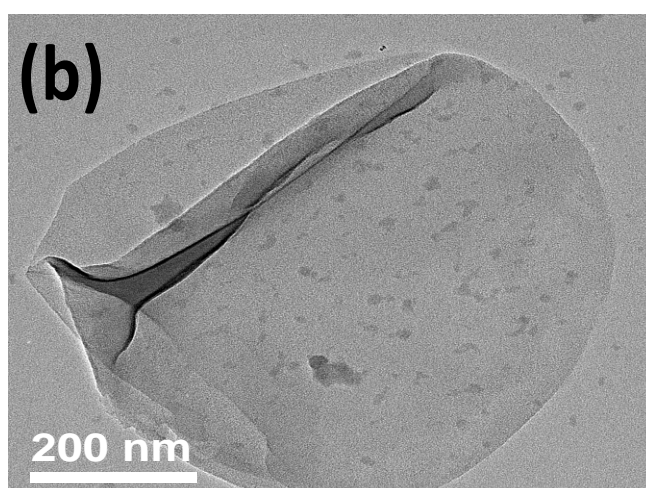
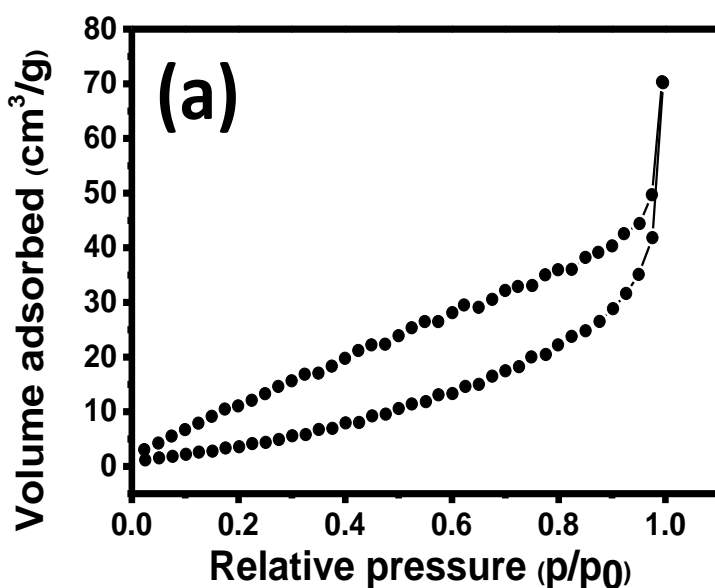


Figure 3.14 (a) BET isotherm; (b) HRTEM image of the C700.

The specific surface area of C700, as determined by the BET analysis, was $20 \text{ m}^2 \text{ g}^{-1}$ (Figure 3.14a). The HRTEM image of C700 shows that it had a sheet like structure (Figure 3.14b).

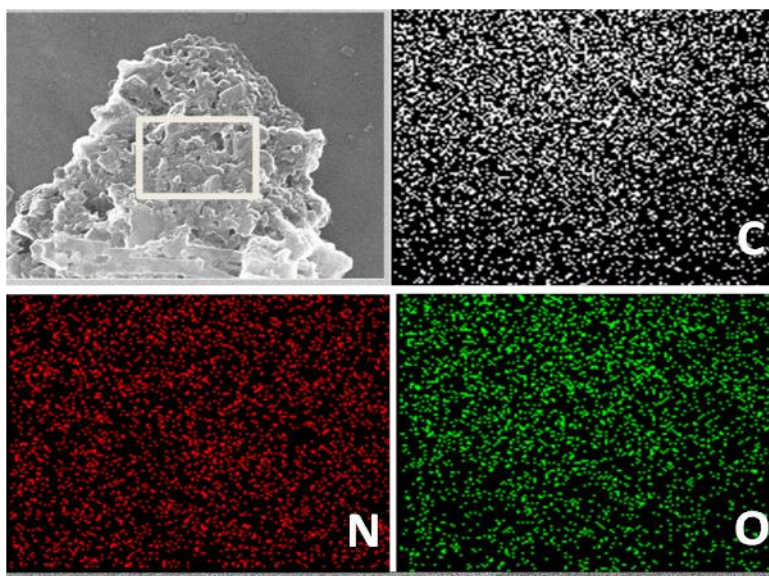


Figure 3.15 FESEM elemental mapping of the C500

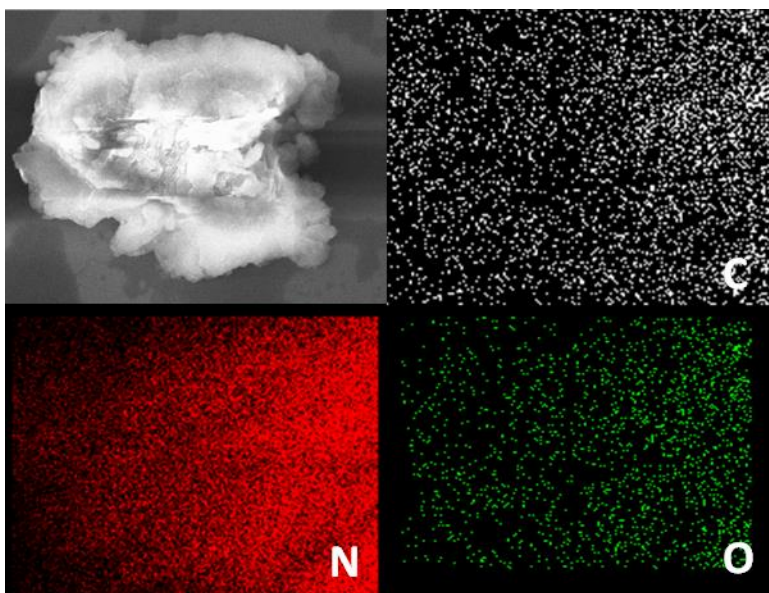


Figure 3.16 FESEM elemental mapping of the C700

The FESEM images of both C500 and C700 show that they had sheet-like structures. The elemental mapping of both materials also showed the presence of C, N, and O (Figure 3.15, 3.16).

Carbon nanosheets	CHNS	XPS	FESEM
CRT(Carbon at room temp)	N (22.2%) C (45.84%)	N (19.8%) C (53.72%)	N (38.22%) C (43.18%)
C500	N (20.1%) C (56.36%)	N (18.4%) C (53.74%)	N (25.2%) C (46.28%)
C700	N (14.1%) C (65.36%)	N (11.4%) C (63.34%)	N (14.72%) C (59.54%)

3.3.3 Electrochemical properties

3.3.3.1 Electrochemical performance of the C500

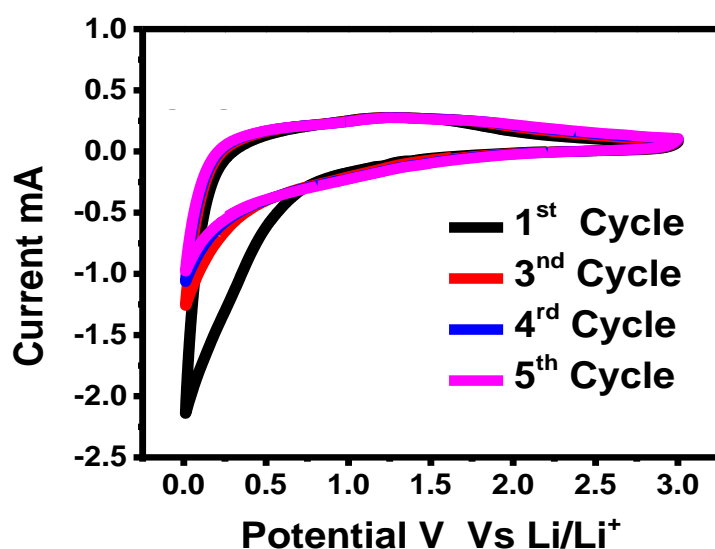


Figure 3.17 Cyclic voltammogram (CV) (scan rate = 0.1 mV/s)

The CV measurement was carried out to characterize the electrochemical performance. Figure 3.15 shows the first five CV curves of the C500 electrode at room temperature between 0.005 and 3 V at a scanning rate of 0.1 mV/s. The CV curve of the first cycle was different from the subsequent cycles, especially during discharging. A cathodic peak at 0.2 V due to lithiation and delithiation appeared at 0.4 V vs. Li/Li^+ . The anodic peak at 1.2 V indicated breaking of Li bonds with defect sites during the charging process.²⁶ The CV curves almost overlapped from the second cycle onwards, indicating the stable and superior reversibility of the prepared carbon materials. To get further insight into the electrochemical

process, EIS was carried out using a three-electrode system to obtain the Nyquist plot (Figure 3.16a). The results showed that the charge transfer impedance (R_{ct}) of the material was 114Ω between the electrode and electrolyte.

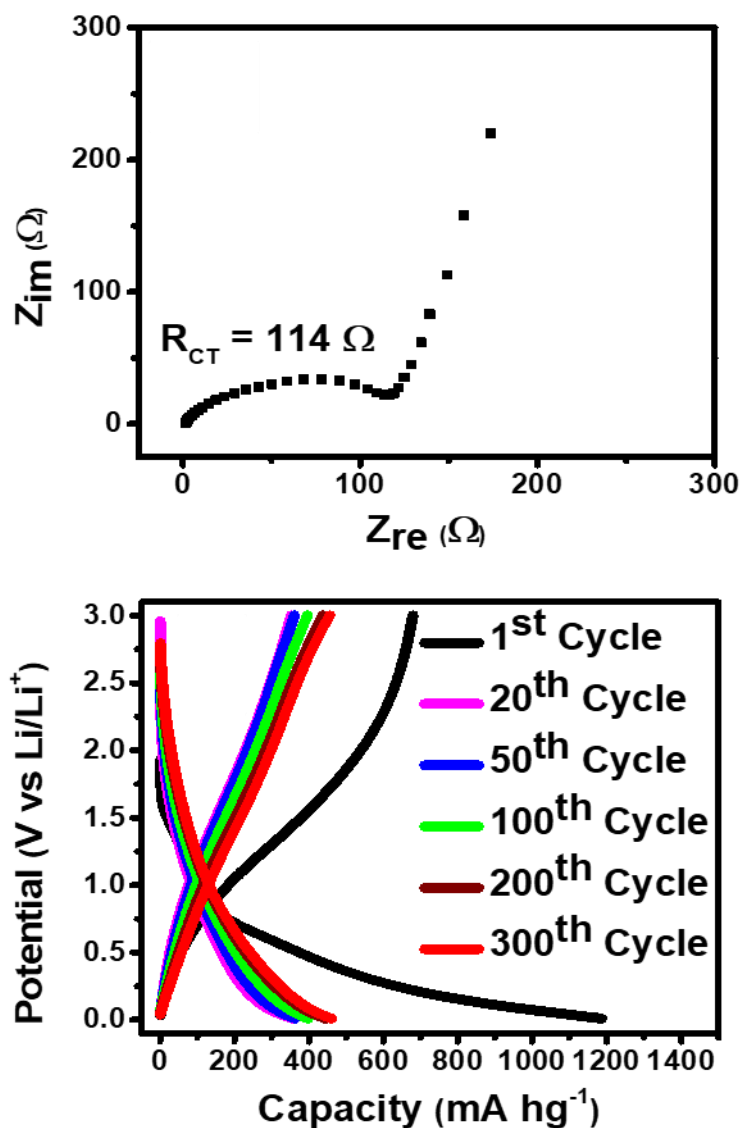


Figure 3.18 (a) Nyquist plots the electrodes containing C500; (b) Discharge-charge voltage profile of the electrode containing C500 in the half-cell with respect to Li/Li^+ .

The first charge-discharge curve (Figure 3.16b) shows a slopy plateau at 0.8 V, which arises from the formation of the solid electrolyte interphase (SEI). The initial discharge and charge specific capacities were 1187 and $680\ mA h g^{-1}$, respectively, based on the total mass of the C500. This corresponded to an initial Coulombic efficiency of 57.25% at a low current of $100\ mA g^{-1}$ for the C500 nanosheets electrode.²⁶ The discharge capacity of the second cycle

decreased to 679.4 mAh/g. The irreversible capacity loss of 507.6 mAh/g could have been caused by both the decomposition of the electrolyte on the graphene surface and strong Li ion adsorption.

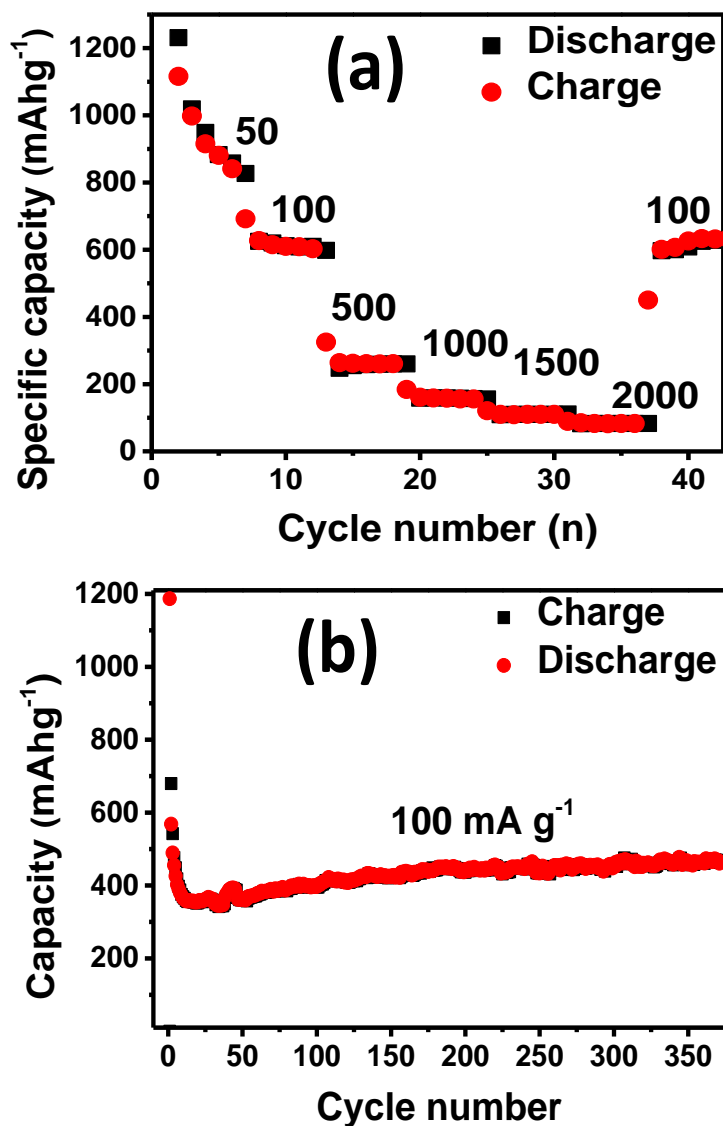


Figure 3.19 (a) Rate capability profile; (b) cyclic cycling performance of the electrode containing C500 nanosheets in the half-cell with respect to Li/Li⁺.

The rate capability of the C500 nanosheets was evaluated under a wide range of current densities (from 100 mA g⁻¹ to 2 Ag⁻¹) (Figure 3.17a). A capacity of 36 m Ahg⁻¹ was obtained at a high current density of 2 Ag⁻¹. The capacity was recovered to the initial level when the current density was reverted to 100 mA g⁻¹, demonstrating the stability and reversibility of the C500 nanosheets. The cycling performance of the C500 nanosheets electrode was measured

at 100 m Ag⁻¹ over 370 cycles (Figure 3.17b). The initial charge and discharge capacities were 1187 and 670 m Ahg⁻¹, respectively, while the Coulombic efficiency was 56.5%. After 370 cycles, the reversible capacity of the C500 nanosheets electrode was maintained at 470 m Ahg⁻¹; however, the Coulombic efficiency increased to 100%.²⁶

3.3.3.2 Electrochemical performance of the C700

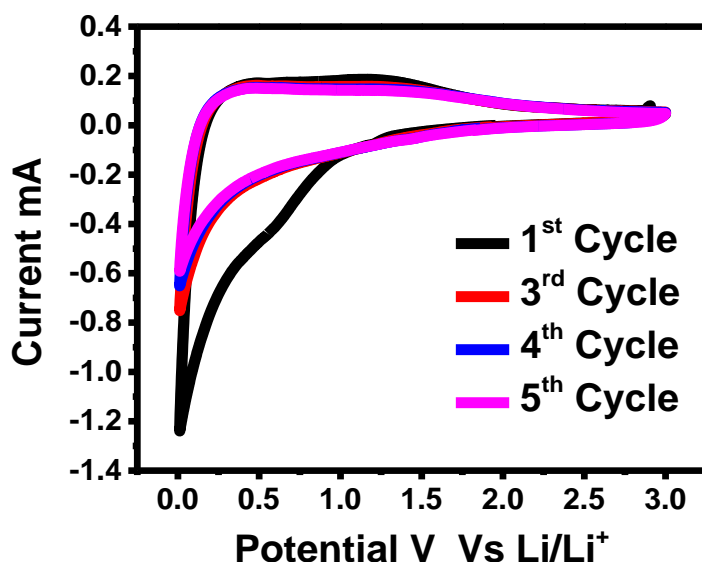


Figure 3.20 cyclic cycling performance of the electrode containing C700 nanosheets in the half-cell with respect to Li/Li⁺.

The CV (Figure 3.18) of C700 shows a peak at 0.5 V during the Li-insertion process, attributed to the occurrence of the side reactions on the electrode surface due to the SEI film formation.²⁷ The impedance performance of the C700 was evaluated from the Nyquist plot of the electrodes (Figure 3.19a) and charge-discharge galvanostatic voltage profile (Figure 3.19b) in a CR2032 coin cell. The results show that the R_{ct} of the material was 39.5 Ω between the electrode and electrolyte. The charge-discharge curve had a shape similar to those of other carbon materials. The initial discharge and charge specific capacities were 1180 and 654 m Ahg⁻¹, respectively based on the total mass of the C700. This corresponds to an initial Coulombic efficiency of 55.45% at a low current of 100 mAg⁻¹ for the C700 nanosheet electrode.

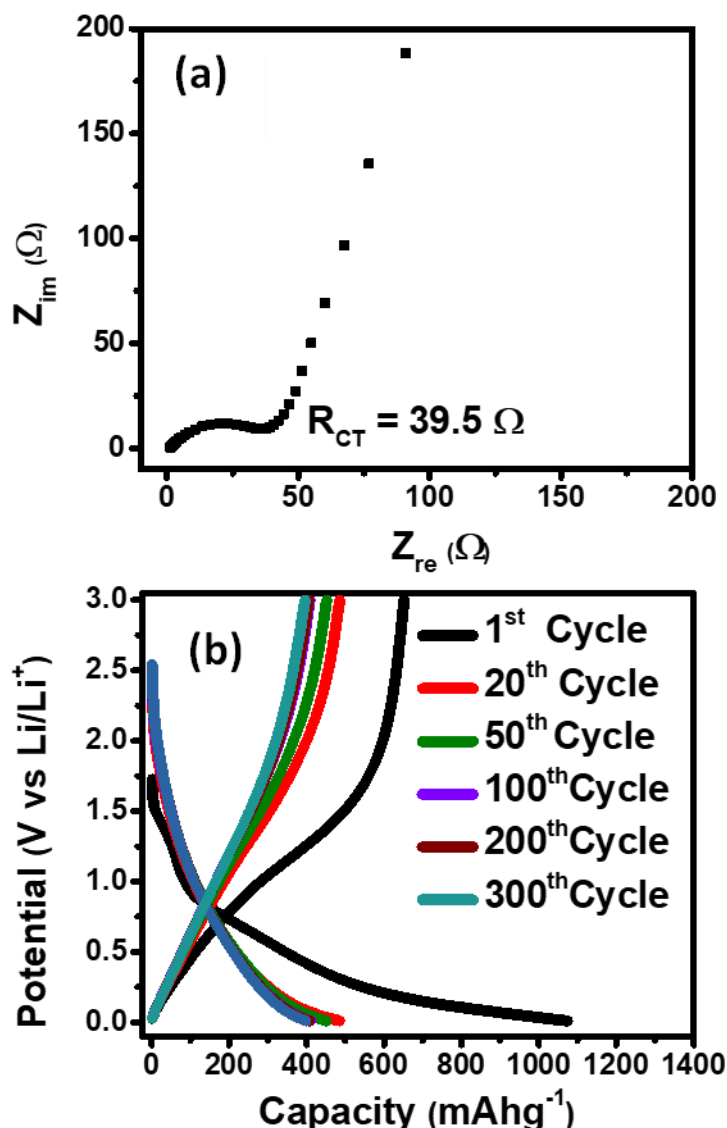


Figure 3.21(a) Nyquist plots of the electrodes containing C700 material; (b) Discharge-charge voltage profile of the electrode containing C700 in the half-cell with respect to Li/Li⁺.

The rate capability of the C700 nanosheets was evaluated under a wide range of current densities (from 100 mA g⁻¹ to 3 Ag⁻¹) (Figure 3.20a). A capacity of 223 m Ahg⁻¹ was obtained at a high current density of 3 Ag⁻¹. The capacity was recovered to the initial level when the current density was reverted to 100 mA g⁻¹, demonstrating the stability and reversibility of the C700 nanosheets. The cycling performance was measured at 100 m Ag⁻¹ for 400 cycles (Figure 3.20b). As shown in figure 3.20b, the initial charge and discharge capacities were 1075 and 655 m Ahg⁻¹, respectively, while the Coulombic efficiency was 60.5%. After 400 cycles, the reversible capacity of the C700 nanosheets electrode was maintained at 400 m Ahg⁻¹; however, the Coulombic efficiency increased to 100%.

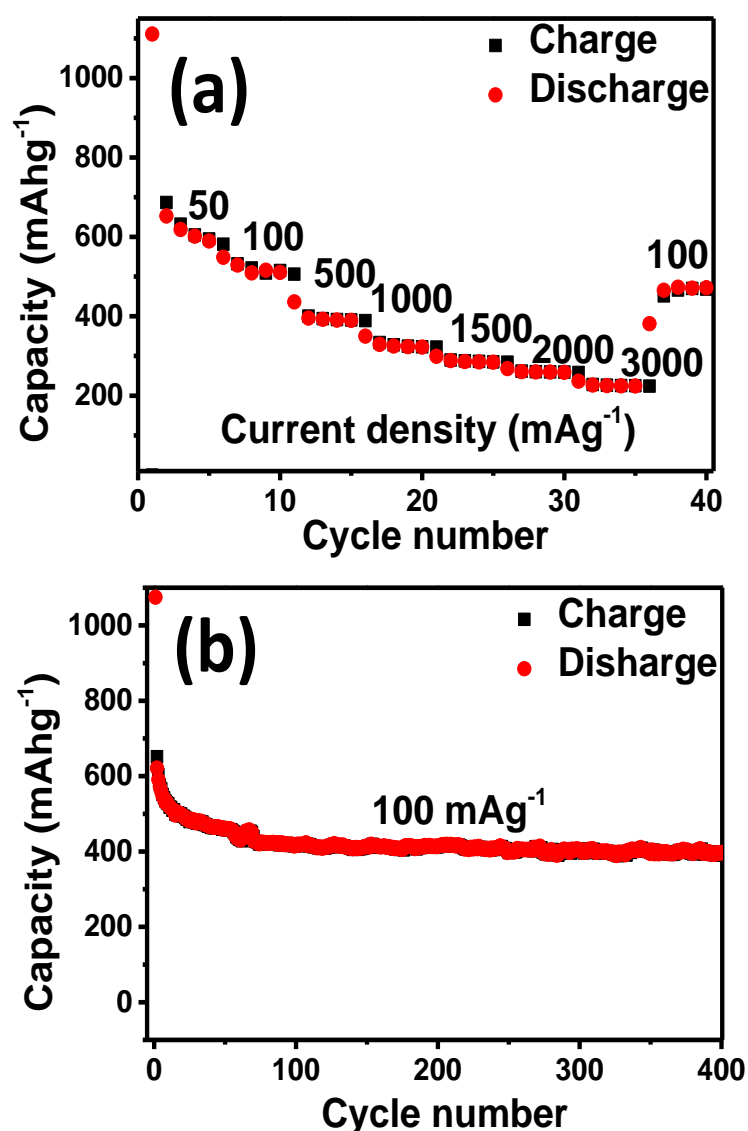


Figure 3.22 (a) Rate capability profile; (b) cyclic performance of the electrode containing the C700 nanosheets in the half-cell with respect to Li/Li⁺.

3.4 Summary

A simple low-cost method for the direct large-scale production of nitrogen-rich carbon nanosheets from 1,4-bis-(trimethylsilyl)-1,4-diaza-2,5-cyclohexadiene under ambient conditions at room temperature was demonstrated. The as-prepared carbon nanosheets (CRT) had a high nitrogen doping level (22.2 at.%) and contained unique nitrogen doping species (pyridinic N and pyrrolic N). After annealing the CRT at 500 and 700 °C, the nitrogen content was reduced to 20.1 and 14.1%, respectively. These results show that carbon nanosheets have a promising electrochemical performance as an anode material in Li-ion

batteries. Therefore, this study provides general guidance for the development of high-performance carbon-based electrode materials for energy conversion and storage applications.

References

1. D. Jana, C.-L. Sun, L.-C. Chen, K.-H. Chen, *Prog. Mater. Sci.* **2013**, *58*, 565–635
2. a) U. N. Maiti, W. J. Lee, J. M. Lee, Y. Oh, J. Y. Kim, J. E. Kim, J. Shim, T. H. Han, S. O. Kim, *Adv. Mater.* **2014**, *26*, 40–66; b) B. G. Sumpter, J. Huang, V. Meunier, J. M. Romo-Herrera, E. Cruz-Silva, H. Terrones, M. Terrones, *Int. J. Quantum Chem.* **2009**, *109*, 97–118.
3. a) E. A. Ekimov, V. A. Sidorov, E. D. Bauer, N. N. Mel'nik, N. J. Curro, J. D. Thompson, S. M. Stishov, *Nature*, **2004**, *428*, 542–545; b) S.-M. Jung, E. K. Lee, M. Choi, D. Shin, I.-Y. Jeon, J.-M. Seo, H. Y. Jeong, N. Park, J. H. Oh, J.-B. Baek, *Angew. Chem. Int. Ed.* **2014**, *53*, 2398–2401; *Angew. Chem. Int. Ed.* **2014**, *126*, 2430–2433.
4. a) R. Czerw, M. Terrones, J. C. Charlier, X. Blase, B. Foley, R. Kamalakaran, N. Grobert, H. Terrones, D. Tekleab, P. M. Ajayan, W. Blau, M. R_hle, D. L. Carroll, *Nano Lett.* **2001**, *1*, 457–460; b) W.-Q. Han, P. Kohler-Redlich, T. Seeger, F. Ernst, M. R_hle, N. Grobert, W.-K. Hsu, B.-H. Chang, Y.-Q. Zhu, H. W. Kroto, D. R. M. Walton, M. Terrones, H. Terrones, *Appl. Phys. Lett.* **2000**, *77*, 1807–1809; c) B. G. Sumpter, V. Meunier, J. M. Romo-Herrera, E. Cruz-Silva, D. A. Cullen, H. Terrones, D. J. Smith, M. Terrones, *ACS Nano* **2007**, *1*, 369–375; d) M. Terrones, H. Terrones, N. Grobert, W. K. Hsu, Y. Q. Zhu, J. P. Hare, H. W. Kroto, D. R. M. Walton, P. Kohler-Redlich, M. R_hle, J. P. Zhang, A. K. Cheetham, *Appl. Phys. Lett.* **1999**, *75*, 3932–3934.
5. E. Cruz-Silva, D. A. Cullen, L. Gu, J. M. Romo-Herrera, E. MuCoz-Sandoval, F. L_pez-Ur_as, B. G. Sumpter, V. Meunier, J.-C. Charlier, D. J. Smith, H. Terrones, M. Terrones, *ACS Nano* **2008**, *2*, 441–448.
6. a) Z. Yang, Z. Yao, G. Li, G. Fang, H. Nie, Z. Liu, X. Zhou, X. A. Chen, S. Huang, *ACS Nano* **2012**, *6*, 205–211; b) I.-Y. Jeon, S. Zhang, L. Zhang, H.-J. Choi, J.-M. Seo, Z. Xia, L. Dai, J.-B. Baek, *Adv. Mater.* **2013**, *25*, 6138–6145; c) Q. Fan, H.-J.

- Noh, Z. Wei, J. Zhang, X. Lian, J. Ma, S.-M. Jung, I.- Y. Jeon, J. Xu, J.-B. Baek, *Nano Energy***2019**, 62, 419– 425.
7. D. Wei, Y. Liu, Y. Wang, H. Zhang, L. Huang, G. Yu, *Nano Lett.***2009**, 9, 1752 – 1758.
 8. a) S. Latil, S. Roche, D. Mayou, J.-C. Charlier, *Phys. Rev. Lett.***2004**, 92, 56805; b) K.-Y. Chun, H. S. Lee, C. J. Lee, *Carbon***2009**, 47, 169– 177; c) J. O. Hwang, J. S. Park, D. S. Choi, J. Y. Kim, S. H. Lee, K. E. Lee, Y.-H. Kim, M. H. Song, S. Yoo, S. O. Kim, *ACS Nano***2012**, 6, 159 –167; d) H. C. Choi, S. Y. Bae, J. Park, K. Seo, C. Kim, B. Kim, H. J. Song, H.-J. Shin, *Appl. Phys. Lett.***2004**, 85, 5742 –5744; e) A. Bostwick, F. Speck, T. Seyller, K. Horn, M. Polini, R. Asgari, A. H. MacDonald, E. Rotenberg, *Science***2010**, 328, 999–1002.
 9. a) Y. Liang, Y. Li, H. Wang, J. Zhou, J. Wang, T. Regier, H. Dai, *Nat. Mater.***2011**, 10, 780– 786; b) J. Wu, Z. Pan, Y. Zhang, B. Wang, H. Peng, *J. Mater. Chem. A***2018**, 6, 12932 – 12944.
 10. S. Park, D. Srivastava, K. Cho, *Nano Lett.***2003**, 3, 1273 –1277.
 11. G. V. Bianco, M. Losurdo, M. M. Giangregorio, P. Capezzuto and G. Bruno, Exploring and rationalising effective n-doping of large area CVD-graphene by NH₃, *Phys. Chem. Chem. Phys.* **2014**, 16, 3632-3639.
 12. A. Javid, M. Kumar and J. G. Han, Study of sterilization-treatment in pure and N-doped carbon thin films synthesized by inductively coupled plasma assisted pulsed-DC magnetron sputtering, *Appl. Surf. Sci.* **2017**,392, 1062-1067.
 13. M. Glerup, J. Steinmetz, D. Samaille, O. Stephan, S. Enouz, A. Loiseau, S. Roth and P. Bernier, Synthesis of N-doped SWNT using the arc-discharge procedure, *Chem. Phys. Lett.***2004**, 387, 193-197.
 14. D. H. Deng, X. L. Pan, L. A. Yu, Y. Cui, Y. P. Jiang, J. Qi, W. X. Li, Q. A. Fu, X. C. Ma, Q. K. Xue, G. Q. Sun and X. H. Bao, Toward N-Doped Graphene via Solvothermal Synthesis, *Chem. Mater.* **2011**,23, 1188-1193.
 15. C. H. Zhang, L. Fu, N. Liu, M. H. Liu, Y. Y. Wang and Z. F. Liu, Synthesis of Nitrogen-Doped Graphene Using Embedded Carbon and Nitrogen Sources, *Adv. Mater.* **2011**,23, 1020-1024.
 16. M. S. He, S. Zhou, J. Zhang, Z. F. Liu and C. Robinson, CVD growth of N-doped carbon nanotubes on silicon substrates and its mechanism, *J. Phys. Chem. B*, **2005**,109, 9275-9279.

17. H. G. Wang, Z. Wu, F. L. Meng, D. L. Ma, X. L. Huang, L. M. Wang and X. B. Zhang, Nitrogen-Doped Porous Carbon Nanosheets as Low-Cost, High-Performance Anode Material for Sodium-Ion Batteries, *ChemSusChem*, **2013**,6, 56-60.
18. J. K. Ou, L. Yang, Z. Zhang and X. H. Xi, Nitrogen-doped porous carbon derived from horn as an advanced anode material for sodium ion batteries, *Micropor Mesopor Mat.***2017**,237, 23-30.
19. R. K. Raut, S. F. Amin, P. Sahoo, V. Kumar, M. Majumdar, *Inorganics*, **2018**, 6, 69.
20. T. Yurino, Y. Ueda, Y. Shimizu, S. Tanaka, H. Nishiyama, H. Tsurugi, K. Sato, K. Mashima, *Angew. Chem. Int. Ed.* **2015**, 54, 14437-14441.
21. Akula. N, Sharma. N, Lohenaonkar. A, Ogale. B. S, Majumdar. M, *ChemAsianJ.***2020**, 15,585–589
22. J. Chen, Z. Mao, L. Zhang, Y. Tang, D. Wang, L. Bie, B. D. Fahlman, *Carbon*, **2018**, 130, 41-47.
23. S. Zhang, K. Dokko, M. Watanabe, *Chem. Mater.* **2014**, 26, 2915-2926.
24. Y. Wang, Y. Shao, D. W. Matson, J. Li, Y. Lin, *ACS Nano*, **2010**, 4, 1790- 1798.
25. H. Wang, T. Maiyalagan, X. Wang, *ACS Catal.* **2012**, 2, 781-794.
26. Z. Xing, Z. Ju, Y. Zhao, J. Wan, Y. Zhu, Y. Qiang and Y. Qian, *Sci. Rep.***2016**, 6, 26146.
27. Chen J, Mao Z, Zhang L, Tang Y, Wang D, Bie L, *Carbon***2018**, 130, 41-7.

Chapter 4

Simultaneous Synthesis and Characterisation of Antimony-Graphitic Nanocomposite and its anode performance in Li ion Battery

4.1 Introduction

The high energy density and long cycle life time of Li ion batteries have enabled them to be extensively used for energy storage in multiple devices. However, Li ion batteries are expensive and have safety problems. In addition, lithium is a limited resource.¹⁻³ Therefore, an inexpensive energy storage devices is desirable. Sodium is more naturally abundant than lithium. Its lower cost also makes it a good alternative to Li ion batteries at room temperature.^{4,5} However, the sodium ion is larger than the lithium ion; hence, its insertion into graphite is considerably less than that of the lithium ion used in commercially available Li ion batteries. Therefore, graphite is less used in sodium ion batteries.⁶⁻⁸ Finding an appropriate anode material for sodium ion batteries is challenging; however, hard carbon materials have had most of the attention due to their low price, high natural abundance, and environment-friendliness.⁹ However, most of the capacity of the material is obtained between 0 and 0.1 V which is at a low plateau. This causes safety issues during the fast charging of the device.^{6,10} Furthermore, the low rate capability of the hard carbon materials is not favourable for application in commercial batteries.^{8,11,12} To overcome these issues, other high-capacity materials can be used along with carbon materials to increase the overall volumetric capacity of the composite. Sb has emerged as a suitable candidate for use in sodium ion battery due to its suitable insertion potential and theoretical capacity of 660 m Ahg⁻¹ (Na₃Sb).¹³⁻¹⁶ Sb also has better stability and conductivity than P, which is in the same group, which is addition to the electrochemical application.¹⁷ The volumetric expansion of the antimony electrode material causes capacity fading due to its pulverization.^{18,19,20} Several attempts have been made to solve this problem, such as decreasing the size of Sb and preparing different types of Sb nanomaterials.⁴⁶ There have been many reports on several Sb nanocomposites, such as Sb@C nanocomposites,²¹ hollow Sb spheres,²² monodisperse Sb nanocrystals,²⁹ Sb-graphite nanocomposites,²⁴ hollow Sb particles,²³ and Sb yoke shell composites, for efficient Li ion storage.^{25,26} However, the methods for the synthesis of these Sb nanocomposite materials are complicated and require expensive starting materials.^{20,30,31,47-50} Therefore, a simple, low-cost, and eco-friendly synthesis method is required. Herein we report the colloidal synthesis method, which uses 1,4-bis-(trimethylsilyl)-1,4-diaza-2,5-cyclohexadiene, and SbCl₃ as precursors. The resulting nanocomposite had better electrochemical performance characteristics, good rate capability, and reversible capacity.

4.2 Experimental Sections

4.2.1 General Remarks.

Synthesis: All chemicals were purchased from Sigma-Aldrich and used as received. Tetrahydrofuran and pentane were refluxed over sodium/benzophenone and distilled prior to use. Acetone and toluene were simply distilled prior to use. Oleylamine was stirred overnight at 100 °C under vacuum prior to use. Meanwhile, 1,4-bis(trimethylsilyl)-1,4-diaza-2,5-cyclohexadiene was prepared according to a reported procedure . The annealation was done in Nabertherm RHTC 80-710/15.

4.2.2 Synthesis of the Sb/NG: 1,4-Bis-(trimethylsilyl)-1,4-diaza-2,5-cyclohexadiene dissolved in oleylamine (4 mL, 12.15 mmol) was heated to 150 °C in argon atmosphere in a three-necked flask fitted with a reflux condenser. When the temperature was reached, a toluene (2 mL) solution of SbCl₃ was rapidly injected. Antimony is metallic in nature and forms bulk Sb crystals at low temperatures; hence, SbCl₃ was injected here instead of the reducing agent. The solution colour instantaneously turned intense brown-red. The reaction temperature was increased to 165 °C (ramp up rate = 10 °C/min) and maintained for 1 min. Subsequently, the reaction mixture was quenched to room temperature. The solution was then transferred to a centrifuge tube containing 2–3 mL of toluene. The Sb/NG was precipitated by adding 20 mL of acetone and then separated by centrifugation (9000 rpm for 10 min). After decanting the supernatant, the precipitate was re-suspended in 5 mL of toluene, with 25 mL of acetone added as the non-solvent. This process of dissolution/precipitation/centrifugation was repeated several times until all the impurities were removed to yield 150 mg of a black solid.

4.2.3 Synthesis of the Sb/NG/C: The Sb/NG (150 mg) was annealed at 500 °C for 2 h under argon containing 5% hydrogen in a furnace to yield a black powder Sb/NG/C (85 mg). The heating rate was 2 °C/min.

4.2.4 Characterisation: The powder X-ray Diffraction (XRD) of the Sb-graphenic nanocomposites were recorded using a Bruker D8 Advance X-ray diffractometer equipped with Cu K α radiation (1.54 Å). The Raman spectra of the nanocomposites were analysed using the LabRAM HR800 from Yvon Horiba. Meanwhile, the X-ray photoelectron spectroscopy (XPS) data were collected using the PHI 5000 Versa Probe II, FEI Inc. SEM analysis was carried out using a FEI Nova Nano 450 SEM. The BET adsorption measurements for surface area calculations were carried out using a Quadrasorb automatic

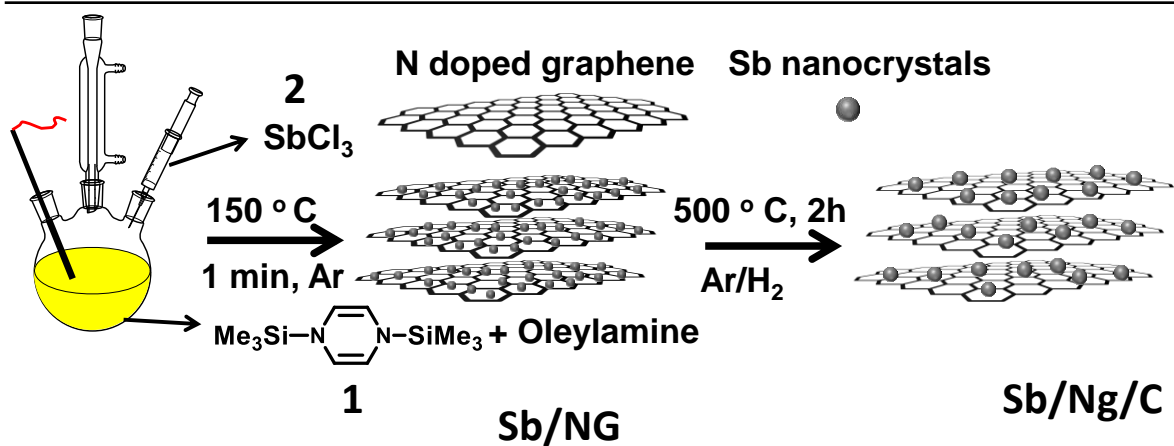
volumetric instrument. The AFM data were collected by the Keysight atomic force microscope (model: AFM 5500) using the tapping mode technique. The Fourier-transform infrared (FTIR) spectra were collected using nanocomposites pellets and KBr on a Thermo scientific NICOLET 6700 FTIR spectrophotometer. The TEM images were taken using a JEOL JEM 2100 FS field-emission transmission electron microscope at 200 kV. The CHN analyses were performed using Elementar vario EL analyser. The thermogravimetric analysis was performed in air using TGA Perkin-Elmer STA6000.

4.2.5 Electrochemical Measurements: The electrodes were prepared from a slurry of Sb/NG/C, conducting carbon, and PVDF binder at a weight ratio of 80:10:10 using NMP as solvent. The slurry was coated onto a Cu foil and dried overnight at 80 °C. Then, the foil was punched into 1-cm² circular discs. The CR-2032 coin half-cell was assembled using this composite as the working electrode and metallic Li foil as the counter and reference electrode. The mass of active material loaded on the electrode was 1.0 mg. A Whatmann was used as the separator, while 1 M LiPF₆ in a 1:1 (v/v) mixture of EC and DMC was used as the commercial electrolyte. All the cells were assembled inside an argon-filled glove box. The galvanostatic charge-discharge measurements were performed using BTS-Neware (China) 5 V, 10 mA battery tester. The impedance and cyclic voltammetry were performed using VMP3 Biologic system equipped with potentiostat and galvanostat channels.

4.3 Results and Discussion

4.3.1 Preparation of Sb/NG Nanocomposite

In a typical reaction in inert atmosphere, 2.16 mmol of 1,4-bis-(trimethylsilyl)-1,4-diaza-2,5-cyclohexadiene was dissolved in 24.3 mmol of oleylamine in a three-necked round-bottomed flask and was heated to 150 °C. When the reaction temperature reached 150 °C, a 3.3 mmol solution of SbCl₃ solution in toluene was rapidly injected leading to an immediate temperature drop to ~130 °C. The solution turned dark brownish-red instantaneously. After the temperature had recovered to 150 °C, the reaction temperature was raised to 165 °C (ramp up rate = 10 °C/min) and maintained for 1 min. After subsequent cooling to room temperature, the dark brown solid was isolated using the solvent/non-solvent technique.³² The washing and centrifugation were repeated until all the impurities, such as unbound oleylamine, were removed. This method is gram-scalable and the resulting dark-brown solid Sb/NG was dried. The Sb/NG forms a stable colloidal suspension in toluene. A burst of homogeneous nucleation followed by controlled growth from the hot injection method led to a high-quality monodispersed Sb/NG nanocomposite.



Scheme: Schematic of the synthesis of the Sb/NG and Sb/NG/C nanocomposites.

4.3.2 Structural and Microscopic Characterisations

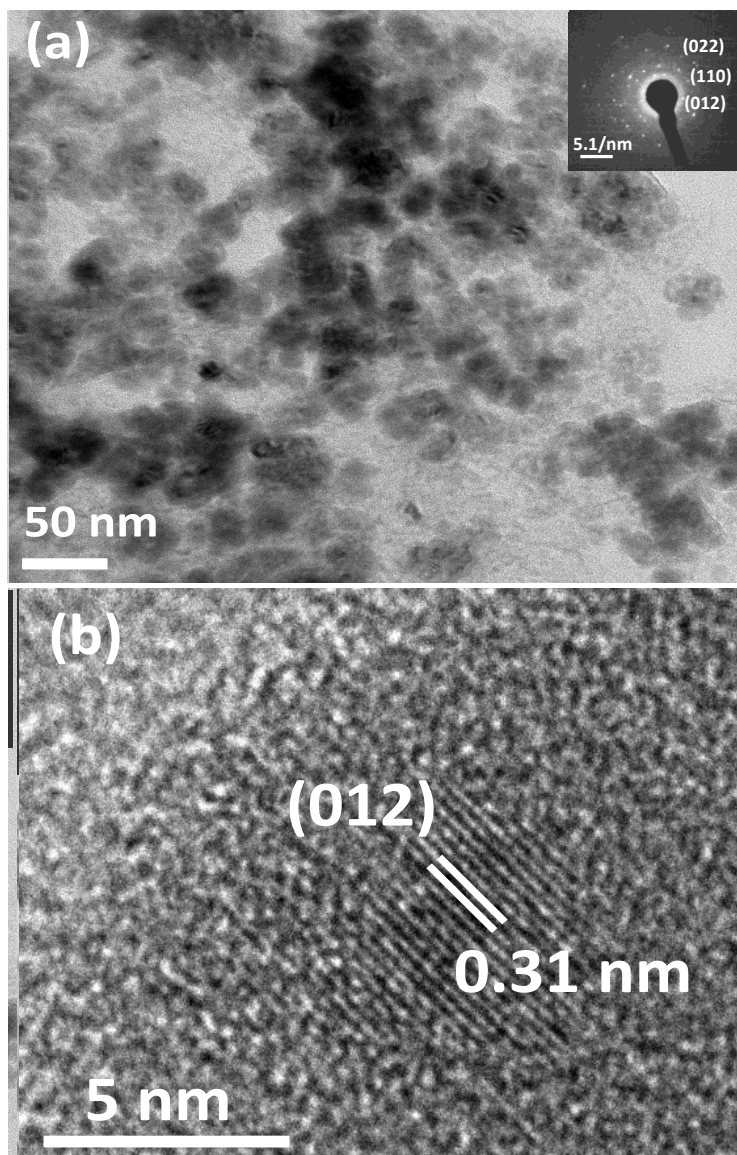


Figure 4.1 (a) TEM image; (b) HRTEM image;

The TEM image (Figure 4.1a) reveals that the Sb NCs are uniformly and densely anchored³⁵ on the graphitic nanosheets. The mean size of the Sb NCs was approximately 10 nm which could be determined from the HRTEM (Figure 4.1b). The lattice fringes had interlayer spacing of 0.31 nm (Figure 4.3a), which agrees well with the (012) plane of the diamond cubic Sb and matches with the interlayer spacing calculated from the PXRD.

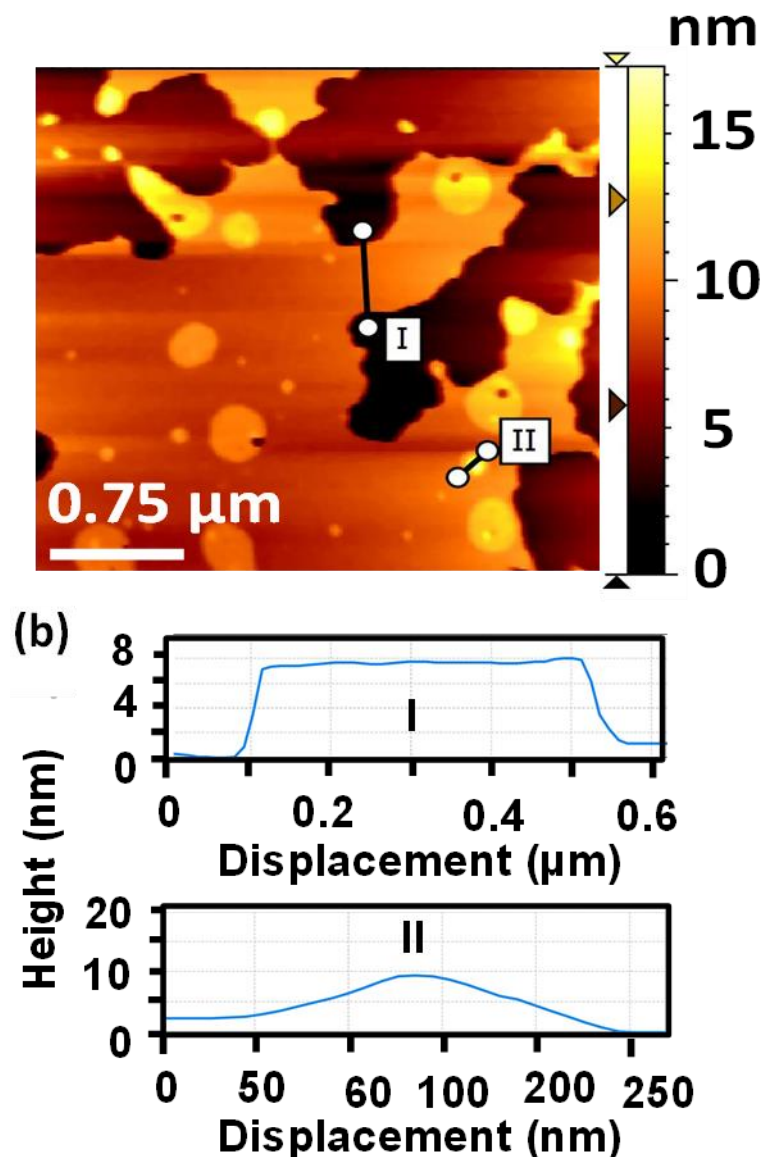


Figure 4.2 (a) AFM image; (b) height profiles for the lines I and II in the AFM image of Sb/NG

The selected-area electron diffraction (SAED) pattern also reveals that the Sb NCs had a diamond cubic structure. No diffraction patterns associated with the graphitic sheets were observed indicating the poor degree of graphitisation. The profile height obtained from the

AFM images (Figures 4.2a, b) shows a nanosheet thickness of ~ 8 nm, characteristic of approximately 26 stacked graphene layers.

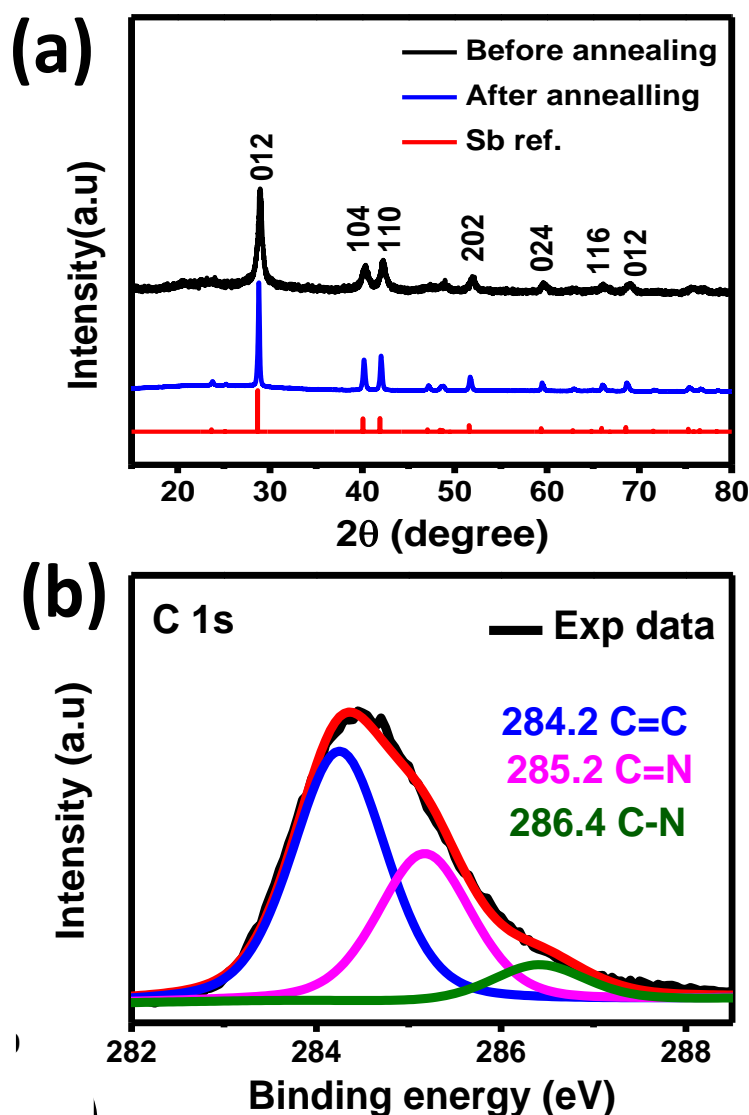


Figure 4.3 (a) PXRD pattern; (b) high-resolution XPS of C1s

The PXRD pattern (Figure 4.3a) of the as-synthesized Sb/NG display clear peaks at $2\theta = 28.8^\circ$, 40.3° , and 42.3° , which can be well indexed to the diamond cubic Sb (JCPDS card No. 35-0732). The calculated d-spacing based on the (012) peak was 0.31 nm. The XPS (Figure 4.7a) shows three signals, which can be assigned to Sb, C, and N. The fitted XPS spectra of the C1s display three peaks (Figure 4.3b). The main peak at 284.2 eV was assigned to the graphite-like sp^2 C.³³

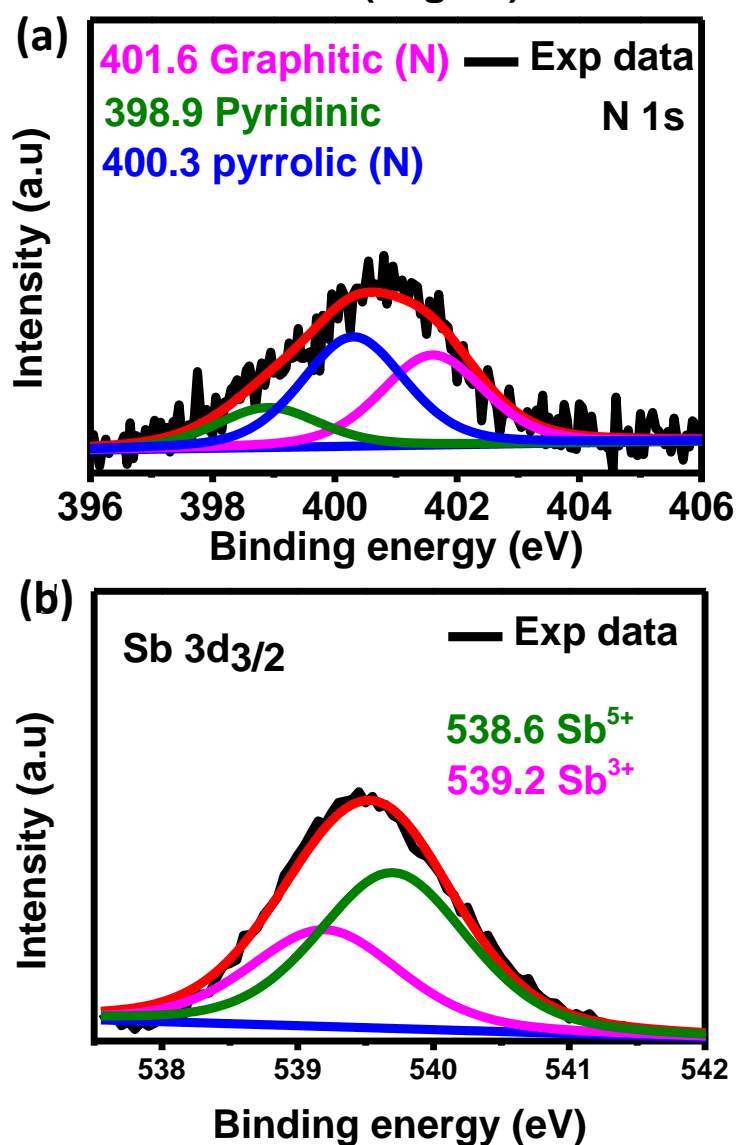


Figure 4.4 High-resolution XPS of the (a) C1s; (c) N1s sp (b) Sb 3d_{3/2} of the Sb/NG (before annealing).

Meanwhile, the other two peaks, centred at 285.2 and 286.4 eV, corresponded to the C=N and C-N groups, respectively.³³ The N1s spectra de-convoluted into three sub peaks at 398.8, 400.3 eV, and 401.6 eV corresponding to the pyridinic N, pyrrolic N, and graphitic N, respectively (Figure 4.4a).³⁴ The Sb 3/2 spectra showed peaks at 539.6 and 540.1 eV, corresponding to Sb 3d (Figure 4.4b). The N contents of the graphene obtained from CHN elemental analysis and XPS was ~8.7 wt.%. The doping of graphene with N adjust the electronic and physicochemical properties of the pristine graphene and improves its potential for application in devices.³⁵ The graphitization of carbon occurred at a low temperature (150

°C), indicating that the method is suitable for producing nanocomposites from highly metallic elements for electrochemical application.

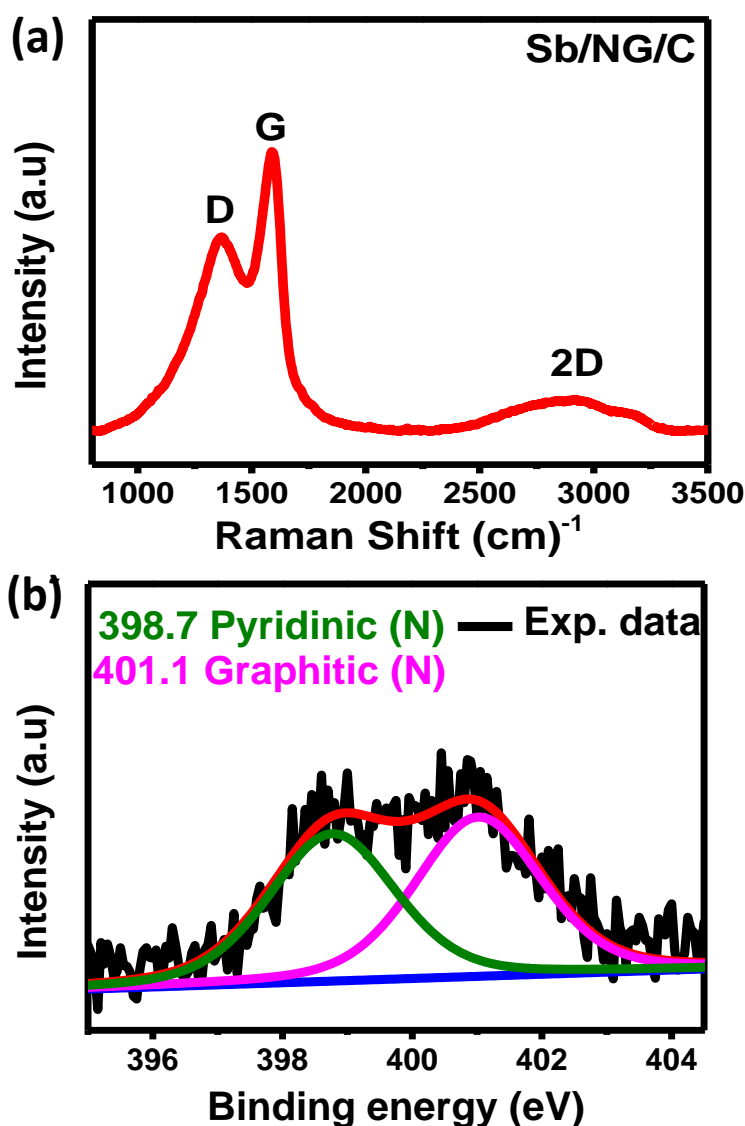


Figure 4.5 (a) Raman spectra of the Sb/NG/C; High resolution XPS of the (b) N1s sp;

The Sb/NG was subsequently annealed at 500 °C for 2 h under Ar containing 5% H₂. The carbonization led to the formation of carbon-coated Sb/NG/C with 70.8 wt.% Sb, as determined by thermogravimetric analysis³⁹ in air (Figure 4.6b). Meanwhile, the XRD pattern of the Sb/NG/C shows intense and sharp peaks corresponding to the diamond cubic phase of the Sb (Figure 4.3a).

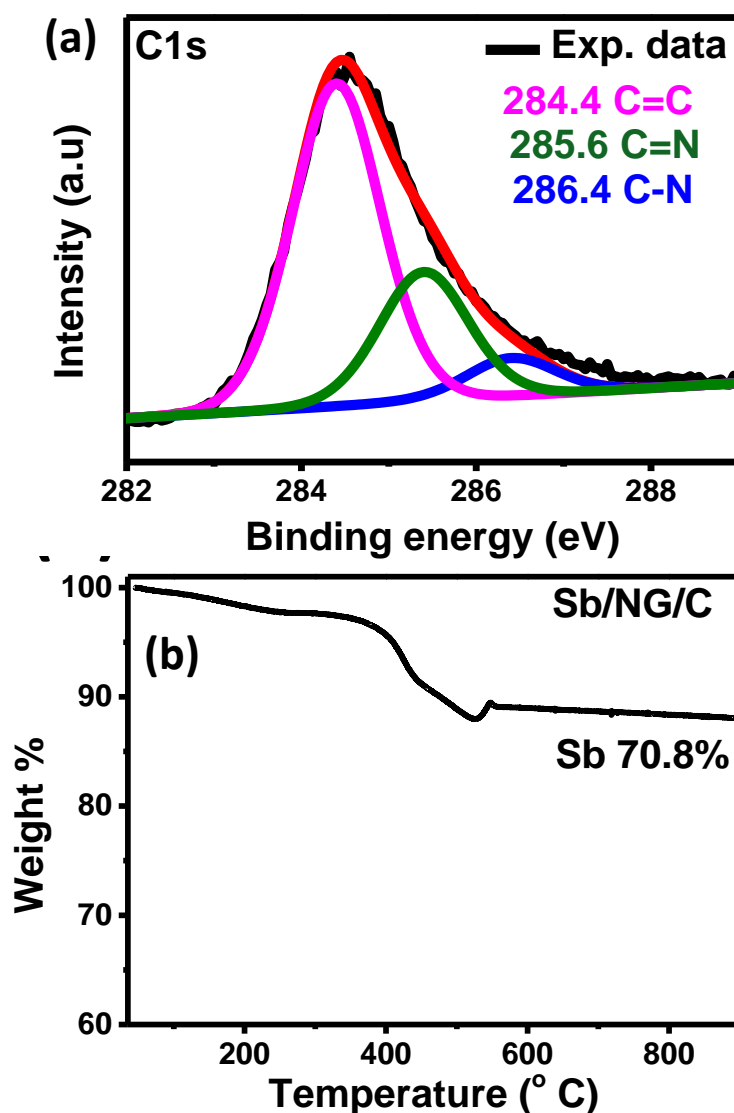


Figure 4.6 (a) C1s; (b) TGA of the Sb/NG/C in air.

The Raman spectra of the Sb/NG/C (Figure 4.5a) showed three characteristic peaks at 1342 and 1530 cm^{-1} , which were in good agreement with the typical optical modes of D band (disorder-induced phonon mode) and G band (graphitic band) of C, respectively. A distinct broad 2D peak, which is the D band second order, appeared at 2635 cm^{-1} in the Raman spectrum. Meanwhile, the XPS (Figure 4.7b) shows three signals which can be assigned to the Sb, C, and N. The fitted XPS spectra of the C1s display three peaks (Figure 4.6a). The main peak at 284.3 eV was assigned to the graphite-like sp² C.³³ The other two peaks centred at 285.6 and 286.4 eV corresponded to the C=N and C-N groups, respectively.³⁷ The N1s spectra de-convoluted into two sub peaks at 398.7 and 401.1 eV, corresponding to the

pyridinic N and graphitic N, respectively (Figure 4.6b).³⁸ The N content of the graphene, obtained from the CHN elemental analysis and XPS, was approximately 3.14 wt.%. The doping of graphene with N helped adjust the electronic and physicochemical properties of pristine graphene, and improved its potential for application in devices.³⁹

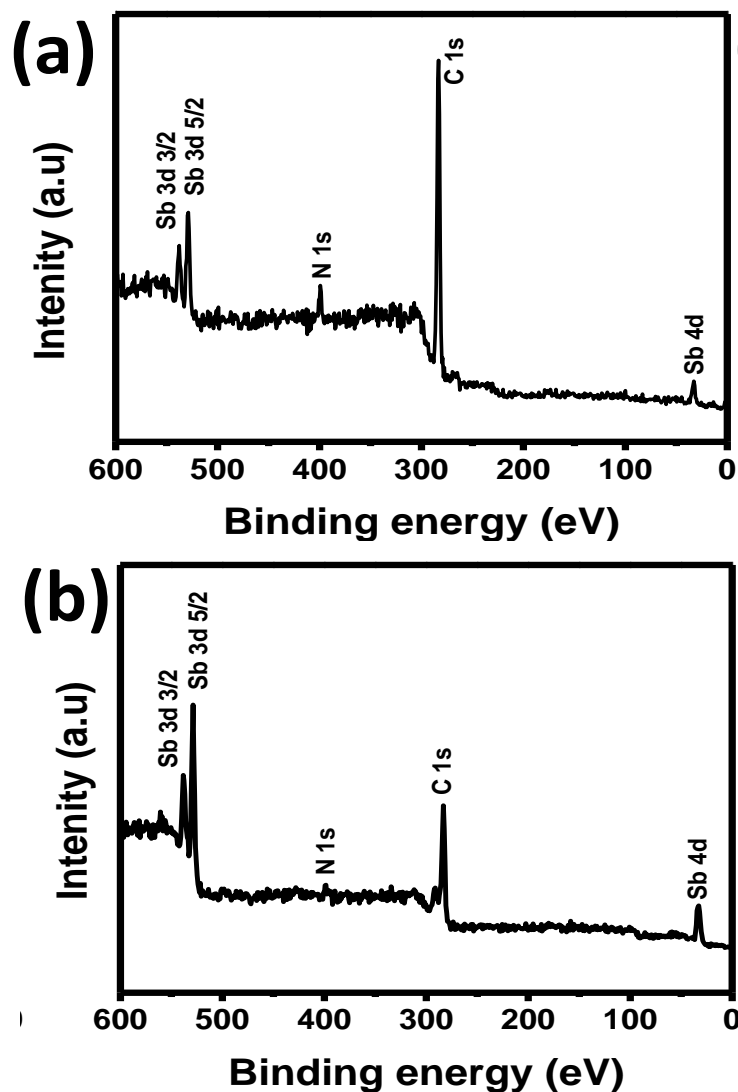


Figure 4.7 XPS survey spectrums of the (a) Sb/NG and (b) Sb/NG/C

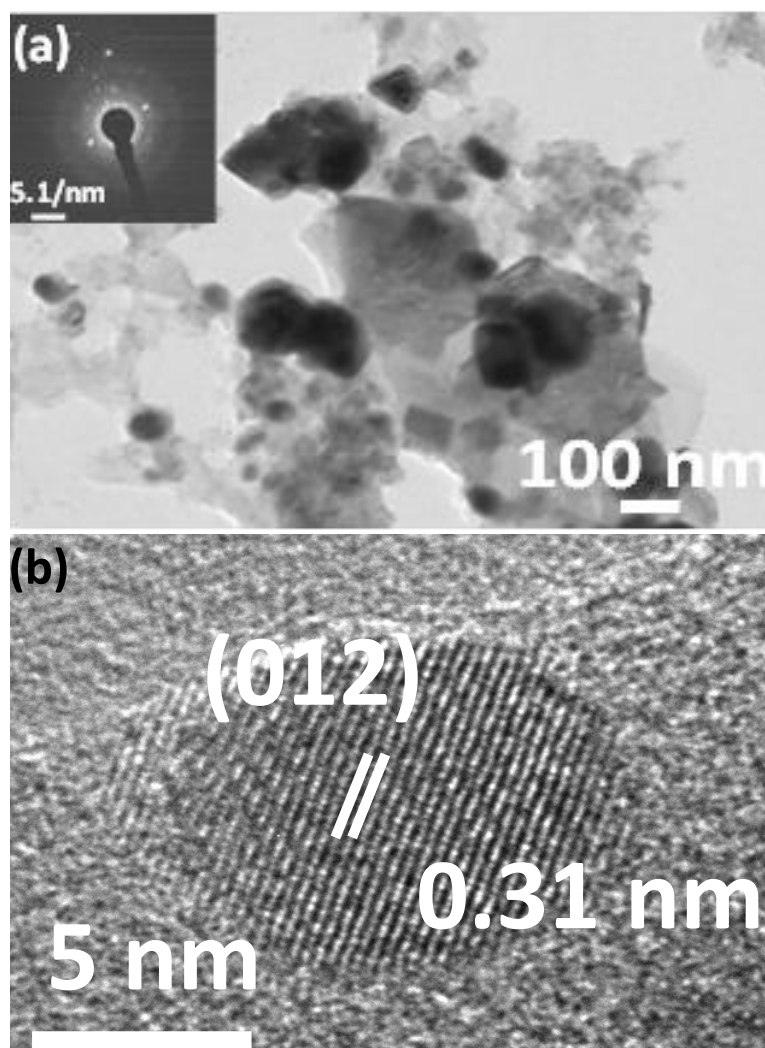


Figure 4.8 (a) TEM image; (b) HRTEM image;

The TEM image (Figure 4.8a) reveals that the Sb NCs were anchored⁴⁰ on the graphitic nanosheets. The mean size of the Sb NCs was ~30 nm, as determined from HRTEM (Figure 2.4b). The lattice fringes had an interlayer spacing of 0.31 nm (Figure 4.8b), which agrees well with the (012) plane of the diamond cubic Sb and matches with the interlayer spacing calculated from the PXRD. The SAED pattern also reveals that the Sb NCs had a diamond cubic structure (Figure 4.8a). No diffraction patterns associated with the graphitic sheets were observed indicating the poor degree of graphitisation.

4.3.3 Electrochemical properties

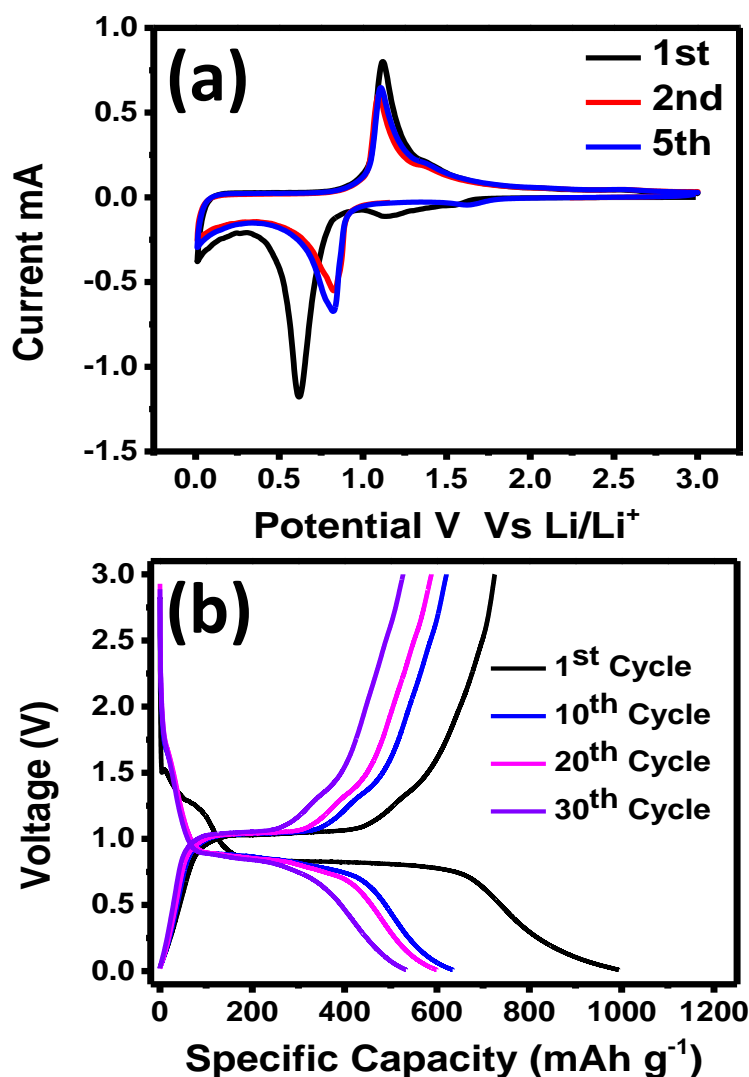


Figure 4.9 (a) CV (scan rate = 0.1 mV/s); (b) Discharge-charge voltage profile of the electrode containing the Sb/NG/C nanocomposite in the half-cell with respect to Li/Li⁺

The electrochemical performance of the Sb/NG/C was evaluated from the CV (Figure 4.9a) and charge-discharge galvanostatic voltage profile (Figure 4.9b) in a CR2032 coin cell. The scan rate of the Sb/NG/C electrode CV was 0.1 mV/s, between 0.01 and 1.5 V in the first three cycles of the Li ion batteries. The broad peak between 0.7 V and 0.4 V was attributed to the SEI films. Meanwhile, the first cycle was attributed to the lithiation reaction from antimony to Li_xSb.^{41, 42} In the following two cycles, the peak at 0.8 V corresponded to the lithiation of the crystalline antimony.⁴³ The anodic peak at 1.1 V was attributed to the delithiation reaction of the Li_xSb.^{44, 45} The voltage profiles of the Sb/NG/C during the first cycle revealed that the voltage plateaus on the discharge and charge curves were stable, with

cathodic and anodic peaks on the CV curves. The first discharge and charge capacities were 995.5 and 723.3 mA h g⁻¹ at a current density of 100 mA g⁻¹.

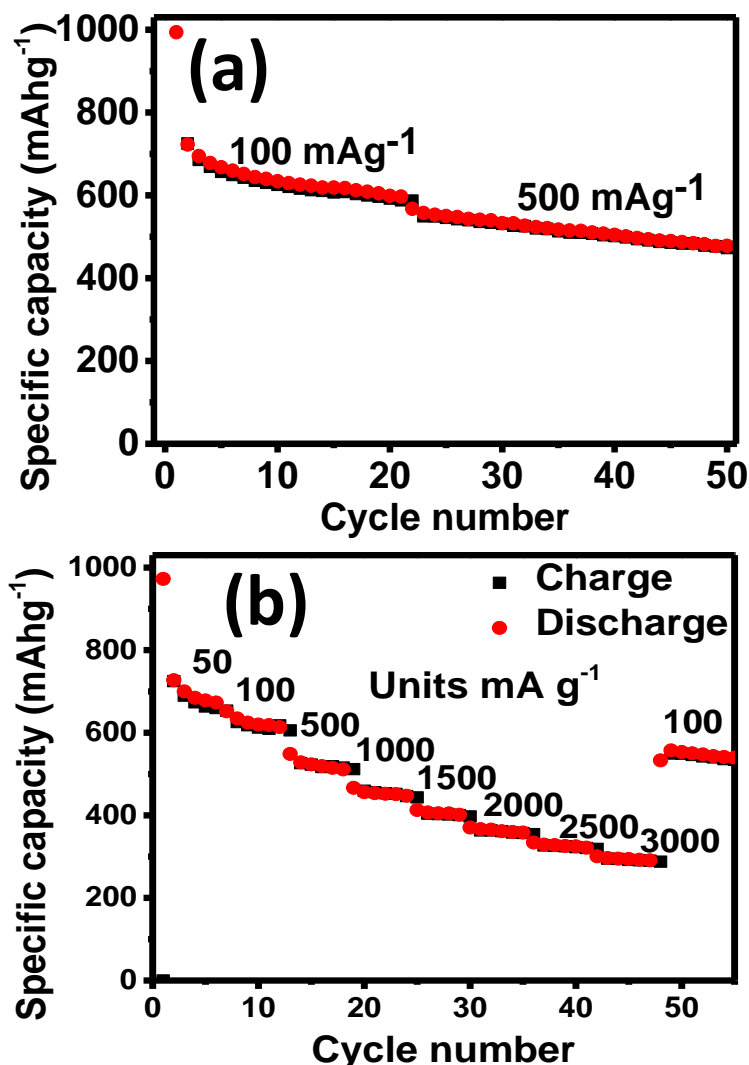


Figure 4.10 (a) Cycling performance and (b) rate capability profile of the electrode containing Sb/NG/C nanocomposite in the half-cell with respect to Li/Li⁺.

The cycling performance of the Sb/NG/C nanocomposite electrode was measured at 100 and 500 mA g⁻¹ (Figure 4.10a). The initial charge and discharge capacities were 993.9 and 725.05 mA h g⁻¹, respectively, at 100 mA g⁻¹, while the Coulombic efficiency was 72.5%. The current density was increased to 500 mA g⁻¹ after 20 cycles and the capacity was 477 mA h g⁻¹ at 50 cycles with a Coulombic efficiency of 98.9%. Meanwhile, the rate capability of the Sb/NG/C nanocomposite was evaluated under a wide range of current densities (from 50 mA g⁻¹ to 3 Ag⁻¹) (Figure 4.10b). A capacity of 290 mA h g⁻¹ was obtained at a high current density of 3

Ag⁻¹. The capacity was recovered to the initial level when the current density was reduced back to 100 m Ag⁻¹, demonstrating the good stability and reversibility of the Sb/NG/C nanocomposite.

4.4 Summary

We successfully synthesized an Sb/NG/C nanocomposites using a facile method, in which the active materials, i.e. Sb nanoparticles, were well encapsulated in an interconnected carbon matrix. This method also enables the large-scale synthesis of the Sb/NG/C nanocomposites owing to its simplicity and utilisation of cheaper raw materials.

References

- 1 Y. S. Wang, X. Q. Yu, S. Y. Xu, J. M. Bai, R. J. Xiao, Y. H. Hu, H. Li, X. Q. Yang, L. Q. Chen and X. J. Huang, *Nat. Commun.*, **2013**, *4*, 2365.
- 2 S. Yuan, X. L. Huang, D. L. Ma, H. G. Wang, F. Z. Meng and X. B. Zhang, *Adv. Mater.*, **2014**, *26*, 2273.
- 3 T. F. Zhou, W. K. Pang, C. F. Zhang, J. P. Yang, Z. X. Chen, H. K. Liu and Z. P. Guo, *ACS Nano*, **2014**, *8*, 8323.
- 4 D. Su, H. J. Ahn and G. Wang, *Chem. Commun.* **2013**, *49*, 3131.
- 5 B. H. Qu, C. Z. Ma, G. Ji, C. H. Xu, J. Xu, Y. S. Meng, T. H. Wang and J. Y. Lee, *Adv. Mater.*, **2014**, *26*, 3854.
- 6 Y. Yan, Y. X. Yin, Y. G. Guo and L. J. Wan, *Adv. Energy Mater.*, **2014**, *4*, DOI: 10.1002/aenm.201301584.
- 7 T. Q. Chen, L. K. Pan, T. Lu, C. L. Fu, D. H. C. Chua and Z. Sun, *J. Mater. Chem. A*, **2014**, *2*, 1263.
- 8 M. Dahbi, N. Yabuuchi, K. Kubota, K. Tokiwa and S. Komaba, *Phys. Chem. Chem. Phys.*, **2014**, *16*, 15007.
- 9 M. D. Slater, D. Kim, E. Lee and C. S. Johnson, *Adv. Funct. Mater.*, **2013**, *23*, 947.
- 10 H. Yu, Y. Ren, D. Xiao, S. Guo, Y. Zhu, Y. Qian, L. Gu and H. Zhou, *Angew. Chem., Int. Ed.*, **2014**, *53*, 8963.
- 11 K. Tang, L. J. Fu, R. J. White, L. H. Yu, M.-M. Titirici, M. Antonietti and J. Maier, *Adv. Energy Mater.*, **2012**, *2*, 873.
- 12 V. L. Chevrier and G. Ceder, *J. Electrochem. Soc.*, **2011**, *158*, 1011.

13. L. Lian g, Y. Xu, C. Wan g, L. Wen, Y. Fan g, Y. Mi, M. Zh ou, H. Zh ao, Y. Lei, *Energy Environ. Sci.*, **2015**, 8, 2954–2962.
14. H. Hou, M. Jing, Z. Hu an g, Y. Yang, Y. Zh an g, J. Ch en, Z. Wu, X. Ji, *ACS Appl. Mater. Interfaces*, **2015**, 7, 19362–19369.
15. Z. Liu, X.-Y. Yu , X.W. Lou, U. Paik, *Energy Environ. Sci.* **2016**, 9, 2314–2318.
16. X. Xion g, G. Wang, Y. Lin , Y. Wang, X. Ou , F. Zh eng, C. Yan g, J.-H. Wang, M. Liu, *ACS Nano* **2016**, 10, 10953–10959.
17. J. He, Y. Wei, T. Zhai and H. Li, *Mater. Chem. Front.*, 2018, 2, 437–455.
18. D. T. Ngo, H. T. T. Le, X.-M. Pham, J.-W. Jung, N. H. Vu, J. G. Fisher, W.-B. Im, I.-D. Kim and C.-J. Park, *J. Mater. Chem. A*, 2018, 6, 2834–2846.
19. X.-M. Pham, D. T. Ngo, H. T. T. Le, P. N. Didwal, R. Verma, C.-W. Min, C.-N. Park and C.-J. Park, *Nanoscale*, 2018, 10, 19399–19408.
20. L. Wu, X. Hu, J. Qian, F. Pei, F. Wu, R. Mao, X. Ai, H. Yang and Y. Cao, *Energy Environ. Sci.*, 2014, 7, 323–328.
21. L. Fan, J. Zhang, J. Cui, Y. Zhu, J. Liang, L. Wang and Y. Qian, *J. Mater. Chem. A*, 2015, 3, 3276–3280.
22. H. Hou, M. Jing, Y. Yang, Y. Zhu, L. Fang, W. Song, C. Pan, X. Yang and X. Ji, *ACS Appl. Mater. Interfaces*, 2014, 6, 16189–16196.
23. H. Kim and J. Cho, *Chem. Mater.*, 2008, 20, 1679–1681.
24. A. Dailly, J. Ghanbaja, P. Willmann and D. Billaud, *J. Power Sources*, 2004, 125, 70–76.
25. J. Liu, L. Yu, C. Wu, Y. Wen, K. Yin, F.-K. Chiang, R. Hu, J. Liu, L. Sun, L. Gu, J. Maier, Y. Yu and M. Zhu, *Nano Lett.*, 2017, 17, 2034–2042.
26. Y.-L. Ding, C. Wu, P. Kopold, P. A. van Aken, J. Maier and Y. Yu, *Small*, 2015, 11, 6026–6035.
27. Q. Yang, J. Zhou, G. Zhang, C. Guo, M. Li, Y. Zhu and Y. Qian, *J. Mater. Chem. A*, 2017, 5, 12144–12148.
28. Z. Yi, Q. Han, P. Zan, Y. Wu, Y. Cheng and L. Wang, *J. Power Sources*, 2016, 331, 16–21.
29. M. He, K. Kravchyk, M. Walter and M. V. Kovalenko, *Nano Lett.*, 2014, 14, 1255–1262.
30. M. Walter, R. Erni and M. V. Kovalenko, *Sci. Rep.*, 2015, 5, 8418.

31. J. Duan, W. Zhang, C. Wu, Q. Fan, W. Zhang, X. Hu and Y. Huang, *Nano Energy*, 2015, 16, 479–487.
32. a) C. de Mello Donegá, P. Liljeroth, D. Vanmaekelbergh, *Small* 2005, 1, 1152–1162; b) D. A. Ruddy, J. C. Johnson, E. R. Smith, N. R. Neale, *ACS Nano*, 2010, 4, 7459–7466.
33. S. Zhang, K. Dokko, M. Watanabe, *Chem. Mater.* 2014, 26, 2915–2926.
34. Y. Wang, Y. Shao, D. W. Matson, J. Li, Y. Lin, *ACS Nano*, 2010, 4, 179
35. H. Wang, T. Maiyalagan, X. Wang, *ACS Catal.* 2012, 2, 781–794.
36. a) L. Zhi, K. Müllen, *J. Mater. Chem.* 2008, 18, 1472–1484; b) A. Narita, X. Feng, Y. Hernandez, S. A. Jensen, M. Bonn, H. Yang, I. A. Verzhbitskiy, C. Casiraghi, M. R. Hansen, A. H. R. Koch, G. Fytas, O. Ivasenko, B. Li, K. S. Mali, T. Balandina, S. Mahesh, S. De Feyter, K. Müllen, *Nat. Chem.* 2013, 6, 126–132; c) L. Talirz, P. Ruffieux, R. Fasel, *Adv. Mater.* 2016, 28, 6222– 6231; d) Y. Segawa, H. Ito, K. Itami, *Nat. Rev. Mater.* 2016, 1, 15002.
37. A. Turchanin, A. Beyer, C. T. Nottbohm, X. Zhang, R. Stosch, A. Sologubenko, J. Mayer, P. Hinze, T. Weimann, A. Götzhäuser, *Adv. Mater.* 2009, 21, 1233–1237.
38. M. A. Meshgi, S. Biswas, D. McNulty, C. O’Dwyer, G. A. Alessio Verni, J. O’Connell, F. Davitt, I. Letofsky-Papst, P. Poelt, J. D. Holmes, C. Marschner, *Chem. Mater.* 2017, 29, 4351–4360.
39. Y. Xiao, M. Cao, *ACS Appl. Mater. Interfaces*, 2014, 6, 12922–12930.
40. Y. Xu, X. Zhu, X. Zhou, X. Liu, Y. Liu, Z. Dai, J. Bao, *J. Phys. Chem. C*, 2014, 118, 28502–28508.
41. Z. Yi, Q. Han, P. Zan, Y. Wu, Y. Cheng and L. Wang, *J. Power Sources*, 2016, 331, 16–21.
42. A. Dailly, J. Ghanbaja, P. Willmann and D. Billaud, *Electrochim. Acta*, 2003, 48, 977–984.
43. J. Zhu, T. Sun, J. Chen, W. Shi, X. Zhang, X. Lou, S. Mhaisalkar, H. H. Hng, F. Boey and J. Ma, *Chem. Mater.*, 2010, 22, 5333–5339.
44. D. Chang, H. Huo, K. E. Johnston, M. M’én’etrier, L. Monconduit, C. P. Grey and A. Van der Ven, *J. Mater. Chem. A*, 2015, 3, 18928–18943.
45. Y. Yang, X. Yang, Y. Zhang, H. Hou, M. Jing, Y. Zhu, L. Fang, Q. Chen and X. Ji, *J. Power Sources*, 2015, 282, 358–367.

46. (a) D. Su, H. J. Ahn and G. Wang, *Chem. Commun.*, 2013, 49, 3131. (b) B. H. Qu, C. Z. Ma, G. Ji, C. H. Xu, J. Xu, Y. S. Meng, T. H. Wang and J. Y. Lee, *Adv. Mater.*, 2014, 26, 3854.
47. H. Hou, M. Jing, Y. Yang, Y. Zhu, L. Fang, W. Song, C. Pan, X. Yang and X. Ji, *ACS Appl. Mater. Interfaces*, 2014, 6, 16189–16196.
48. H. Kim and J. Cho, *Chem. Mater.*, 2008, 20, 1679–1681.
49. A. Dailly, J. Ghanbaja, P. Willmann and D. Billaud, *J. Power Sources*, 2004, 125, 70–76.
50. J. Liu, L. Yu, C. Wu, Y. Wen, K. Yin, F.-K. Chiang, R. Hu, J. Liu, L. Sun, L. Gu, J. Maier, Y. Yu and M. Zhu, *Nano Lett.*, 2017, 17, 2034–2042.

Appendix

**Cobalt-Graphitic Nano-Composite
Characterisation and Hydrogen Evolution
Reaction Performance**

5.1 Introduction

It is necessary to develop an efficient, cost-effective, and environment-friendly water electrolysis system to produce hydrogen fuel, which is non-polluting. Hydrogen is favourable for sustainably satisfying the clean energy demands of modern society.¹ Typically, in a water electrolysis system, oxygen gas and hydrogen gas are evolved at anode and cathode via the oxygen evolution reaction (OER) and hydrogen evolution reaction (HER), respectively. To overcome the energy barrier (1.23 V) of the water splitting reaction, an external voltage is applied to the system. Currently, hydrogen production through water splitting contributes approximately 4% of the total H₂ production worldwide, which is a small fraction.^{12–13} This is mainly due to the high cost of the electrocatalysts and photoelectrocatalysts. In practise, the energy conversion efficiency of hydrogen production through water splitting is 50–70%.¹⁴ To further enhance this energy conversion efficiency, it is necessary to develop efficient catalysts. Currently, excellent energy conversion efficiency has been achieved using noble metal-based catalysts for the HER.¹⁵ Pt is particularly the best electrocatalyst for the HER.¹⁵ However, it is not an abundant material in the earth's crust. Therefore, the development of catalysts from abundantly available materials, with activity comparable to that of the noble-metal catalysts, is required. Consequently, researchers have devoted considerable effort into synthesizing different kinds of non-noble metal-based catalysts from different types of conceptual designs. 3d transition metals, which are abundant in the earth's crust, have attracted significant interest in recent years for HER catalysis. This is also because of their low cost and excellent theoretical activity.^{16–19a} However, in strong acidic or alkaline medium, bare transition-metal materials are unstable and their electrocatalytic activity decay severely. However, a carbon layer on the transition metal nanocrystal prevents the decay of the nanocrystal under harsh oxidation conditions. This also increases the conductivity of the nanocomposite.^{20–24} Therefore, the encapsulation of nanocrystals with carbon layer gives new insights into improving the activity, conductivity, and stability of materials, which are already being used in ORR,^{25–26} and HER.^{27–33a} The H-bonding energy of metallic cobalt is important for HER.^{33b} In addition, carbon shells covered with cobalt nanocrystals reduce the corrosion of the nanocrystal material.^{34a} Therefore, cobalt-nitrogen-doped carbon nanocomposites are good candidates for the HER over a wide pH range. CNT-based Co-NRCNT material have been used to catalyse the HER,^{35a} while Co-N-C composites to have been used for the overall water splitting,^{36a} as well as Co nanoparticles in N-doped carbon (Co@N-C). Co-N-graphene).⁴² These studies give excellent results; however, there are

challenges that need to be overcome. Herein we report the synthesis of N-doped carbon-encapsulated cobalt nanocrystals scattered on carbon nanosheets (Co/NG/C). The cobalt nanocrystals were placed in close contact with the N-doped carbon layers, which can offer several catalytically active sites.^{37,38} Moreover, these nanocrystals are unified by the structure of the carbon nanosheets formed during a colloidal hot injection synthesis process. This enables the electron and mass transport through catalytic tests.³⁹ As a result, the Co/NG/C nanocomposite was an efficient and durable HER electrocatalyst under both acidic and alkaline conditions, which is an important property for HER catalysts.^{34b} An overpotential of 310 mV was required to achieve 10 mA cm⁻² under acidic conditions.

5.2 Experimental Sections

5.2.1 General Remarks.

Synthesis: All chemicals were purchased from Sigma-Aldrich and used as is. Tetrahydrofuran and pentane were refluxed over sodium/benzophenone and distilled prior to use. Acetone and toluene were also distilled prior to use. Oleylamine was stirred overnight at 100 °C under vacuum prior to use. 1,4-Bis-(trimethylsilyl)-1,4-diaza-2,5-cyclohexadiene was prepared according to a procedure reported in literature. The annealing was carried out in a Nabertherm RHTC 80-710/15.

5.2.2 Synthesis of the Co/NG: 1,4-Bis-(trimethylsilyl)-1,4-diaza-2,5-cyclohexadiene dissolved in oleylamine (4 mL, 12.15 mmol) was heated to 200 °C in an argon atmosphere in a three-necked flask fitted with a reflux condenser. When the reaction mixture reached 200 °C, an acetonitrile (2 mL) solution of CoCl₂ was rapidly injected. The colour of the solution instantaneously turned intense brown-red. Then, the reaction temperature was increased to 250 °C (ramp up rate = 10 °C/min) and maintained there for 1 h. Subsequently, the reaction mixture was quenched to room temperature. Then, the solution was transferred into a centrifuge tube containing 2–3 mL of toluene. The Co/NG was precipitated by adding 20 mL of acetone and separated by centrifugation (9000 rpm for 10 min). After decanting the supernatant, the precipitate was resuspended in 5 mL of toluene and 25 mL of acetone was added as the non-solvent. This dissolution/precipitation/centrifugation process was repeated several times until all the impurities were removed to yield 150 mg of a black solid.

5.2.3 Synthesis of the Co/NG/C: The Co/NG (80 mg) was annealed at 900 °C for 2 h under argon containing 5% hydrogen in a furnace to yield a black powder Co/NG/C (40 mg). The heating rate was 5 °C/min.

5.2.4 Characterization: The powder X-ray diffraction (PXRD) patterns of the Ge-graphenic nanocomposites were recorded on a Bruker D8 Advance X-ray diffractometer using Cu K α radiation (1.54 Å). The Raman spectra of the nanocomposites were analysed by using LabRAM HR800 from Yvon Horiba. SEM images were recorded on FEI Nova Nano 450 SEM. The AFM data were collected by Keysight atomic force microscope (model: AFM 5500) using the tapping mode technique. The TEM images were taken using a JEOL JEM 2100 FS field-emission transmission electron microscope at 200 kV.

5.2.5 Electrochemical Measurements for Hydrogen Evolution Study

All the electrochemical measurements were carried out by PAR Potentiostat/Galvanostat (PARSTAT 2273) using a typical three electrode system. A graphite rod and Ag/AgCl (3 M KCl) were used as the counter and reference electrodes, respectively. Meanwhile, a glassy carbon electrode loaded with catalyst was used as the working electrode. Co/NG/C (20 mg) and 10 μ L Nafion were added to 2 mL ethanol and sonicated (at least 2 h) to prepare the catalyst ink. A 2- μ L aliquot of catalyst ink was carefully drop-casted on the glassy carbon electrode of 3 mm diameter and dried under vacuum. All the measurements were performed in 0.5 M H₂SO₄ solution. Linear sweep voltammetry (LSV) measurements were carried out at a scan rate of 5 mV/s and the polarization curves were corrected for the iR contribution within the cell. The potentials were converted and reported with respect to the reversible hydrogen electrode (RHE) using equation; $E_{\text{RHE}} = E \text{ vs Ag/AgCl} + 0.059^{\text{pH}} + E^0 (\text{Ag/AgCl})$. The geometric surface areas of electrodes were used to calculate the current density.

5.3 Results and Discussion

5.3.1 Preparation of the Co/NG Nanocomposite

A 2.16 mmol solution of 1,4-bis-(trimethylsilyl)-1,4-diaza-2,5- cyclohexadiene 1 dissolved in 24.3 mmol of oleylamine under an inert atmosphere in a three-necked round bottomed flask was heated to 150 °C. When the reaction temperature reached 200 °C, a 3.3 mmol solution of CoCl₂ in toluene was rapidly injected leading to an immediate temperature drop to ~170 °C. The solution also turned dark brownish-red instantaneously. After the temperature recovered to 150 °C, the reaction temperature was raised to 250 °C (ramp up rate = 10 °C/min) and maintained there for 1 h. After subsequent cooling to room temperature, the dark brown solid was isolated using the solvent/non-solvent technique. The washing and centrifugation were repeated until all the impurities, such as unbound oleylamine were removed. This method

was gram-scalable and the resulting dark brown solid Co/NG was dried. The Co/NG formed a stable colloidal suspension in toluene. A burst of homogeneous nucleation followed by steady controlled growth using the hot injection method led to the formation of high-quality monodispersed Co/NG nanocomposites.

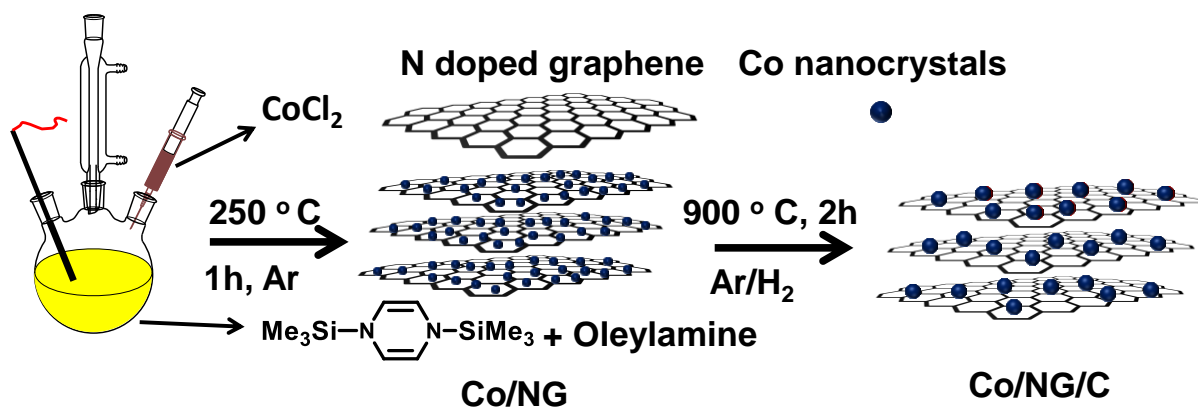


Figure 5.1: Schematic representation of the synthesis of the Co/NG and Co/NG/C nanocomposites.

5.3.2 Structural and Microscopic Analysis

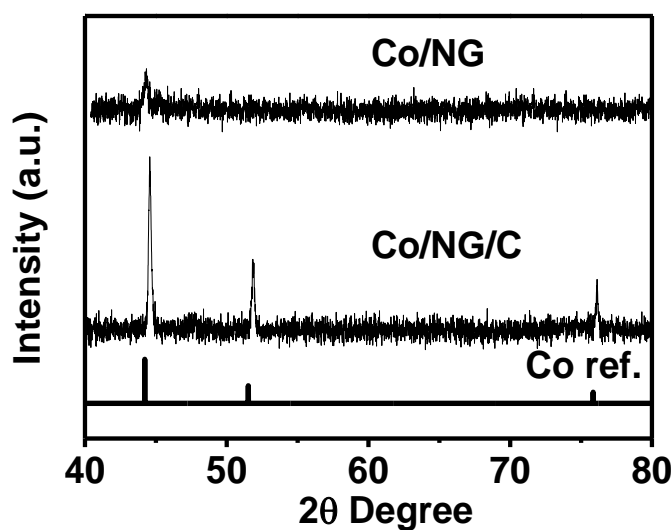


Figure 5.2 PXRD pattern of the Co/NG and Co/NG/C

The PXRD pattern (Figure 5.2) of the as-synthesized Co/NG displays clear peaks at $2\theta = 44.2^\circ$ which could be well-indexed to the diamond cubic Co (JCPDS card No. 15-0806). The XRD pattern of the Ge/NG/C shows intense and sharp peaks corresponding well to the diamond cubic phase of Co (Figure 5.2).

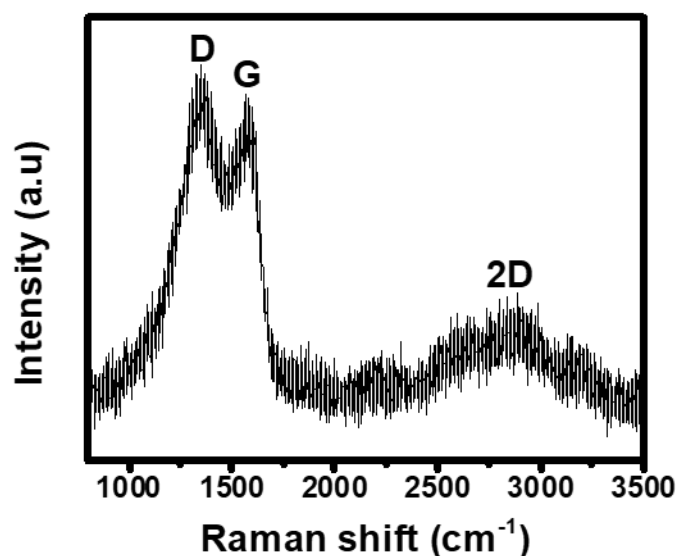


Figure 5.3 Raman spectra of the Co/NG/C

The Raman spectra of the Co/NG/C (Figure 5.3) shows three characteristic peaks at 1345 and 1533 cm^{-1} , which are in good agreement with the typical optical modes of the D band (disorder induced phonon mode) and G band (graphitic band) of C, respectively. A distinct broad 2D peak, attributed to the second-order D band, appeared at 2645 cm^{-1} in the Raman spectrum.

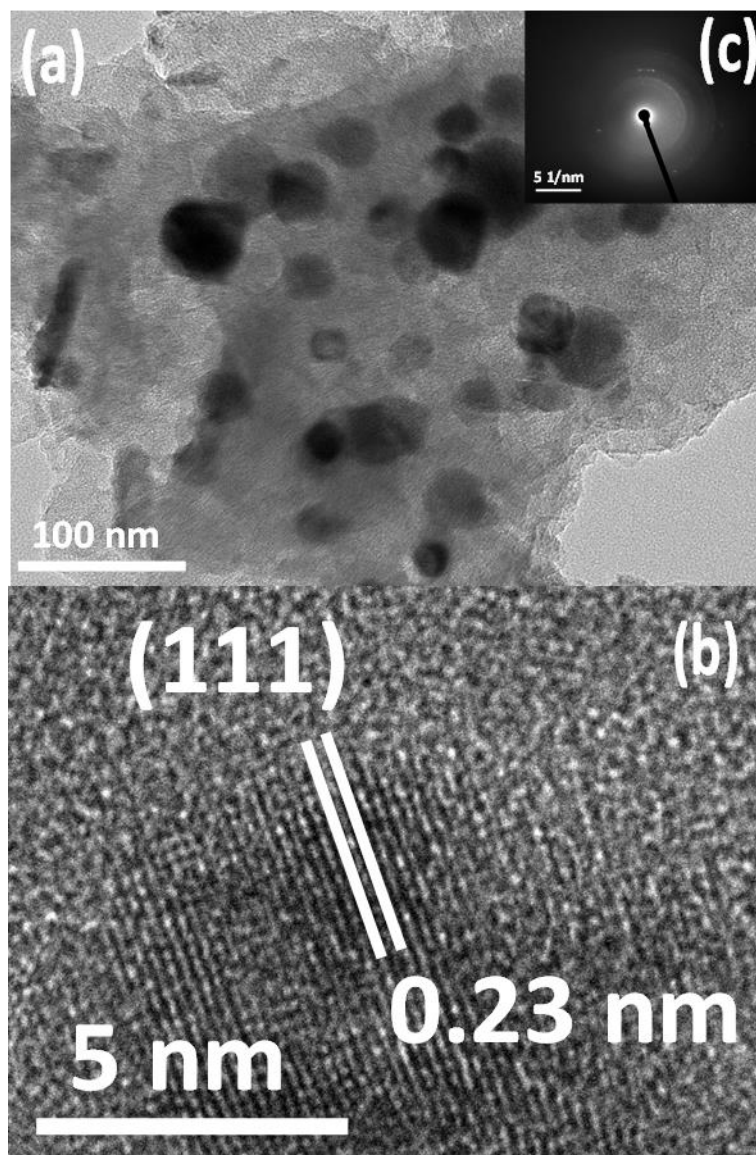


Figure 5.4 (a) TEM; (b) HRTEM; (c) SAED images of the Co/NG/C;

The TEM image (Figure 5.4a) reveals that the Co NCs were anchored on the graphitic nanosheets. The mean size of Co NCs was 40 nm as determined from the HRTEM (Figure 5.4b). The lattice fringes had an interlayer spacing of 0.23 nm (Figure 5.4b), which agrees well with the (111) plane of the diamond cubic Co and matches with the interlayer spacing calculated from the PXRD. The SAED pattern also revealed that the Co NCs had a diamond cubic structure. No diffraction patterns associated with the graphitic sheets were observed indicating the poor degree of graphitisation.

5.3.3 Electrochemical HER Using the Co/NG/C Nanocomposite

The HER was carried out using a typical three electrode system. The working electrode was prepared by drop-casting 0.28 mg/cm^2 of Co/NG/C nanocomposite on the glassy carbon (GC) electrode. The Ag/AgCl (3 M KCl) and graphite rods were used as the reference and counter electrode, respectively. The overpotential at a current density of 10 mA/cm^2 was 310 mV (Figure 5.5a).

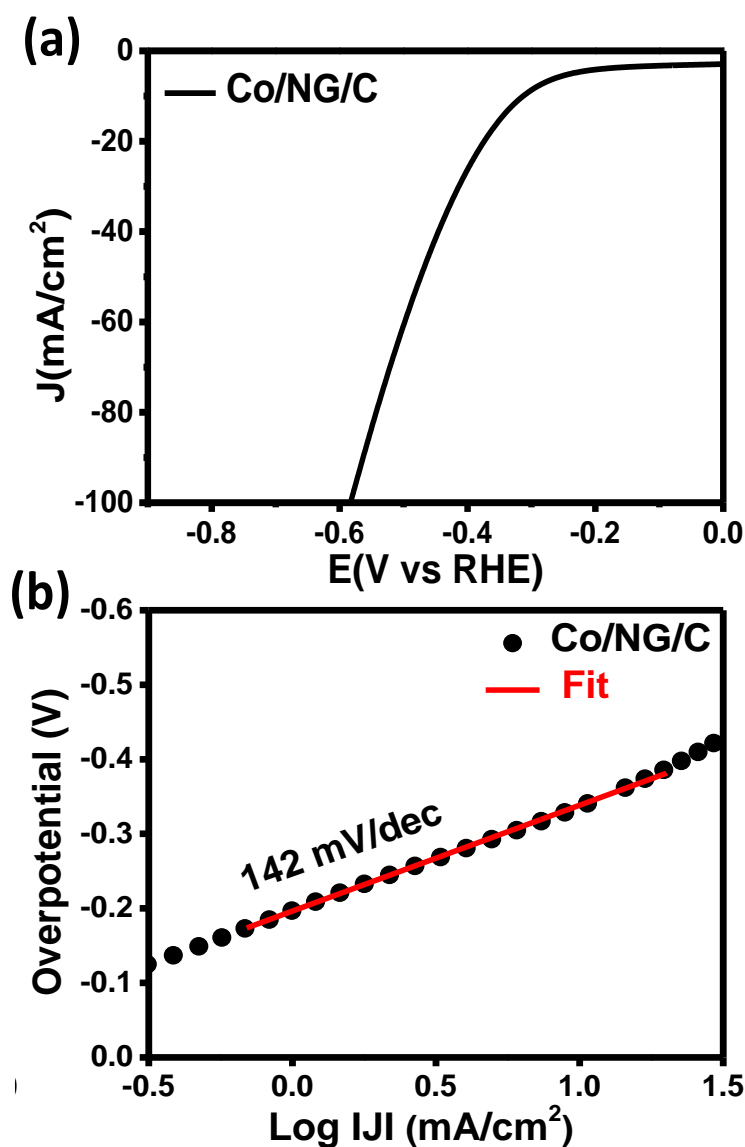


Figure 5.5: (a) LSV polarisation curve of the Co/NG/C nanocomposite (b) Tafel plot of the Co/NG/C in $0.5 \text{ M H}_2\text{SO}_4$.

The Tafel plot (Figure 5.5b) of the Co/NG/C nanocomposite catalyst had a Tafel slope of 142 mV dec^{-1} . The Tafel slope of the Co/NG/C shows that the moderate kinetics of the HER.^{35a,}

5.4 Summary

We developed a simple chemical strategy for the large-scale production of the amalgamated Co-graphitic nanocomposites. The organosilicon compound proved to be a promising precursor for producing nanostructures with tuneable composition and electronic properties. The preparation of novel nanocomposites suitable for the application in energy storage devices using this modular synthetic approach is currently underway in our laboratory.

Comparison of the Overpotential of the Co/NG/C from prior Literature

Catalyst	Electrolyte	Overpotential mV @ 10 mA cm ⁻²	References
Co/NG/C	0.5 M H₂SO₄	310	Present work
Co-NRCNTs	0.5 M H ₂ SO ₄	260	Asefa T et. al. <i>Angew. Chem.</i> 2014 , <i>126</i> , 4461–446.
Co@NC-3/1	0.5 M H ₂ SO ₄	370	Su Y C et. al. <i>Adv. Energy Mater.</i> , 2017 , <i>8</i> , 1702048.
Co@NPC	0.5 M H ₂ SO ₄	360	Biradha K et al. <i>Nanoscale Adv.</i> , 2019 , <i>1</i> , 2293–2302.
PNC/Co	0.5 M H ₂ SO ₄	370	Ai L et. al. <i>J. Mater. Chem. A</i> , 2016 , <i>4</i> , 3204–3209.
Co/HNCP	0.5 M H ₂ SO ₄	383	Li Y et. al. <i>ACS Catal.</i> , 2018 , <i>8</i> , 7879–7888.
NCNT/CoO-Co	0.5 M H ₂ SO ₄	380	Cho J et. al. <i>Angew. Chem. Int. Ed.</i> , 2015 , <i>54</i> , 9654–9658.
Co ₂ P/Co foil	0.5 M H ₂ SO ₄	319	Xu W J et. al. <i>J. Mater. Chem. A</i> , 2017 , <i>5</i> , 10561–10566.
Co@NG	0.5 M H ₂ SO ₄	172	Li G Y et. al. <i>Adv. Funct. Mater.</i> , 2016 , <i>26</i> , 4397.

References

1. J. Kibsgaard, Z. Chen, B. N. Reinecke and T. F. Jaramillo, *Nat. Mater.*, **2012**, *11*, 963–969.
2. H. Lv, Z. Xi, Z. Chen, S. Guo, Y. Yu, W. Zhu, Q. Li, X. Zhang, M. Pan, G. Lu, S. Mu and S. Sun, *J. Am. Chem. Soc.*, **2015**, *137*, 5859–5862.
3. Y. Zhao, K. Kamiya, K. Hashimoto and S. Nakanishi, *Angew. Chem., Int. Ed.*, **2013**, *52*, 13638–13641.
4. W.-F. Chen, C.-H. Wang, K. Sasaki, N. Marinkovic, W. Xu, J. T. Muckerman, Y. Zhu and R. R. Adzic, *Energy Environ. Sci.*, **2013**, *6*, 943.
5. M. A. Lukowski, A. S. Daniel, C. R. English, F. Meng, A. Forticaux, R. J. Hamers and S. Jin, *Energy Environ. Sci.*, **2014**, *7*, 2608–2613.
6. D. Kong, H. Wang, Z. Lu and Y. Cui, *J. Am. Chem. Soc.*, **2014**, *136*, 4897–4900.
7. J. Tian, Q. Liu, A. M. Asiri and X. Sun, *J. Am. Chem. Soc.*, **2014**, *136*, 7587–7590.
8. E. J. Popczun, J. R. McKone, C. G. Read, A. J. Biacchi, A. M. Wiltrout, N. S. Lewis and R. E. Schaak, *J. Am. Chem. Soc.*, **2013**, *135*, 9267–9270.
9. X. Gao, H. Zhang, Q. Li, X. Yu, Z. Hong, X. Zhang, C. Liang and Z. Lin, *Angew. Chem., Int. Ed.*, **2016**, *55*, 6290–6294.
10. M. Tavakkoli, T. Kallio, O. Reynaud, A. G. Nasibulin, C. Johans, J. Sainio, H. Jiang, E. I. Kauppinen and K. Laasonen, *Angew. Chem., Int. Ed.*, **2015**, *54*, 4535–4538.
11. W. F. Chen, K. Sasaki, C. Ma, A. I. Frenkel, N. Marinkovic, J. T. Muckerman, Y. Zhu and R. R. Adzic, *Angew. Chem., Int. Ed.*, **2012**, *51*, 6131–6135.
12. S. Peng, N. Li, X. Han, W. Sun, M. Srinivasan, S. G. Mhaisalkar, F. Cheng, Q. Yan, J. Chen and S. Ramakrishna, *Angew. Chem., Int. Ed.*, **2014**, *53*, 12594–12599.
13. X. Long, G. Li, Z. Wang, H. Zhu, T. Zhang, S. Xiao, W. Guo and S. Yang, *J. Am. Chem. Soc.*, **2015**, *137*, 11900–11903.
14. B. Cao, G. M. Veith, J. C. Neufeind, R. R. Adzic and P. G. Khalifah, *J. Am. Chem. Soc.*, **2013**, *135*, 19186–19192.
15. L. Fan, P. F. Liu, X. Yan, L. Gu, Z. Z. Yang, H. G. Yang, S. Qiu and X. Yao, *Nat. Commun.*, **2016**, *7*, 1–7.
16. E. Detsi, J. B. Cook, B. K. Lesel, C. L. Turner, Y.-L. Liang, S. Robbennolt and S. H. Tolbert, *Energy Environ. Sci.*, **2016**, *9*, 540–549.
17. M. Lefevre, E. Proietti, F. Jaouen and J. P. Dodelet, *Science*, **2009**, *324*, 71–74.

18. T. Sun, L. Xu, Y. Yan, A. A. Zakhidov, R. H. Baughman and J. Chen, *ACS Catal.*, **2016**, *6*, 1446–1450.
19. (a) L. Wu, Q. Li, C. H. Wu, H. Zhu, A. Mendoza-Garcia, B. Shen, J. Guo and S. Sun, *J. Am. Chem. Soc.*, **2015**, *137*, 7071–7074. (b) X. Liu, I.S. Amiinu, S. Liu, K. Cheng, S. Mu, *Nanoscale*, **2016**, *8*, 13311.
20. (a) J. Deng, P. Ren, D. Deng, L. Yu, F. Yang and X. Bao, *Energy Environ. Sci.*, **2014**, *7*, 1919–1923.
21. H. Zhang, Z. Ma, J. Duan, H. Liu, G. Liu, T. Wang, K. Chang, M. Li, L. Shi, X. Meng, K. Wu and J. Ye, *ACS Nano*, **2016**, *10*, 684–694.
22. Y. Xu, W. Tu, B. Zhang, S. Yin, Y. Huang, M. Kraft and R. Xu, *Adv. Mater.*, **2017**, *29*, 1605957.
23. X. Zou, X. Huang, A. Goswami, R. Silva, B. R. Sathe, E. Mikmekova´ and T. Asefa, *Angew. Chem., Int. Ed.*, **2014**, *53*, 4372–4376.
24. J. Deng, P. Ren, D. Deng and X. Bao, *Angew. Chem., Int. Ed.*, **2015**, *54*, 2100–2104.
25. J. Wang and F. Ciucci, *Small*, **2017**, *13*, 1604103.
26. C.-Y. Su, H. Cheng, W. Li, Z.-Q. Liu, N. Li, Z. Hou, F.-Q. Bai, H.-X. Zhang and T.-Y. Ma, *Adv. Energy Mater.*, **2017**, *7*, 1602420.
27. W. Gu, L. Gan, X. Zhang, E. Wang and J. Wang, *Nano Energy*, **2017**, *34*, 421–427.
28. S. H. Noh, M. H. Seo, J. Kang, T. Okajima, B. Han and T. Ohsaka, *NPG Asia Mater.*, **2016**, *8*, 312.
29. W. Zhou, J. Zhou, Y. Zhou, J. Lu, K. Zhou, L. Yang, Z. Tang, L. Li and S. Chen, *Chem. Mater.*, **2015**, *27*, 2026–2032.
30. M. Tavakkoli, T. Kallio, O. Reynaud, A. G. Nasibulin, C. Johans, J. Sainio, H. Jiang, E. I. Kauppinen and K. Laasonen, *Angew. Chem., Int. Ed.*, **2015**, *54*, 4535–4538.
31. X. Li, Z. Ao, J. Liu, H. Sun, A. I. Rykov and J. Wang, *ACS Nano*, **2016**, *10*, 11532–11540.
32. L. Han, S. Dong and E. Wang, *Adv. Mater.*, **2016**, *28*, 9266–9291.
33. (a) J. Greeley, T. F. Jaramillo, J. Bonde, I. Chorkendorff, J. K. Nørskov, *Nat. Mater.* **2006**, *5*, 909. (b) Y. Yang, Z. Lin, S. Gao, J. Su, Z. Lun, G. Xia, J. Chen, R. Zhang and Q. Chen, *ACS Catal.*, **2017**, *7*, 469–479.
34. (a) D. Deng, L. Yu, X. Chen, G. Wang, L. Jin, X. Pan, J. Deng, G. Sun, X. Bao, *Angew. Chem. Int. Ed.* **2013**, *52*, 371. (b) Vrubel, H.; Hu, X. *Angew. Chem.* **2012**, *124*, 12875–12878.

-
35. (a) X. Zou , X. Huang , A. Goswami , R. Silva , B. R. Sathe , E. Mikmeková , T. Asefa , *Angew. Chem. Int. Ed.* **2014**, *53*, 4372. (b) Chen, W. F.; Muckerman, J. T.; Fujita, E. *Chem. Commun.* **2013**, *49*, 8896-8909.
36. (a) J. Wang , D. Gao , G. Wang , S. Miao , H. Wu , J. Li , X. Bao , *J. Mater. Chem. A* **2014**, *2*, 20067. (b) Durst, J.; Simon, C.; Hasché, F.; Gasteiger, H. A. *J. Electrochem. Soc.* **2015**, *162*, F190-F203.
37. Hu, Y.; Jensen, J. O.; Zhang, W.; Cleemann, L. N.; Xing, W.; Bjerrum, N. J.; Li, Q. *Angew. Chem., Int. Ed.* **2014**, *53*, 3675– 3679.
38. Deng, J.; Yu, L.; Deng, D.; Chen, X.; Yang, F.; Bao, X. *J. Mater. Chem. A* **2013**, *1*, 14868– 14873.
39. X. Zou, Y. Zhang, *Chem. Soc. Rev.* **2015**, *44*, 5148- 5180.
40. W. Yang, L. Chen, X. Liu, J. Jia, S. Guo, *Nanoscale*, **2017**, *9*, 1738.
41. W. Zhou, J. Zhou, Y. Zhou, J. Lu, K. Zhou, L. Yang, Z. Tang, L. Li, S. Chen, *Chem. Mater.* **2015**, *2*, 2026.
42. B. He, X. Chen, J. Lu, S. Yao, J. Wei, Q. Zhao, D. Jing, X. Huang, T. Wang, *Electroanalysis*, **2016**, *28*, 2435.
43. G. Zhang, P. Wang, W.T. Lu, C.Y. Wang, Y.K. Li, C. Ding, J. Gu, X.S. Zheng, F.F. Cao, *ACS Appl. Mater. Interfaces*, **2017**, *9*, 28566.

Copy right declarations



RightsLink®



Home



Help



Email Support



Naveen kumar ▾



Coherent Solution-phase Synthesis of a Germanium-Graphitic Nanocomposite and Its Evaluation for Lithium-Ion Battery Anodes: Non-innocent Role of the Mashima Reagent

Author: Naveenkumar Akula, Neha Sharma, Apurva Lohegaonkar, et al

Publication: Chemistry - An Asian Journal

Publisher: John Wiley and Sons

Date: Feb 14, 2020

© 2020 Wiley-VCH Verlag GmbH & Co. KGaA, Weinheim

Order Completed

Thank you for your order.

This Agreement between Mr. Naveen kumar ("You") and John Wiley and Sons ("John Wiley and Sons") consists of your license details and the terms and conditions provided by John Wiley and Sons and Copyright Clearance Center.

Your confirmation email will contain your order number for future reference.

License Number 4883061297573

License date Aug 06, 2020

Order Number: 1053974

Order Date: 07 Aug 2020

Payment Information

Naveen kumar
naveenkumar.akula@students.iiser
pune.ac.in

Payment method: Invoice

Billing Address:

Mr. Naveen kumar
iiser hostel 2, iiser campus
Pune, Maharashtra 41100
8
India

+91 9764920586
naveenkumar.akula@stud
ents.iiserpune.ac.in

Customer Location:

Mr. Naveen kumar
iiser hostel 2, iiser campus
Pune, Maharashtra 41100
8
India

Order Details

1. Journal of materials chemistry. A, Materials for energy
and sustainability

Billing Status:
Open

Order license ID	1053974-1
Order detail status	Completed
ISSN	2050-7496
Type of use	Republish in a thesis/dissertation
Publisher	Royal Society of Chemistry
Portion	Image/photo/illustration

REUSE CONTENT DETAILS

Title, description or numeric reference of the portion(s)	Nanostructured anode materials for lithium ion batteries	Title of the article/chapter the portion is from	n/a
Editor of portion(s)	n/a	Author of portion(s)	Royal Society of Chemistry (Great Britain)
Volume of serial or monograph	n/a	Publication date of portion	2014-12-02
Page or page range of portion	19523		

Appendix

JOHN WILEY AND SONS LICENSE TERMS AND CONDITIONS

Aug 07, 2020

This Agreement between Mr. Naveen kumar ("You") and John Wiley and Sons ("John Wiley and Sons") consists of your license details and the terms and conditions provided by John Wiley and Sons and Copyright Clearance Center.

License Number	4883630630852
License date	Aug 07, 2020
Licensed Content Publisher	John Wiley and Sons
Licensed Content Publication	Small
Licensed Content Title	Formation Mechanisms of Uniform Nanocrystals via Hot-Injection and Heat-Up Methods
Licensed Content Author	Taeghwan Hyeon, Soon Gu Kwon
Licensed Content Date	Aug 1, 2011
Licensed Content Volume	7
Licensed Content Issue	19
Licensed Content Pages	18

<https://s100.copyright.com/AppDispatchServlet>

8/7/2020

RightsLink Printable License

Type of use Dissertation/Thesis

Requestor type University/Academic

Format Print and electronic

Order Details

1. Chemical Society reviews

Billing Status:
Open

Order license ID	1053995-1
Order detail status	Completed
ISSN	1460-4744
Type of use	Republish in a thesis/dissertation
Publisher	ROYAL SOCIETY OF CHEMISTRY
Portion	Image/photo/illustration

0.00 USD
Republishing Permission

LICENSED CONTENT

Publication Title	Chemical Society reviews	Country	United Kingdom of Great Britain and Northern Ireland
Author/Editor	Royal Society of Chemistry (Great Britain)	Rightholder	Royal Society of Chemistry
Date	01/01/1972	Publication Type	e-Journal
Language	English	URL	http://www.rsc.org/csr

REQUEST DETAILS

Portion Type	Image/photo/illustration	Distribution	Worldwide
Number of images / photos / illustrations	1	Translation	Original language of publication

REUSE CONTENT DETAILS

Title, description or numeric reference of the portion(s)	Noble metal-free hydrogen evolution catalysts for water splitting	Title of the article/chapter the portion is from	N/A
Editor of portion(s)	N/A	Author of portion(s)	Royal Society of Chemistry (Great Britain)
Volume of serial or monograph	N/A	Publication date of portion	2015-04-17
Page or page range of portion	5150		

REUSE CONTENT DETAILS

Title, description or numeric reference of the portion(s)	Nanostructured hydrotreating catalysts for electrochemical hydrogen evolution	Title of the article/chapter the portion is from	N/A
Editor of portion(s)	N/A	Author of portion(s)	Royal Society of Chemistry (Great Britain)
Volume of serial or monograph	N/A	Publication date of portion	2014-03-13
Page or page range of portion	6557		

Order Number: 1053974
Order Date: 07 Aug 2020

Payment Information

Naveen kumar naveenkumar.akula@students.ils erpune.ac.in Payment method: Invoice	Billing Address: Mr. Naveen kumar ils er hostel 2, ils er campus Pune, Maharashtra 41100 8 India +91 9764920586 naveenkumar.akula@stud ents.ils erpune.ac.in	Customer Location: Mr. Naveen kumar ils er hostel 2, ils er campus Pune, Maharashtra 41100 8 India
-------------------------------------------------------------------------------------------	-------------------------------------------------------------------------------------------------------------------------------------------------------------------------------------------------	--------------------------------------------------------------------------------------------------------------------------

Order Details

1. Journal of materials chemistry. A, Materials for energy and sustainability

Billing Status:
Open

Order license ID	1053974-1
Order detail status	Completed
ISSN	2050-7496
Type of use	Republish in a thesis/dissertation
Publisher	Royal Society of Chemistry
Portion	Image/photo/illustration

0.00 USD
Republication Permission

LICENSED CONTENT

Publication Title	Journal of materials chemistry. A, Materials for energy and sustainability	Country	United Kingdom of Great Britain and Northern Ireland
Author/Editor	Royal Society of Chemistry (Great Britain)	Rights holder	Royal Society of Chemistry
Date	01/01/2013	Publication Type	e-journal
Language	English	URL	http://pubs.rsc.org/env/journals/journalissues/ta

REQUEST DETAILS

Portion Type	Image/photo/illustration	Distribution	Worldwide
		Translation	Original language of publication

REUSE CONTENT DETAILS

Title, description or numeric reference of the portion(s)	Nanostructured anode materials for lithium ion batteries	Title of the article/chapter the portion is from	n/a
Editor of portion(s)	n/a	Author of portion(s)	Royal Society of Chemistry (Great Britain)
Volume of serial or monograph	n/a	Publication date of portion	2014-12-02
Page or page range of portion	19523		

Order Number: 1054008
Order Date: 07 Aug 2020

Payment Information

Naveen kumar
naveenkumar.akula@students.iser
pune.ac.in

Payment method: Invoice

Billing Address:

Mr. Naveen kumar
iser hostel 2, iser campus
Pune, Maharashtra 41100
8
India

+91 9764920586
naveenkumar.akula@stud
ents.iserpune.ac.in

Customer Location:

Mr. Naveen kumar
iser hostel 2, iser campus
Pune, Maharashtra 41100
8
India

Order Details

1. Chemical Society reviews

Billing Status:
Open

Order license ID	1054008-1
Order detail status	Completed
ISSN	1460-4744
Type of use	Republish in a thesis/dissertation
Publisher	ROYAL SOCIETY OF CHEMISTRY
Portion	Image/photo/illustration

0.00 USD
Republication Permission

LICENSED CONTENT

Publication Title	Chemical Society reviews	Country	United Kingdom of Great Britain and Northern Ireland
Author/Editor	Royal Society of Chemistry (Great Britain)	Rightholder	Royal Society of Chemistry
Date	01/01/1972	Publication Type	e-Journal
Language	English	URL	http://www.rsc.org/csr

REQUEST DETAILS

Portion Type	Image/photo/illustration	Distribution	Worldwide
Number of Images / photos / illustrations	1	Translation	Original language of publication

REUSE CONTENT DETAILS

Title, description or numeric reference of the portion(s)	Nanostructured hydrotreating catalysts for electrochemical hydrogen evolution	Title of the article/chapter the portion is from	N/A
Editor of portion(s)	N/A	Author of portion(s)	Royal Society of Chemistry (Great Britain)
Volume of serial or monograph	N/A	Publication date of portion	2014-03-13
Page or page range of portion	6557		

Total Items: 1

Subtotal: 0.00 USD
Order Total: 0.00 USD

Phase Changes in Ge Nanoparticles

Author: Hsiang Wei Chiu, Christopher N. Chervin, Susan M. Kauzlarich



Publication: Chemistry of Materials

Publisher: American Chemical Society

Date: Sep 1, 2005

Copyright © 2005, American Chemical Society

PERMISSION/LICENSE IS GRANTED FOR YOUR ORDER AT NO CHARGE

This type of permission/license, instead of the standard Terms & Conditions, is sent to you because no fee is being charged for your order. Please note the following:

- Permission is granted for your request in both print and electronic formats, and translations.
 - If figures and/or tables were requested, they may be adapted or used in part.
 - Please print this page for your records and send a copy of it to your publisher/graduate school.
 - Appropriate credit for the requested material should be given as follows: "Reprinted (adapted) with permission from (COMPLETE REFERENCE CITATION). Copyright (YEAR) American Chemical Society." Insert appropriate information in place of the capitalized words.
 - One-time permission is granted only for the use specified in your request. No additional uses are granted (such as derivative works or other editions). For any other uses, please submit a new request.
- If credit is given to another source for the material you requested, permission must be obtained from that source.



Alkyl-terminated crystalline Ge nanoparticles prepared from NaGe: Synthesis, functionalization and optical properties

Author: Xuchu Ma, Fengyi Wu, Susan M. Kauzlarich

Publication: Journal of Solid State Chemistry

Publisher: Elsevier

Date: July 2008

Copyright © 2008 Elsevier Inc. All rights reserved.

Order Completed

Thank you for your order.

This Agreement between Mr. Naveen kumar ("You") and Elsevier ("Elsevier") consists of your license details and the terms and conditions provided by Elsevier and Copyright Clearance Center.

Your confirmation email will contain your order number for future reference.

License Number 4897680842509

[Printable Details](#)

License date Aug 28, 2020

Licensed Content

Licensed Content Publisher Elsevier
 Licensed Content Publication Journal of Solid State Chemistry
 Licensed Content Title Alkyl-terminated crystalline Ge nanoparticles prepared from NaGe: Synthesis, functionalization and optical properties
 Licensed Content Author Xuchu Ma, Fengyi Wu, Susan M. Kauzlarich
 Licensed Content Date Jul 1, 2008
 Licensed Content Volume 181
 Licensed Content Issue 7
 Licensed Content Pages 6
 Journal Type S&T

Order Details

Type of Use reuse in a thesis/dissertation
 Portion figures/tables/illustrations
 Number of figures/tables/illustrations 1
 Format both print and electronic
 Are you the author of this Elsevier article? No
 Will you be translating? No

About Your Work

Title Preparation of Main-group and Transition metal Graphenic Nano-composites for Energy application
 Institution name IISER, pune
 Expected presentation date Nov 2020

Additional Data

Order reference number 174
 Portions Figure 1.5

Requestor Location

Mr. Naveen kumar
 iiser hostel 2, iiser campus
 Requestor Location pune, Maharashtra 411008
 India
 Attn: IISER, pune

Tax Details

Publisher Tax ID GB 494 6272 12

Appendix



Preparation of Ge nanocrystals via ultrasonic solution reduction

Author: H.P. Wu,J.F. Liu,Y.W. Wang,Y.W. Zeng,J.Z. Jjiang

Publication: Materials Letters

Publisher: Elsevier

Date: April 2006

Copyright © 2005 Elsevier B.V. All rights reserved.

Order Completed

Thank you for your order.

This Agreement between Mr. Naveen kumar ("You") and Elsevier ("Elsevier") consists of your license details and the terms and conditions provided by Elsevier and Copyright Clearance Center.

Your confirmation email will contain your order number for future reference.

License Number 4897690034851

[Printable Details](#)

License date Aug 28, 2020

Licensed Content

Licensed Content Publisher Elsevier
Licensed Content Publication Materials Letters
Licensed Content Title Preparation of Ge nanocrystals via ultrasonic solution reduction
Licensed Content Author H.P. Wu,J.F. Liu,Y.W. Wang,Y.W. Zeng,J.Z. Jjiang
Licensed Content Date Apr 1, 2006
Licensed Content Volume 60
Licensed Content Issue 7
Licensed Content Pages 4
Journal Type S&T

Order Details

Type of Use reuse in a thesis/dissertation
Portion figures/tables/illustrations
Number of figures/tables/illustrations 1
Format both print and electronic
Are you the author of this Elsevier article? No
Will you be translating? No

About Your Work

Title Preparation of Main-group and Transition metal Graphenic Nano-composites for Energy application
Institution name IISER,pune
Expected presentation date Nov 2020

Additional Data

Order reference number 185
Portions figure 1.6

Requestor Location

Mr. Naveen kumar
iiser hostel 2, iiser campus
Requestor Location pune, Maharashtra 411008
India
Attn: IISER, pune

Tax Details

Publisher Tax ID GB 494 6272 12



Colloidal Synthesis of Infrared-Emitting Germanium Nanocrystals

Author: Doh C. Lee, Jeffrey M. Pietryga, Istvan Robel, et al

Publication: Journal of the American Chemical Society

Publisher: American Chemical Society

Date: Mar 1, 2009

Copyright © 2009, American Chemical Society

PERMISSION/LICENSE IS GRANTED FOR YOUR ORDER AT NO CHARGE

This type of permission/license, instead of the standard Terms & Conditions, is sent to you because no fee is being charged for your order. Please note the following:

- Permission is granted for your request in both print and electronic formats, and translations.
 - If figures and/or tables were requested, they may be adapted or used in part.
 - Please print this page for your records and send a copy of it to your publisher/graduate school.
 - Appropriate credit for the requested material should be given as follows: "Reprinted (adapted) with permission from (COMPLETE REFERENCE CITATION). Copyright (YEAR) American Chemical Society." Insert appropriate information in place of the capitalized words.
 - One-time permission is granted only for the use specified in your request. No additional uses are granted (such as derivative works or other editions). For any other uses, please submit a new request.
- If credit is given to another source for the material you requested, permission must be obtained from that source.

